Advanced lithography by self-assembly of PS-b-PDMS and associated plasma ething : application to the fabrication of functional graphene nanoribbons arrays

Javier Arias Zapata

Communauté
UNIVERSITÉ Grenoble Alpes

THÈSE

Pour obtenir le grade de

DOCTEUR DE LA COMMUNAUTÉ UNIVERSITÉ GRENOBLE ALPES

Spécialité : NANO ELECTRONIQUE ET NANO TECHNOLOGIES

Arrêté ministériel : 25 mai 2016

Présentée par

Javier ARIAS ZAPATA

Thèse dirigée par **Marc ZELSMANN**, CNRS
et codirigée par **Gilles CUNGE**

préparée au sein du **Laboratoire Laboratoire des Technologies de la Microélectronique**
dans **l'École Doctorale Electronique, Electrotechnique, Automatique, Traitement du Signal (EEATS)**

Lithographie à très haute résolution par l'auto-assemblage du PS-*b*-PDMS et les gravures plasma associées : application à la fabrication de matrices de nanorubans de graphène

Advanced lithography by self-assembly of PS-*b*-PDMS and associated plasma etching: application to the fabrication of functional graphene nanoribbons arrays

Thèse soutenue publiquement le **19 janvier 2018**,
devant le jury composé de :

Monsieur Marc ZELSMANN
Chargé de Recherche, CNRS Délégation Alpes, Directeur de thèse
Monsieur Gilles CUNGE
Directeur de Recherche, CNRS délégation Alpes, Co-directeur de thèse
Monsieur Francesc PEREZ MURANO
Directeur de Recherche, Consejo Superior de Investigaciones Científicas, Rapporteur
Monsieur Guillaume FLEURY
Maître de Conférences, Université de Bordeaux , Rapporteur
Madame Mouis MIREILLE
Directeur de Recherche, CNRS Délégation Alpes, Président
Monsieur Rémi DUSSART
Professeur, Université d'Orléans, Examinateur

"... by standing upon the shoulders of giants."

— **Isaac Newton**, *the correspondence*

Abstract

Block copolymers (BCPs) have the particular property to self-assemble into ordered periodical structures. These macromolecules, in association with standard photolithography, represent a promising approach as an alternative advanced patterning technique in microelectronics. This way, the downsizing of Integrated Circuitss (ICs) can be kept up. BCPs with high chemical incompatibility between their blocks exhibit a high value of the Flory-Huggins interaction parameter χ. The BCP theory predicts periodical features sizes with high-χ BCPs of only few nanometers.

This thesis presents an experimental development in view of the use of a second-generation BCP lithography using the high-χ Polystyrene-*block*-Polydimethylsiloxane (PS-*b*-PDMS), versus the low-χ Polystyrene-*block*-Polydi(methyl methacrylate) (PS-*b*-PMMA). On this subject, the self-assembly kinetics of higher molecular weight (M_w) PS-*b*-PDMS BCPs (resolutions in the range of 15 - 30 nm) was improved with the blending of PS-selective plasticizers. Self-assembly on large surfaces was then proved by a rapid thermal annealing ($\sim$ 30 s). As a proof-of-concept of this lithography approach, some of the tested PS-*b*-PDMS masks were transferred on Si, where Si features sizes up to 25 nm high were achieved.

The BCP lithography principle was then used to show the patterning of 2D materials. For example, graphene presents a real need of patterning into very narrow nanostructures to open up a bandgap to switch its electrical properties by quantum confinement. A lower Mw PS-*b*-PDMS was used to pattern $\sim$ 10 nm features. Different patterning approaches were tested. BCP results are obtained when the BCP is spin-coated and annealed directly on graphene. Self-assembly on large surfaces (1 cm^2) is achieved in few minutes and the mask is then transferred on graphene by oxygen-based plasma etching, where a single step will eliminate the PS matrix, oxidized the PDMS cylinders and etch the graphene. Large surfaces 11nm-width Graphene nanoribbons (GNRs) were finally obtained. Dry H_2 plasma cleaning was also performed to remove organic contaminants appearing during the fabrication steps. Different analysis techniques of carbon such as Raman and X-ray

photoelectron spectroscopy and atomic force microscopy were used to show the high chemical quality of the GNRs.

Electrical characterization of the GNRs such as mobility and bandgap opening were measured to confirm the electronic behavior of the nanoribbons. Values of the order of 150 $cm^2/(V\cdot s)$ and 30 meV were measured, respectively. The entire procedure was realized under microelectronics clean room environment, then, the BCP self-assembly processes proposed is scalable and low cost, and is well-suited for integration with existing semiconductor fabrication techniques.

The lithography procedure developed in this investigation could also be generalized to fabricate different graphene nanostructures such as graphene nanomeshes or quantum dots that could be used in other applications in functional devices. Additionally, GNRs on large surfaces are expected to find a broad ranges of applications, in the fields of electrochemical sensors and bioanalysis.

Abrégé

Les copolymères à bloc (BCP) ont la propriété particulière de s'auto-assembler en structures périodiques ordonnées. Ces macromolécules, en association avec la photolithographie standard, représentent une approche prometteuse en tant que technique de lithographie alternative avancée en microélectronique. De cette façon, la course à la réduction des dimensions des circuits intégrés peut être maintenue. Les BCPs présentant une forte incompatibilité chimique entre leurs blocs présentent une valeur élevée du paramètre d'interaction de Flory-Huggins χ. La théorie des BCPs prédit des périodiques caractéristiques qui peuvent être aussi petites que quelques nanomètres.

Cette thèse présente un développement expérimental utilisant une lithographie de BCPs de deuxième génération avec le polystyrène-*bloc*-polydiméthylsiloxane (PS-*b*-PDMS), contre le polystyrène-*bloc*-Poly(méthyle méthacrylate) (PS-*b*-PMMA) à faible valeur de χ. La cinétique d'auto-assemblage du BCP PS-*b*-PDMS de poids moléculaire relativement élevés (résolutions dans la plage de 15 à 30 nm) a été amélioré grâce à l'ajout de plastifiants sélectifs au bloc PS. L'auto-assemblage sur des grandes surfaces a ensuite été montré par un recuit thermique rapide ($\sim$ 30 s). Comme une preuve de concept de la lithographie, certains masques PS-*b*-PDMS testés ont été transférés par gravure plasma sur le substrat Si.

Le principe de lithographie par BCP a également été utilisé pour montrer la structuration de matériaux 2D. Par exemple, le graphène présente un réel besoin de nanostructuration afin de changer ses propriétés électriques par confinement quantique quantique et ouvrir une bande interdite électronique. Pour cela, le PS-*b*-PDMS de résolution caractéristique d'environ 10 nm a été utilisé. Différentes approches d'intégration ont été testées. Les meilleurs résultats sont obtenus lorsque le BCP est enduit et recuit directement sur le graphène. L'auto-assemblage sur de grandes surfaces (1 cm^2) est réalisé en quelques minutes et le masque est ensuite transféré dans le graphène par gravure plasma à base d'oxygène, où une seule étape va éliminer la matrice PS, oxyder les cylindres PDMS et graver le graphène. De grandes surfaces de nanorubans de graphène (GNRs)

de 11 nm de largeur ont finalement été obtenues. Un nettoyage par plasma hydrogène a également été effectué pour éliminer les contaminants organiques apparaissant lors des étapes de fabrication. Différentes techniques d'analyse du carbone telles que les spectroscopie Raman et de photoélectrons X, ainsi que la microscopie à force atomique, ont été utilisées pour montrer la haute qualité chimique des GNRs.

La caractérisation électrique des GNRs tels que la mobilité et l'ouverture de la bande interdite ont été mesurées pour confirmer le comportement électronique des nanorubans. Des valeurs de l'ordre de 150 $cm^2/(V\cdot s)$ et de 30 meV ont été mesurées, respectivement. L'ensemble de la procédure a été réalisée dans un environnement de salle blanche de microélectronique, en utilisant des procédés standard et grande surface. Les développements proposés sont donc compatibles avec les techniques de fabrication de composants semi-conducteurs existantes.

La procédure lithographique développée dans cette étude pourrait également être généralisée pour fabriquer différentes nanostructures de graphène telles que des nanofilets de graphène ou des boîtes quantiques, qui pourraient être utilisées dans d'autres applications et/ou d'autres des dispositifs fonctionnels. De plus, les GNRs sur grandes surfaces pourraient trouver une large gamme d'applications dans les domaines des capteurs électrochimiques et de la bioanalyse.

Acknowledgements

Fifteen years ago when I was a teenager, I had a wish involving the research of objects at the nanoscale such as molecular machines and smart and atomic materials. The future once I imagined, constitutes now our present and I am part of it. This memory reminds me how far we can get with a simple and even crazy idea, this always with the help of someone else.

En primer lugar quiero agradecer a mi familia por haberme acompañado en este ambicioso proyecto doctoral. Entre ellos mis padres, hermanos, primos y tíos quienes con mucha humildad y respeto, a pesar de la distancia, siempre me han apoyado en mis decisiones. Sin duda, esto constituyó unas de mis principales motivaciones para concluir de forma satisfactoria.

Je remercie profondement mes directeurs de thèse Marc Zelsmann et Gilles Cunge pour leurs conseils, disponibilité et bienveillance pendant tout ce temps. Leurs encouragements et la bonne humeur furent très appréciables afin de garder toujours la bonne motivation, même dans les moments les plus turbulents. Mon développement professionnel en tant que chercheur repose sur leur remarquables qualités humaines et scientifiques.

De la même façon, je tiens à remercier Jumana Boussey, pour son écoute et ses conseils pendant tout ce temps, ainsi qu'à la direction du Laboratoire des Technologies de la Microélectronique (LTM) pour son accueil pendants ses quatre ans passées au LTM.

La haute multidisciplinarité de cette thèse m'a permis des nombreuses et étroites collaborations à qui je dois sa réussite et j'en remercie. Tout d'abord l'équipe de copolymères à bloc : Cécile Girardot, Sophie Böhme, Jérôme Garnier et Antoine Legrain. L'équipe des technologies pour la santé : Tiphaine Belloir, Anthony Léonard, David Peyrade, Alice Nicolas et Victor Gaude. L'équipe des matériaux : Bassem Salem, Mouwad Merhej, Ahmad Chaker et Sebastien Labau. L'équipe plasma : Camille Petit-Etienne, Djawhar Ferrah, Hasan Mehdi, Mathieu Sérégé, Odile Mourey et Eddy Latu-

Romain. L'équipe TEM de l'INAC : Hanako Okuno et Carlos Alvarez. Smart Force Technologies : Julien Cordeiro et Olivier Lecarme. Ainsi que les secretaires du LTM pour leur aide invaluable : Malou Clot et Sylvaine Cetra.

Et enfin je remercie mes amis de tous horizons pour leur soutien. Y finalmente agradezco a mis amigos de todos los ámbitos de la vida por el apoyo incondicional. And finally I thank my friends from various circles for their support.

I would like to express my sincere gratitude to the thesis jury, Prof. Francesc Perez Murano, Prof. Guillaume Fleury, Prof. Rémi Dussart and Prof. Mireille Mouis. Their professional evaluation and constructive review of this doctoral research will allow this exciting subject to thrust forward. Indeed, this thesis might not have been possible without utilizing the excellent facilities at SINAPS, CEA-Léti, PTA and PFNC. I owe my gratitude to technicians and engineers that monitor the proper functioning of these platforms.

I would like to finish by apologizing to all those people I forgot to acknowledge, but they deserve to be named here. At the end it is to them that I dedicate this thesis manuscript, without which, their direct or indirect contributions would have made harder this PhD, more than it already is.

January 19th, 2018

Javier Arias Zapata

Contents

List of Figures

List of Tables

Acronyms

AFM Atomic Force Microscopy. 88, 100, 118

ALD Atomic Layer Deposition. 69

BCP Block copolymer. ii, 2, 3, 8–11, 13, 14, 16, 17, 27–30, 32, 35, 37, 44, 63, 64, 99, 133

BE Binding energy. 102

DCP Diblock copolymer. 6

DLS Dynamic light scattering. 27–29

DOA Diisooctyl-adipate. 26, 27, 34, 35, 37

DOS Dioctyl-sebacate. 26–28, 30, 32, 34, 35, 37

DSA Directed self-assembly. 2, 3, 38

EUV Extreme Ultraviolet. 2

FET Field-Effect Transistor. 1, 44

FWHM Full width at half maximum. 102, 105

GISAXS Grazing incidence small angle X-ray scattering. 26, 28–30

GNR Graphene nanoribbon. ii, iii, 88, 89, 114, 118, 134

IC Integrated Circuits. ii, 1, 3, 11, 44, 133, 134

LER Line edge roughness. 139

LWR Line width roughness. 139

ODT Order disorder transition. 8, 13–15

PDMS Polydimethylsiloxane. 64, 79, 100

PGMEA Propylene glycol methyl ether acetate. 26, 28, 64

PMMA Poly(methyl methacrylate). 99, 100

PS Polystyrene. 28, 30, 32, 34, 35, 37, 64, 79

PS-*b*-PDMS Polystyrene-*block*-Polydimethylsiloxane. ii, 13, 14, 18, 19, 25–30, 33–35, 37, 39, 44, 55, 57, 58, 63, 64, 66–69, 72, 77–79, 81, 82, 86, 91, 93, 96, 98, 99, 107, 112, 113, 121, 129, 133–138

PS-*b*-PMMA Polystyrene-*block*-Polydi(methyl methacrylate). ii, 12–14, 63, 133

PS-brush Hydroxyl-terminated PS homopolymer. 26

PTP Photolithography transfer pattern. 114, 122, 124

PVD Physical Vapor Deposition. 69

SCFT Self-consistent-field theory. 6, 8, 9

SEM Scanning Electron Microscopy. 26, 36, 39, 40, 65

SVA Solvent Vapor Annealing. 15, 16, 25

TA Thermal Annealing. 14, 15, 25, 35

XPS X-Ray Photoelectron Spectroscopy. 88, 99, 100

Symbols

$D(T)$ Interface diffusion. 14

D_h Hydrodynamic diameter. 28, 29

E_g Bandgap energy. 49, 126

F Total free energy. 37

G Gibbs free energy. 4

$G(r)$ Correlation function. 147

L_0 BCP natural period. 10, 13, 29, 69

L_D Defects length. 118

N Degree of polymerization. 4, 8, 13

RT Room Temperature. 15, 30

T_g Glass Transition Temperature. 14, 15, 30

W Work of adhesion. 74

χ Flory-Huggins interaction parameter. 4, 9, 13, 16

χN Strenght of the segregation. 6–8, 13, 14

δ Solubility parameter. 5

γ Interfacial tension. 74

λ_L Laser wavelength. 118

μ Career mobility. 125

ξ Correlation length. 68, 147

a_0 Lattice constant. 46

f Volume fraction. 4, 8

1. Introduction

1.1. Background and context

For decades, miniaturization has been the keyword of the progress in microelectronics. The most successful device example is the Field-Effect Transistor (FET). Its size scaling has enabled the complexity of IC to double every 18 months [1, 2], leading to significant improvements in performance and energy efficiency per transistor. Today, processors containing two billion FETs, some with gate lengths of just 28 nm, are in mass production (fig.1.1). However, this downsizing needs to be seen with more detail from a manufacturing point of view.

Lithography is the technological process in semiconductor device fabrication to create surface features and it has been at the heart of FET miniaturization. The current lithographic technique, photolithography, uses ultraviolet light through a photomask to expose a light sensitive polymer. Subsequent removal of exposed, or unexposed, areas of the resist in a selective solvent yields to a topographic pattern which can be used as an etch mask. The six decades following the invention of the IC have seen the evolution of photolithography to the point where a modern photolithography tool, operating with an immersion lens at a wavelength of 193 nm [4], is capable of printing at a resolution of 38 nm [5].

A combination of immersion lithography and multiple patterning methods have been used by leading chip manufacturers for the latest 22 nm-node technology [6]. It requires however the use of repeated exposures and very accurate wafer positioning so that feature sizes can be trimmed which reduces wafer throughput and increases capital and other costs dramatically [7].

It is expected that these techniques will be used for the fabrication of future 14 nm-node technology. However, due to the inherent limit of the wavelength of UV light

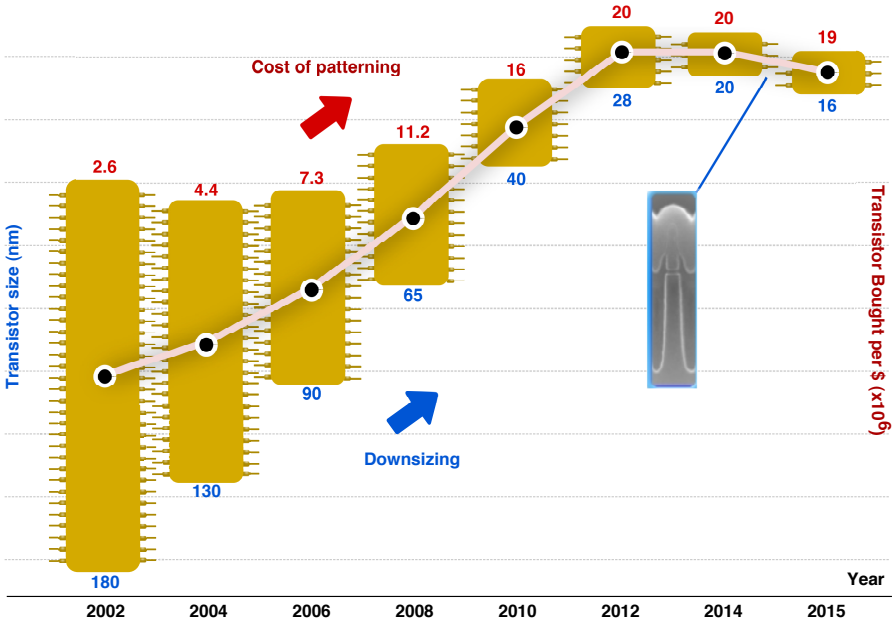

Figure 1.1.: Schematic representation of the Moore law for the last 15 years. Inset: A 19nm FET size. Adapted from [3].

sources, combined with prohibitively high costs of implementing new technologies, photolithography might be partially replaced in the future, by a surrogate lithographic process capable of producing sub-10 nm features [8].

Alternative processes to photolithography include electron-beam lithography, ion-beam lithography, X-ray lithography and nanoimprint lithography [9, 10, 11, 12]; all are top-down processes that rely on pattern transfer through masks or via molded stamps. Efforts are focused to move to shorter wavelengths (Extreme Ultraviolet (EUV) at 13.5 nm) for patterning, which are consistent with shrinking device dimensions. Nevertheless, EUV faces limitations such as EUV source power output availability of defect free masks/detection systems and considerable cost [13].

Bottom-up processes have also garnered the attention of the semiconductor industry, as viable alternatives for the fabrication of nanoscale features. In contrast to the deterministic nature of top-down processes, bottom-up processes are driven by a combination of thermodynamics and kinetics which then determines the yield of the desired structure [14]. Among those strategies: Directed self-assembly (DSA) of BCPs and DNA-based macromolecules, colloidal and fluidic assembly.

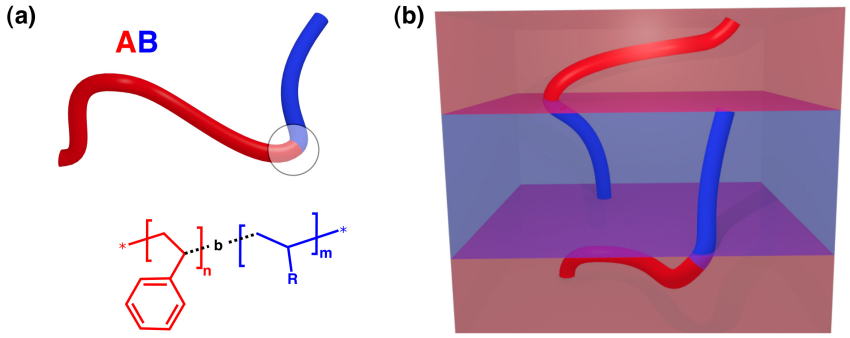

Figure 1.2.: Schematic representation of a block copolymer. (a) The A-B diblock copolymer, such as the poly(styrene)-family based diblock copolymer molecule represented at the bottom. (b) The BCP chains microphase separate such that the contact area between the A and B blocks is minimized, which lead to the formation of self-organized structures.

Particularly, DSA of BCPs on topographical patterns combines advantages of thermodynamics-governed bottom-up self-assembly of BCPs and top-down photolithography and offers opportunities to create periodic nanostructures with sub-20 nm half-pitch for the fabrication of IC components and other devices.

1.2. Physics of block copolymer systems

1.2.1. Theory of microphase separation

Flory-Huggins model

BCPs are composed of two or more chemically distinct, and usually immiscible, polymer blocks which are covalently bound to each other. The simplest system is a diblock copolymer which can be represented as $A_n - B_m$ where A and B are the molecular units and n and m are the numbers of each unit (fig.1.2a). Thermodynamic incompatibility between A and B blocks drives a collection of A–B diblock molecules to self-assembly via microphase separation [15]. An example of such a microstructured (and ordered) phase is given in (fig.1.2b) for a symmetric (50% by volume component A) diblock copolymer.

Microphase separation results from the system minimizing repulsive interactions be-

tween dissimilar blocks and maximizing attractive interactions between similar blocks. Effectively, the system attempts to minimize the interfacial surface area between unlike blocks [16]. Because of the covalent bond between blocks, phase separation can only occur on a scale similar to that of the polymer chain size, consequently length scales are in the order of one to a hundred nanometers [17].

In this far simplest case of two undiluted (bulk) blocks, A and B, the phase behavior may be controlled by three experimental parameters:

- The degree of polymerization N, with $N = n + m$
- The composition f
- The temperature dependent Flory-Huggins interaction parameter χ

The first two factors are regulated through the polymerization stoichiometry and influences the translational and configurational entropy [18], whereas the magnitude of (the largely enthalpic) χ is determined by the selection of the $A - B$ monomer pair.

The choice of a particular pair of monomers establishes the sign and magnitude of the energy of mixing, which can be approximated by the Flory-Huggins interaction parameter

$$\chi \equiv \frac{Z}{k_B T}[\epsilon_{ij} - \frac{1}{2}(\epsilon_{ii} + \epsilon_{jj})] \tag{1.1}$$

which describes the free-energy cost of contacts between A and B monomers. In this definition, Z is the number of nearest-neighbor monomers to a copolymer configuration cell, and ϵ_{ij} is the interaction energy per monomer between i and j monomers ($i = A, B; j = A, B$). From eq. 1.1, a negative value of χ results from a favorable energy of mixing, meanwhile positive values of χ occur when the net system energy increases upon forming $A - B$ contact pairs from unmixed components [19].

The thermodynamics of microphase separation is governed by a balance between enthalpic ($H = U + PV$ where U, P and V represent the system energy, pressure, and volume, respectively) and entropic (S) components. It can be represented by a simple Gibbs free energy G equation:

$$G_{mix} - G_{PS} = \Delta G_{SA} = \Delta H_{SA} - T\Delta S_{SA} \tag{1.2}$$

where G_{mix} and G_{PS} represent the free energy of the mixed and phase separated systems respectively. ΔH_{SA} is the enthalpy change of the process and is largely determined by the potential energy/intermolecular forces between the assembling entities [20]. ΔS_{SA} is the change in entropy in the process. Self-assembly is a spontaneous process if ΔG_{SA} is negative.

Flory and Huggins independently estimated the change in free energy per segment ΔG_{mix} associated with mixing polymer chains on an incompressible ($f_A + f_B = 1$) lattice, commonly referred to as the Flory-Huggins equation:

$$\frac{\Delta G_{mix}}{k_B T} = \frac{f_A}{N_A} \ln f_A + \frac{f_B}{N_B} \ln f_B + f_A f_B \chi \tag{1.3}$$

The first two terms account for the combinatorial entropy of mixing ΔS_{mix}. The third term represents the enthalpy of mixing ΔH_{mix} and can either increase or decrease ΔG_{mix} depending on the sign of χ.

Hildebrand model

For non-polar mixtures with species interacting mainly by dispersion forces, the interaction parameter χ can be estimated by the method developed by Hildebrand and Scott [21]. This model is based on the solubility parameter δ related to the energy of vaporization ΔE of a molecule. For example, for a molecule of species A the solubility parameter is defined as

$$\delta_A \equiv \sqrt{\frac{\Delta E_A}{V_A}} \tag{1.4}$$

where V_A is the volume of molecule A. The energy of vaporization ΔE_A of a molecule A is the energy of all the interactions between the molecule and its neighbors that have to be break to remove the molecule from the pure A state. The ratio $\Delta E_A / V_A$ is called the cohesive energy and is the interaction energy per unit volume between the molecules in the pure A state [22].

The interaction energy per site in a pure i state $Z\epsilon_{ii}/2$ is therefore related to the solubility parameter δ_i as follows

$$-\frac{Z\epsilon_{ij}}{2} = V_0\delta_i\delta_j \tag{1.5}$$

where $i = A, B$ and V_0 is the volume per site. Substituting Eqs 1.5 into the definition of the Flory interaction parameter (eq. 1.1), allows to express χ in terms of the solubility difference:

$$\chi \approx V_0\frac{[\delta_A^2 + \delta_B^2 - 2\delta_A\delta_B]}{k_BT} = \frac{V_0}{k_BT}(\delta_A - \delta_B)^2 \tag{1.6}$$

This result is very important because it shows that any block copolymer system where the blocks have different solubility parameters (*i.e.*, different strengths and forms of intermolecular interactions) will have a positive enthalpy of mixing and will, thus, have a tendency to microphase separate [23].

Segregation regimes

For immiscible blocks, the BCP system reduces its enthalpy H due to a decrease in A-B contacts. This process occurs locally, segregating A and B blocks. In the Diblock copolymers (DCPs), it is the product χN that controls the state of segregation [24].

Microphase separation exhibits quite different behaviors at regions of χN between near and far away ($N \to \infty$) from the order-disorder transition. In the disordered state, $\chi N \ll 10$, entropic factors dominate here and the BCP exist in a mixed state in the molecular level. Increasing χN, shifts the free energy balance and leads to the development of thermal concentration fluctuations (fig. 1.3).

In the weak segregation limit of the ordered state, in the vicinity of χN=10 predicted by the mean-field theory, the segregation power is not strong enough to form a sharp phase boundary between the two phases, and the interface becomes diffuse [25]. There exists a critical condition $(\chi N)_c$ for the phase transition, above which the ordered state exhibits a smaller free energy and becomes more stable. Fredrickson-Helfand calculated $(\chi N)_c$ by the Self-consistent-field theory (SCFT) [26], this value is higher than that

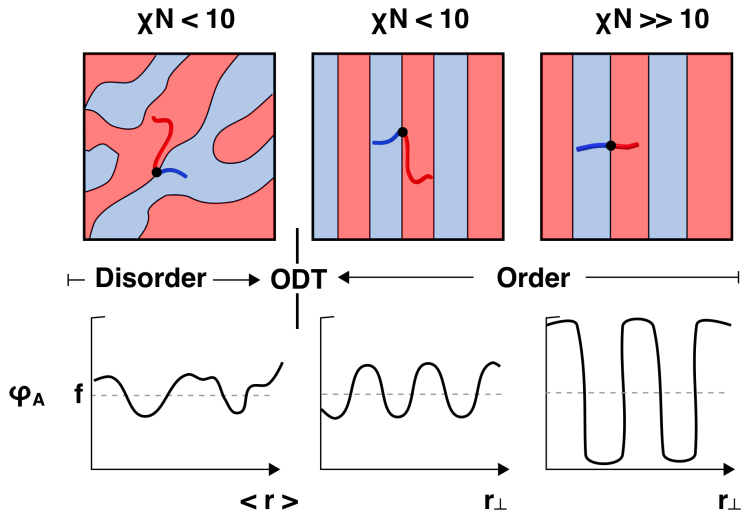

Figure 1.3.: Evolution of structure with the combined parameter χN for a symmetric diblock copolymer with $f = 0.5$. Adapted from [24].

computed by the mean-field theory. For $f = 0.5$, the critical χN is expressed by

$$(\chi N)_c \sim 10.5 + 41 N^{-1/3} \tag{1.7}$$

At the strong segregation limit in ordered state, or at $\chi N > 100$, energetic factors dominate and the ordered microstructures are characterized by narrow interfaces and nearly flat composition profiles (fig. 1.3). The interface thickness L_{int} of the phase boundary becomes proportional to $a\chi^{1/2}$ (where a is the statistical segregation segment of a BCP [27]). The microphase-separated BCP system contains mainly two free energy contributions. The first contribution comes from each chain crossing over the interface, as

$$\Delta H_{int} = kT\chi N \frac{L_{int}}{L} \sim kT\chi^{1/2} a \frac{N}{L} \tag{1.8}$$

The second contribution is the conformational entropy of deformed polymer chains due to the separation of two blocks at the two sides of the interfaces.

$$\Delta S_{sep} =\sim -(\frac{R}{R_0})^2 \sim -(\frac{L}{R_0})^2 \tag{1.9}$$

by assuming $R \propto L$ and the ideal coil size $R_0^2 = Na^2$. The total free energy contribution becomes

$$\frac{\Delta F}{kT} \sim kT\chi^{1/2}a\frac{N}{L} + \frac{L^2}{Na^2} \tag{1.10}$$

Taking the minimum free energy with respect to d, one obtains

$$L_0 \sim aN^{1/3}\chi^{1/6} \tag{1.11}$$

The Order disorder transition (ODT) is described by eq. 1.7, it establishes the microphase separation of the block copolymers. The SCFT provides a mean-field method to calculate various shapes of microdomains by combining the effects of varying χN and f. Helfand applied this theoretical method to the study of microdomain structures in BCP systems [28]. The phase diagram represented in fig. 1.4a was obtained by SCFT computations.

Seven mainly ordered phases were identified [30]. Three types of spherical, cylindrical and gyroid microstructures and lamellar morphology were shown to exist within the thermodynamically equilibrium ranges depending on the composition f and combination parameterχN.

Experimental phase diagrams have been developed and show some divergences with calculated diagrams [31]. In particular the critical $\chi_c N$ value at $\chi N = 20$ and the experimental diagram is not symmetric in terms of f. Furthermore, additional morphologies such as the hexagonally perforated lamellar (HPL) appears only experimentally and is then considered as a metastable structure (1.4b).

1.2.2. From bulk to thin films

As seen in section 1.2.1, bulk BCP can phase separate in different morphologies and sizes, depending on the structure of each of their blocks with f and N and on the interaction of

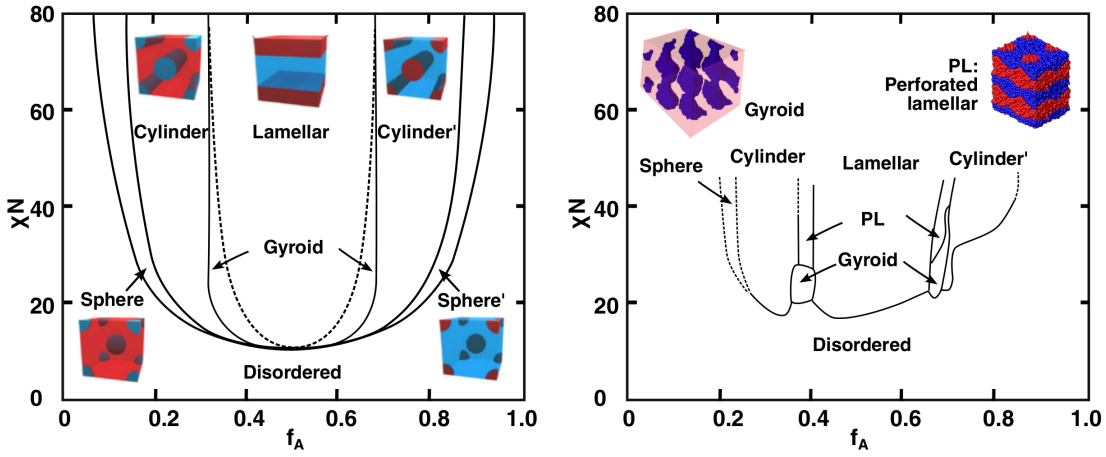

Figure 1.4.: Block copolymer phase diagram (a) by the SCFT. More useful morphologies are displayed: spheres, cylinders and lamellae. (b) obtained experimental, displaying rarer morphologies: gyroid and perforated lamella. Adapted from [15, 19, 29].

the two blocks with χ. However for most technological applications such as lithography, thin films ($<$ 100 nm) of BCPs are necessary. In thin films, other parameters such as thickness and surface and interface interactions become important and influences the phase separation and the orientation of block copolymers. The total free energy F of a diblock copolymer, AB, in a thin layer can be described as the sum of its internal structure F_{bulk} and the interface interactions $F_{surface}$:

$$F = F_{bulk} + F_{surface} \tag{1.12}$$

$$F_{bulk} = F_{A-B} + F_{conformation} \tag{1.13}$$

$$F_{surface} = F_{A-sub} + F_{B-sub} + F_{A-air} + F_{B-air} \tag{1.14}$$

where F_{A-B} is the interfacial energy between A and B blocks, $F_{conformation}$ is the structural arrangement entropy of the A and B polymers chains composing the BCP, F_{X-sub} are the interfacial energies of the blocks with the substrate and F_{X-air} are the

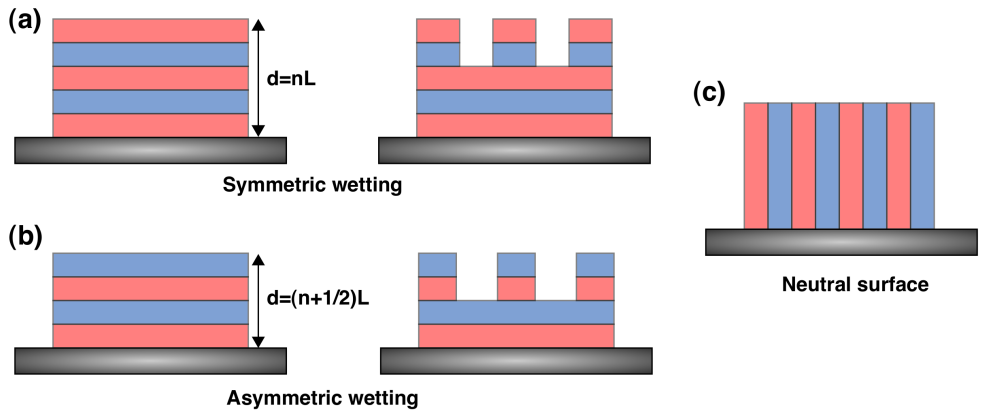

Figure 1.5.: Possible configurations of lamellae in block copolymer thin films confined at one interface. Adapted from [33].

interfacial energies with the air ($X = A, B$).

When the thickness of the block copolymer (t_f) is few times its natural domain spacing L_0, an important effect of commensurability appears between t_f and L_0. Therefore, $F_{surface}$ contribution in eq. 1.12 becomes significant to the commensurability, the total free energy and thus the final film equilibrium structure. Conformational entropy diminishes in 1.13 and consequently the BCP film is from now stable when the domains can be piled inside the film, spaced by L_0. This effect brings to a quantization of the thickness to discrete or half-discrete values of L_0 [32].

As $F_{surface}$ becomes considerable, from eq. 1.14, the orientation of the BCP domains is influenced by the interfaces between the two components of the BCP and the substrate and the air [33]. The film interfaces are classified into three categories:

1. interfacial energy of block A σ_A is higher than that of polymer B σ_B ($\sigma_A > \sigma_B$)
2. the opposite preference ($\sigma_A < \sigma_B$), and
3. neutral preference ($\sigma_A \sim \sigma_B$)

The interface is wet by the domain composed with polymer having lower surface energy. If the same block, for example A, is found at each boundary (i.e. $F_{A-sub} < F_{B-sub}$ and $F_{A-air} < F_{B-air}$), the copolymer is said to exhibit symmetric wetting (see fig. 1.5a). Alternately, BCP thin films that express different blocks at each interface are termed anti-symmetric (fig. 1.5b) [34].

At equilibrium, symmetric film systems exhibit a series of stable films when $t_f = nL_0(n = 1, 2, 3, 4)$, whereas anti-symmetric films exhibit a similar series of stable films when $t_f = (n + 1/2)L_0$. Both cases produce the lamellae to orient in-plane (horizontally) in the thin film [35]. Meanwhile when the block A and block B exhibit equal σ against the substrate and the air ($F_{A-sub} \sim F_{B-sub}$ and $F_{A-air} \sim F_{B-air}$), the BCP film is wet equally by both domains A and B. In this case, lamellar domains orientate perpendicularly against the substrate (fig. 1.5c). However, if the thickness of the film is incommensurate with the microdomain period, the microdomains can be forced to orient perpendicularly or form some other non-equilibrium structures, such as islands and holes [36].

1.2.3. Application to advanced lithography

The capability of BCP thin films to spontaneously form patterns was described in sec. 1.2.1. This arrangement includes a range of morphologies, with characteristic features below 30 nm over large areas. That makes them suitable candidates for lithographic applications [37].

Chemical dissimilarities between the two blocks is exploited to selectively remove one block relative to the other by wet or plasma etching. The remaining patterns allow transfer into an underlying target substrate, in general via plasma etching. From this point of view they behave as sacrificial templates, providing designs from a bottom-up approach. It reminds the photolithography scheme, without the technological limitations of optical systems and expensive templates.

The analogy to classical methods allows BCP lithography to be applied to the existing technological steps without changes in the infrastructure currently available in the IC industry, mostly in the use of thermal annealing to achieve self-assembly (discussed in sec. 1.3.2). Fig. 1.6 illustrates the lithography principle by BCPs thin films from vertical and horizontal cylinders morphologies (fig. 1.6a and b respectively).

1.3. Block copolymer self-assembly in manufacturing

Block copolymer self-assembly must overcome some challenges to be considered as a viable alternative to photolithography in semiconductor manufacturing:

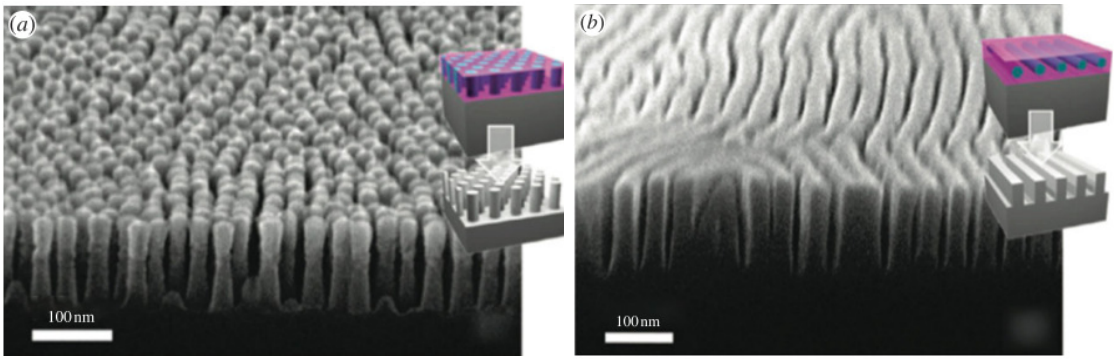

Figure 1.6.: Example of Si patterned from a PS-b-PMMA thin film mask: SEM images of (a) silicon pillars and (b) silicon trenches. Adapted from [38].

1. The pattern arrangement formed must be similar to that used in current technologies (i.e. lines, dots, holes) remaining high resolutions.

2. Integration concerns such as electronic grade purity, cost and throughput.

3. And the most critical, the patterns formed by self-assembly must have defect densities comparable to those formed by photolithography.

1.3.1. High-χ block copolymers

One of the major assumptions of the Flory-Huggins theory is that there is no volume change on mixing and that monomers of both species can fit on the sites of the same lattice. In most real polymer blends, the volume per monomer (ΔV_m) changes upon mixing [39]. These effects are usually accounted by assuming a temperature-independent additive constant in the expression of the Flory interaction parameter, often written as the sum of two terms:

$$\chi = \frac{\alpha}{T} + \beta \tag{1.15}$$

where α and β represent experimentally determined enthalpy and excess entropy coefficients for a particular composition.

The most commonly studied BCP system for lithography has been the PS-*b*-PMMA due to its ease of handling, synthesis and availability; but it has a rather low χ value

Table 1.1.: Flory-Huggins parameters for different BCPs.

Polymer name	**Flory-Huggins parameter**	χ_{eff} [a]	**Chemical structure**	**Reference**
PS-PMMA	$4.46T^{-1} + 0.028$	0.038	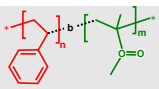	[40]
PS-PEO	$29.8T^{-1} - 0.023$	0.043	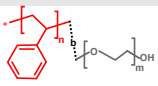	[41]
PS-P2VP	$63T^{-1} - 0.033$	0.106	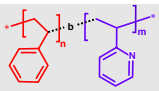	[42]
PS-PLA	$98.1T^{-1} - 0.112$	0.105	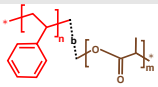	[43]
PS-PDMS	$68T^{-1} + 0.037$	0.187	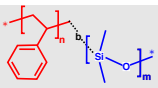	[44]
PS-P4VP	$202T^{-1} - 0.13$	0.4	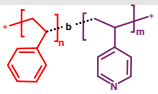	[45]
P2VP-PDMS	*n.a.*	1.0	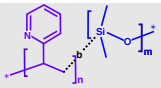	[46]
PDMS-PLA	*n.a.*	1.1	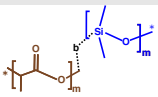	[47]

[a] at 25 °C

($\chi \sim 0.04$ at 298 K) limiting the attainable resolution to around 20 nm [48, 49, 40]. Moreover, in the PS-*b*-PMMA a small number of defects remains such as dislocations and disinclinations [50, 51]. Indeed, the defect population is related to the χ parameter. BCPs with higher χ values have a higher force for reducing the defect population and therefore more performing templates for lithography [52].

As N is reduced to achieve smaller L_0, the system tends to pass the ODT (eq. 1.7). To enable sub-10 nm structures out of the weak segregation regime ($\chi N > 10.5$), higher χ BCPs are desired [53, 54]. Table 1.1 shows some of the most researched high-χ BCPs in the literature for advanced lithography applications, with their respective $\chi(T)$ relation and chemical structure. The majority of them are PS-based, meanwhile latest efforts are focused on synthesizing BCP with higher χ values.

PS-*b*-PDMS is one particularly interesting copolymer exhibiting a higher value of χ

(χ = 0.26 at 298 K), as shown in table 1.1, allowing smaller periodicities than PS-*b*-PMMA. Another known high-χ BCPs includes the PS-P4VP, where the removal of P4VP leaves a PS mask used for patter transfer. However PS is a rather poor mask with a relatively low etch resistance. Due to its Si-containing block, PS-*b*-PDMS shows high etch-resistant selectivity between the blocks [55]. The PDMS block can easily be transformed into silica structures when exposed to oxygen plasma and the PS block can simultaneously be removed [56, 57, 58, 59]. PS-*b*-PDMS templates satisfy then both needed criteria: high resolution and etch-resistance.

1.3.2. Thermal and solvent annealing

Thermal Annealing (TA) is the simplest and most common method to trigger self-assembly in BCP systems. It consists in exposing the BCP thin film at a temperature above the T_g but below the polymer decomposition temperature approaching the ODT. The time of the annealing must be large enough to allow chain diffusion and the establishment of an equilibrium morphology.

Above T_g, the interface diffusion $D(T)$ of a polymer chain is inversely proportional to time (t) and can be described by the Arrhenius equation,

$$\frac{1}{t} \sim D(T) = a \exp(-\frac{\Delta E_a}{RT}) \tag{1.16}$$

where ΔE_a is the apparent activation energy of a polymer and a is a constant. Increasing the annealing temperature will result in faster assembly kinetics and shorten the annealing time to achieve the equilibrium ordered structure in BCP thin films [60].

It is more convenient to express $D(T)$ in terms of χN, to highlight the Arrhenius type relation 1.16, since the temperature relation of χ from eq. 1.15, is usually known (*e.g.* table 1.1):

$$D(T) \propto A \exp(-\alpha \chi N_B) \tag{1.17}$$

where N_B is the number of segments in the shorter block of a AB BCP [61]. In TA, the microphase separation process is strictly dependent on the film thickness of the

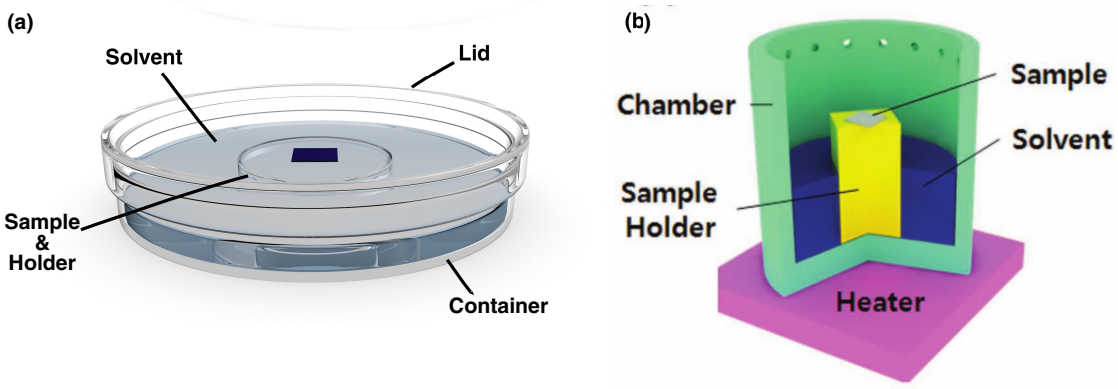

Figure 1.7.: Schematic representations of the experimental setup for the solvent vapor annealing: (a) using a petri box, (b) using a solvothermal for vapor pressure and temperature adjustment, adapted from [62, 63].

BCP. Additionally, the σ values of polymers are temperature-dependent and the $\Delta\sigma$ between the two blocks is also temperature-dependent. If the difference of σ values is large enough, a wetting layer will form at the free surface. Any formation of a wetting interface constitutes an obstacle for lithographic applications.

The TA process could not be effective enough in two situations: for many high molecular mass BCP systems, where the ODT increases considerably, and for high-χ BCPs the energetic diffusion barrier is higher due to a higher χ value. In both cases, very long annealing times are required to achieve microphase separation of the blocks. Additionally, as a function of the blocks nature, high temperatures or long annealing times could produce polymer degradation and it represents too long process times for industry.

Besides TA, Solvent Vapor Annealing (SVA) is the other common method to induce self-assembly in BCPs thin films, but not yet in industrial process. In SVA, the BCP thin films are exposed to a solvent vapor. The absorbed solvent swells the BCP thin film and effectively decreases the T_g to values near RT and increase chain mobility to high mass transport.

Due to the screening effect of the solvent molecules, the effective Flory-Huggins interaction parameter χ_{eff} is reduced as the volume fraction f_s of solvent in the film increase,

$$\chi_{eff} = \chi(1 - f_s) \tag{1.18}$$

where χ is the interaction parameter in the absence of solvent uptake. Thus, solvent uptake in BCP films decreases the effective segregation strength to $\chi_{\text{eff}}N$, and consequently affects the equilibrium domain spacing in a deflection of the effective L_0 from the bulk.

Manipulating the solvent selectivity during SVA, provides an additional control on the BCP final morphology due to a change in the volume fraction of the blocks. A tendency of the final morphology could be predicted by the phase diagram 1.4. Solvents are classified as selective or neutral, according whether they are "good" for only one of the blocks, or both. The affinity between a solvent and a polymer is evaluated by the polymer-solvent (P-S) interaction parameter $\chi_{\text{P-S}}$,

$$\chi_{P-S} = \frac{V_S(\delta_S - \delta_P)^2}{RT} + 0.34 \tag{1.19}$$

where V_S is the molar volume of the solvent and δ_S and δ_P are the Hildebrand solubility parameters of the solvent and the polymer, respectively [64]. Using the Flory-Higgins criteria, a good solvent is considered when $\chi_{P-S} < 0.5$ [65].

Experimentally, SVA is carried out by placing the BCP thin film within a closed reservoir [66], for example a petri box, filled with a volatile solvent during a period of time (fig.1.7a). The solvent evaporation rapidly saturates the chamber. Finally the BCP thin film is removed from the box and dried in the air. More complex systems have been designed with a continuous flux setup. An inert vector gas is used to carry the solvent vapor. This arrangement allows to control in a better way the partial vapor pressure of the solvents and the drying step. Indeed, the evaporation rate of the solvent during drying has been recently an object of many studies as it affects the resulting microdomain order and orientation [67].

A combination of both thermal and solvent annealing has been also proposed, against the long annealing times [68]. This consists in heating the solvent into the chamber to increase kinetics and accelerate swelling rates (see fig.1.7b). In many cases the chamber walls and the substrate are heated at the same temperature to avoid vapor condensation [69, 70].

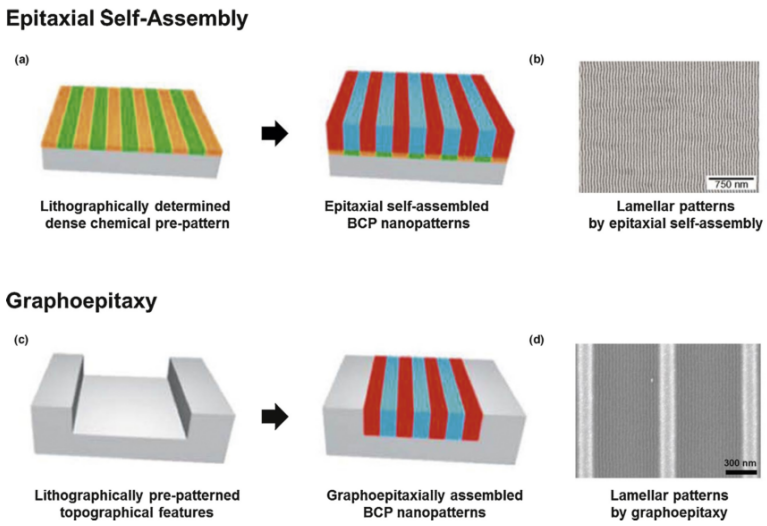

Figure 1.8.: (a) Schematic illustration of epitaxial self-assembly exploiting nanoscopic chemical patterns to direct BCP self-assembly. (b) SEM image showing defect-free lamellar patterns attained by epitaxial self-assembly . (c) Schematic illustration of graphoepitaxy utilizing topographic pattern to direct BCP assembly. (d) SEM image showing highly aligned lamellar patterns prepared by graphoepitaxy. Adapted from [71].

1.3.3. Directed self-assembly

After favoring self-assembly on free surfaces, BCPs arrange usually with short-range lateral ordering, creating the characteristic "fingerprint"or multicrystalline orientation, in the case of horizontal cylindrical or spheres morphologies respectively. In specific applications such as lithography, periodic domains with a preferential direction are required. Controlling the orientation of BCP microdomains with surface modification, either physical or chemical, is called the directed self-assembly of BCPs.

In chemoepitaxy, chemically modified patterns are used to guide the BCP self-assembly. In this technique, the patterns that are created at the surface of a substrate strongly interact with one block. The condition required is that the size of the pattern (L_p) is comparable to that of the BCP period $L_p \approx L_0$.

Graphoepitaxy uses periodical trenches to guide the self-assembly of BCPs and enhances lateral ordering in large areas. The term *graphoepitaxy* comes from the Greek roots *graphos* ($\gamma\rho\alpha\varphi\omega$) meaning "drawing ", *epi* ($\varepsilon\pi\iota$) meaning "above "and *taxis* ($\tau\alpha\xi\iota\varsigma$) meaning an ordered manner. It can be translated as "drawing to arrange upon

". In contrary to chemoepitaxy, the general pattern size of the topographical structures are a few times larger than the natural domain spacing of the BCP. These patterns are generated by conventional photolithography. The high density multiplication and the ability to align the BCP into complex and ordered structures are the key advantages of the graphoepitaxy, nevertheless features on surface cause some area loss.

1.4. Thesis outline

This thesis was mainly dedicated to the study of the PS-*b*-PDMS BCP self-assembly and its implementation as an efficient mask for the advanced lithography applications. A broad range of novel alternative applications in nanosciences are needing ultimate resolution for the study of nanostructurated materials. As high-χ BCPs are highly promising candidates to assure the downsizing of features, it is expected that PS-*b*-PDMS or other BCPs accomplish the increasing demand on the ultra high-resolution lithography.

In chapter 2, a full process of ultra-fast assembly of PS-*b*-PDMS is presented. By blending the BCP solution with plasticizers, chain mobility can be greatly increased, allowing self-assembled morphologies without any annealing treatment. Morphology transitions are proved in only few tenth of seconds. This way, the tedious SVA process can be avoided making the upscaling of the process suitable. Lithography functionalities of the PS-*b*-PDMS thin films are showed by transferring the obtained morphologies on Si, via plasma etching.

In order to give the reader a basic understanding of the needs and issues of graphene patterning, some main concepts relying this particular 2D material are recalled in chapter 3. In particular, the state-of-the-art of graphene nanoribbons fabrication in the sub-10 nm range is recapped and how the high-χ BCP lithography can fulfill this technological challenge.

In chapter 4, the first part of this study is dedicated to the study of BCP-graphene interactions in order to obtained a self-assembled PS-*b*-PDMS lithography mask on large surfaces having the horizontal cylinder morphology. The self-assembly process is achieved by thermal means only to overcome the serious issues related to the SVA. In this research, different approaches are followed, such as the direct spin-coating on graphene, using middle layers to protect graphene and promote self-assembly and the soft-graphoepitaxy

to direct self-assembly.

A large part of this work was devoted to design the experimental conditions to guarantee an accurate transfer from the PS-*b*-PDMS mask to graphene, by oxygen-based plasmas. This study is presented in chapter 5. An innovate way of graphene nanoribbons cleaning is presented at the end the process, without damaging of the structures. Usual technique for carbon analysis are used such as XPS, Raman and AFM.

Once a global procedure was determined, further characterization techniques were performed on the graphene nanoribbons surfaces, mainly on large surfaces. For this, Raman mapping is used on hundreds of μm^2 surfaces. Also electrical characterizations of the graphene nanoribbons are performed in order to show the patterning of graphene. For this, a back-gated FET was fabricated. Moreover, a new contact deposition method without the need of photoresist spin-coating is explored in chapter 6.

Bibliography

[1] G. Moore, Proceedings of the IEEE **86**, 82 (1998).

[2] "International Technology Roadmap for Semiconductors," (2013).

[3] L. Gwennap and M. Demler, "Mobile semiconductor market share forecast," Tech. Rep. (The Linley group).

[4] S. Kusumoto, M. Shima, Y. Wang, T. Shimokawa, H. Sato, and K. Hieda, Polymers for Advanced Technologies **17**, 122 (2006).

[5] W. P. de Boeij, R. Pieternella, I. Bouchoms, M. Leenders, M. Hoofman, R. de Graaf, H. Kok, P. Broman, J. Smits, J.-J. Kuit, *et al.*, in *SPIE Advanced Lithography* (International Society for Optics and Photonics, 2013) pp. 86831L–86831L.

[6] M. Hori, T. Nagai, A. Nakamura, T. Abe, G. Wakamatsu, T. Kakizawa, Y. Anno, M. Sugiura, S. Kusumoto, Y. Yamaguchi, *et al.*, in *SPIE Advanced Lithography* (International Society for Optics and Photonics, 2008) pp. 69230H–69230H.

[7] K. Lucas, C. Cork, A. Miloslavsky, G. Luk-Pat, L. Barnes, J. Hapli, J. Lewellen, G. Rollins, V. Wiaux, and S. Verhaegen, in *SPIE Advanced Lithography* (International Society for Optics and Photonics, 2008) pp. 692403–692403.

[8] R. L. Carroll and C. B. Gorman, Angewandte Chemie International Edition **41**, 4378 (2002).

[9] D. M. Tennant, Journal of Vacuum Science & Technology A: Vacuum, Surfaces, and Films **31**, 050813 (2013).

[10] J. Melngailis, A. Mondelli, I. L. Berry III, and R. Mohondro, Journal of Vacuum Science & Technology B **16**, 927 (1998).

[11] B. Wu and A. Kumar, Applied Physics Reviews **1**, 011104 (2014).

[12] L. J. Guo, Journal of Physics D: Applied Physics **37**, R123 (2004).

[13] O. Wood, J. Arnold, T. Brunner, M. Burkhardt, J. H.-C. Chen, D. Civay, S. S.-C. Fan, E. Gallagher, S. Halle, M. He, *et al.*, in *SPIE Advanced Lithography* (International Society for Optics and Photonics, 2012) pp. 832203–832203.

[14] J. A. Liddle and G. M. Gallatin, ACS nano (2016), 10.1021/acsnano.5b03299.

[15] S. Darling, Progress in Polymer Science **32**, 1152 (2007).

[16] M. Morris, Microelectronic Engineering **132**, 207 (2015).

[17] W. van Zoelen and G. ten Brinke, Soft Matter **5**, 1568 (2009).

[18] R. A. Segalman, Materials Science and Engineering: R: Reports **48**, 191 (2005).

[19] F. S. Bates and G. H. Fredrickson, Physics Today **52**, 32 (1999).

[20] W. Hu, *Polymer Physics: A Molecular Approach* (Springer-Verlag Wien, 2013) p. 248.

[21] J. H. Hildebrand and R. L. Scott, *Regular solutions* (Prentice-Hall, New York, 1962).

[22] M. Rubinstein and R. H. Colby, *Polymer Physics* (OUP Oxford, 2003).

[23] R. A. Farrell, T. G. Fitzgerald, D. Borah, J. D. Holmes, and M. a. Morris, International Journal of Molecular Sciences **10**, 3671 (2009).

[24] F. S. Bates, Science (New York, N.Y.) **251**, 898 (1991).

[25] L. Leibler, Macromolecules **13**, 1602 (1980).

[26] G. H. Fredrickson and E. Helfand, The Journal of Chemical Physics **87**, 697 (1987).

[27] E. Helfand and Z. R. Wasserman, Macromolecules **9**, 879 (1976).

[28] E. Helfand, Macromolecules **8**, 552 (1975).

[29] W.-J. Lee, S.-P. Ju, Y.-C. Wang, and J.-G. Chang, The Journal of Chemical Physics **127**, 064902 (2007).

[30] F. S. Bates and G. H. Fredrickson, Annual review of physical chemistry **41**, 525 (1990).

[31] A. K. Khandpur, S. Foerster, F. S. Bates, I. W. Hamley, A. J. Ryan, W. Bras, K. Almdal, and K. Mortensen, Macromolecules **28**, 8796 (1995).

[32] R. Gronheid and P. Nealey, eds., *Directed Self-assembly of Block Co-polymers for Nano-manufacturing*, 1st ed. (Woodhead Publishing Series in Electronic and Optical Materials, Cambridge, UK, 2015) p. 328.

[33] E. B. Gowd, M. S. Rama, and M. Stamm, *Nanofabrication: Techniques and Principles*, edited by M. Stepanova and S. Dew, Vol. 9783709104 (Springer Vienna, Vienna, 2012) pp. 191–216.

[34] M. J. Fasolka and A. M. Mayes, Annual Review of Materials Research **31**, 323 (2003).

[35] T. P. Russell, G. Coulon, V. R. Deline, and D. C. Miller, Macromolecules **22**, 4600 (1989).

[36] G. Coulon, B. Collin, D. Ausserre, D. Chatenay, and T. Russell, Journal de Physique **51**, 2801 (1990).

[37] M. Park, C. Harrison, P. M. Chaikin, R. A. Register, and D. H. Adamson, Science **276** (1997).

[38] X. Gu, I. Gunkel, and T. P. Russell, Philosophical transactions. Series A, Mathematical, physical, and engineering sciences **371**, 20120306 (2013).

[39] L. P. McMaster, Macromolecules **6**, 760 (1973), http://dx.doi.org/10.1021/ma60035a024 .

[40] Y. Zhao, E. Sivaniah, and T. Hashimoto, Macromolecules **41**, 9948 (2008).

[41] Eric W. Cochran, , David C. Morse, and F. S. Bates*, (2003), 10.1021/MA020651A.

[42] K. H. Dai and E. J. Kramer, Polymer **35**, 157 (1994).

[43] Andrew S. Zalusky, Roberto Olayo-Valles, , Johanna H. Wolf, and M. A. Hillmyer*, (2002), 10.1021/JA0278584.

[44] T. Nose, Polymer **36**, 2243 (1995).

[45] W. Zha, C. D. Han, D. H. Lee, S. H. Han, J. K. Kim, J. H. Kang, and C. Park, Macromolecules **40**, 2109 (2007).

[46] J. W. Jeong, W. I. Park, M.-J. Kim, C. A. Ross, and Y. S. Jung, Nano Letters **11**, 4095 (2011).

[47] M. D. Rodwogin, C. S. Spanjers, C. Leighton, and M. A. Hillmyer, ACS Nano **4**, 725 (2010).

[48] S.-M. Park, B. C. Berry, E. Dobisz, and H.-C. Kim, Soft Matter **5**, 957 (2009).

[49] J. Cheng, C. Ross, H. Smith, and E. Thomas, Advanced Materials **18**, 2505 (2006).

[50] G. S. Doerk, C.-C. Liu, J. Y. Cheng, C. T. Rettner, J. W. Pitera, L. E. Krupp, T. Topuria, N. Arellano, and D. P. Sanders, ACS nano **7**, 276 (2013).

[51] A. Gharbi, R. Tiron, P. Pimenta Barros, M. Argoud, I. Servin, X. Chevalier, C. Nicolet, and C. Navarro, Journal of Vacuum Science & Technology B, Nanotechnology and Microelectronics: Materials, Processing, Measurement, and Phenomena **33**, 051602 (2015).

[52] Joona Bang, †, §. Seung Hyun Kim, Eric Drockenmuller, §. Matthew J. Misner, , §. Thomas P. Russell, *, and Craig J. Hawker*, (2006), 10.1021/JA0608141.

[53] J. N. Albert and T. H. Epps, Materials Today **13**, 24 (2010).

[54] C. Sinturel, F. S. Bates, and M. A. Hillmyer, ACS Macro Letters , 1044 (2015).

[55] E. W. Cochran, C. J. Garcia-Cervera, and G. H. Fredrickson, Macromolecules **39**, 2449 (2006).

[56] Y. S. Jung and C. a. Ross, Nano letters **7**, 2046 (2007).

[57] Z. Liu, X. Gu, J. Hwu, S. Sassolini, and D. L. Olynick, Nanotechnology **25**, 285301 (2014).

[58] D. Borah, M. Ozmen, S. Rasappa, and M. Shaw, Langmuir **29**, 2809 (2013).

[59] Y. S. Jung, J. B. Chang, E. Verploegen, K. K. Berggren, and C. a. Ross, Nano letters **10**, 1000 (2010).

[60] S. Ji, L. Wan, C.-C. Liu, and P. F. Nealey, Progress in Polymer Science **54-55**, 76 (2015).

[61] H. Yokoyama, Materials Science and Engineering R: Reports **53**, 199 (2006).

[62] S. Böhme, *Towards high-χ block copolymers at the industry scale - Routes for a possible integration as a new nanostructuring technology*, Ph.D. thesis, Université de Grenoble Alpes.

[63] W. I. Park, K. Kim, H.-I. Jang, J. W. Jeong, J. M. Kim, J. Choi, J. H. Park, and Y. S. Jung, Small **8**, 3762 (2012).

[64] J. Brandrup, E. H. Immergut, and E. A. Grulke, *Polymer Handbook*, 4th ed., Vol. 2 (Wiley-Blackwell, New York, NY, 1999) p. 2336.

[65] D. W. Van Krevelen and K. Te Nijenhuis, *Properties of polymers: their correlation with chemical structure; their numerical estimation and prediction from additive group contributions* (Elsevier, 2009).

[66] B. Kim, S. W. Hong, S. Park, J. Xu, S.-K. Hong, and T. P. Russell, Soft Matter **7**, 443 (2011).

[67] W. Bai, K. G. Yager, and C. A. Ross, Macromolecules **48**, 8574 (2015).

[68] K. W. Gotrik and C. a. Ross, Nano letters **13**, 5117 (2013).

[69] J. M. Kim, Y. Kim, W. I. Park, Y. H. Hur, J. W. Jeong, D. M. Sim, K. M. Baek, J. H. Lee, M.-J. Kim, and Y. S. Jung, Advanced Functional Materials **25**, 306 (2015).

[70] S. S. Dinachali, W. Bai, K.-H. Tu, H. K. Choi, J. Zhang, M. E. Kreider, L.-C. Cheng, and C. A. Ross, ACS Macro Letters , 500 (2015).

[71] S.-J. Jeong, J. Y. Kim, B. H. Kim, H.-S. Moon, and S. O. Kim, Materials Today **16**, 468 (2013).

2. PS-b-PDMS nanolithography

2.1. Introduction

Apart from resolution, a successful lithography technique must satisfy additional requirements in order to be integrated in the front-end-of-line process of manufacturing transistors, especially in terms of throughput, cost of integration and defectivity. Taking into account the numerous parameters that have to be controlled during SVA and solvothermal annealing to achieve self-assembly, the best option remains, however, TA (section 1.3.2). It is a simple and well-known industrial method that can also easily be scaled up. This context lend motivation to test novel techniques on PS-*b*-PDMS in order to promote the self-assembly by a thermal treatment, despite its high χ value.

Blending BCPs has been employed to influence the final morphology or domain size without any subsequent synthesis steps [1]. The addition of homopolymers [2, 3, 4, 5], monomers [6] or salts [7] has already been reported in order to enhance the process time and kinetics of the self-assembly process of low-χ BCPs. Most of these proposed blending processes include the addition of a material that cannot be or is difficult to be removed, and thus permanently alters the functionality of the block copolymer for technological applications.

The addition of plasticizer molecules in the high-χ PS-*b*-PDMS solution is approached in this chapter, in order to lower its diffusive energy barrier, which could be removed without changing the obtained structures. Plasticizers are well known additives in the polymer industry. They are nonvolatile substances that are incorporated into rigid plastics to increase their flexibility. The plasticizer enters into the polymer network and expands its free volume by providing a lateral motion to the chains [8]. Here, the influence of two selective plasticizers on PS-*b*-PDMS self-assembly is investigated.

2.2. Experimental procedure

2.2.1. Materials

Cylindrical forming PS-*b*-PDMS (M_w=31–11 kg/mol, PDI=1.10 and M_w=30.5–14.5 kg/-mol, PDI=1.04), and Hydroxyl-terminated PS homopolymer (PS-brush) (M_w=3.5 kg/-mol, PI=1.06) were purchased from Polymer Source Inc. (Canada) and used as received. For simplicity, they are abbreviated BCP42 and BCP45 respectively. Solvent Propylene glycol methyl ether acetate (PGMEA) and plasticizers bis(2-ethylhexyl) Adipate Diisooctyl-adipate (DOA) and bis(2-ethylhexyl) Sebacate Dioctyl-sebacate (DOS) were purchased from Sigma Aldrich.

A third PS-b-PDMS block copolymer, generating a spherical phase was utilized for this study. This BCP was synthesized at the University of Ionnina. It has a number-average molecular weight M_w=53–17 kg/mol and polydispersive index PDI=1.07. This BCP is abbreviated BCP70.

2.2.2. Methods

Cleaned bare and graphoepitaxy Si substrates were activated in O_2 plasma for 2 min before use. For the brush preparation, PS-brush solution was deposited by spin-coating at 2000 rpm. Samples were immediately annealed at 200 °C for 5 min. Non-reacted PS-brush residues were rinsed off with PGMEA.

Samples on silicon substrates were treated with a double step (CF_4/O_2) plasma etching, in order to reveal the PDMS structures for SEM observations. The self-assembled morphologies were investigated by Scanning Electron Microscopy (SEM) (Hitachi S-5000) and focused ion beam scanning transmission electron microscopy (FIB-STEM, Helios 450S – FEI).

The Grazing incidence small angle X-ray scattering (GISAXS) measurements were performed on beamline BM02 at the European Synchrotron Radiation Facility (ESRF) in Grenoble (France). A 1 mm-wide and 100 µm-high X-ray beam impinged onto the sample at a grazing incidence angle $\alpha_i = 0.13$ °. The X-ray wavelength was 0.083 nm, corresponding to an energy beam of 15 keV; the sample-detector distance was 4.88 m; and the scattered intensity was detected by using a 2D XPAD detector with image sizes

of 1148 x 578 pixels with a dimension of 130 µm x 130 µm for a single pixel.

Dynamic light scattering (DLS) was used to characterize the size of the micelles in the plasticized BCP solution using a He-Ne gas laser with a wavelength of 633 nm and a backscattering detector positioned at a scattering angle of 180°with respect to the laser. Measurements were performed at RT conditions assuming the solvent had a refractive index of 1.402 and a viscosity of 0.8 mPa · s for PGMEA. The correlation function was fitted by the cumulant method, writing it as a second degree distribution of exponentials so that the mean D_h and the polydisperse index were computed.

Ellipsometry measurements were performed using a UVISEL™ ellipsometer from Horiba Scientific driven by the DeltaPsi 2 software. Spectral range of 300–800 nm and a model composed by Si, SiO_2 and a polymer layer (described with a Cauchy model) were used to measure the BCP film thickness evolution.

2.3. Results & Discussion

PS-selective plasticizers widely used in industry such as DOS and DOA were tested in order to study their influence on the self-assembly of PS-*b*-PDMS. Physical properties of BCP, solvent and plasticizers used in this study are listed in table 2.1. They will be useful to understand the plasticizer mechanism on the self-assembly of the PS-*b*-PDMS throughout this chapter. The χ parameters values in table 2.1 were calculated using the eq. 1.6 from the Hildrebrand model. According to this, a good indication of solubility for nonpolar materials, is indicated for $\chi < 0.5$ (section 1.3.2).

Table 2.1.: Details of some useful physical properties of plasticizers and solvents [9, 10].

	Solubility parameter ($MPa^{1/2}$)	**Vapor pressure (Pa)** [a]	**χ-PS**	**χ-PDMS**
PGMEA	17.4	3.8	0.04	0.2
DOS	17.5	$1.5x10^{-4}$	0.1	0.7
DOA	17.8	$1.1x10^{-4}$	0.04	0.8

[a] at 25 °C

2.3.1. Influence of DOS on self-assembly

A BCP42 monolayer ($\sim$ 34 nm) is obtained at 1700 rpm spin speed with 1 wt% solution in PGMEA. Then, different concentration solutions of DOS were tested (from 0.5 to 1.5 wt%). Better results were found for BCP42 and DOS having both 1 wt% in PGMEA solvent. This solution, abbreviated DOS42, was spin-coated at 1700 rpm and resulted also in a BCP monolayer at the end of the process. In order to understand the mechanism of the DOS on PS-*b*-PDMS self-assembly, the BCP was studied in the three steps involved:

1. BCP42 + DOS system in PGMEA solution
2. BCP42 + DOS thin film
3. the final self-assembled BCP42

DOS42 in solution

In the first step (1), DLS was used to analyze the effect of DOS in the BCP42 solution by measuring the D_h of PS-*b*-PDMS micelles. Adding a selective solvent to the BCP solution changes the Polystyrene (PS) volume fraction f_{PS}, leading to a shift of the micellar morphology [11]. PGMEA is a PS block-selective solvent and leads to the formation of PS_{corona} – $PDMS_{core}$ micelles in solution. As DOS is also PS-selective, spherical micellar formation is expected. Figure 2.1 shows the distribution of D_h of micelles in the BCP42 solution indicating a monodisperse solution of PS-*b*-PDMS micelles, where mean is calculated to be 33 ± 1 nm. A slight difference was observed in mean D_h micelles for the DOS42 solution (Dh $\sim 35 \pm 1$ nm), suggesting an increase of the apparent D_h by the addition of DOS without structural modification of the PS-*b*-PDMS micelles.

DOS42 thin film

In the second step (2), when DOS42 solution is spin-coated on functionalized Si substrates, the PGMEA solvent evaporates and a plasticized BCP thin film is deposited. Figs. 2.2a-b show the GISAXS data and its corresponding profile of the DOS42 thin film after spin-coating. First order reflections $1q_s$ for the BCP thin film appeared at 0.19

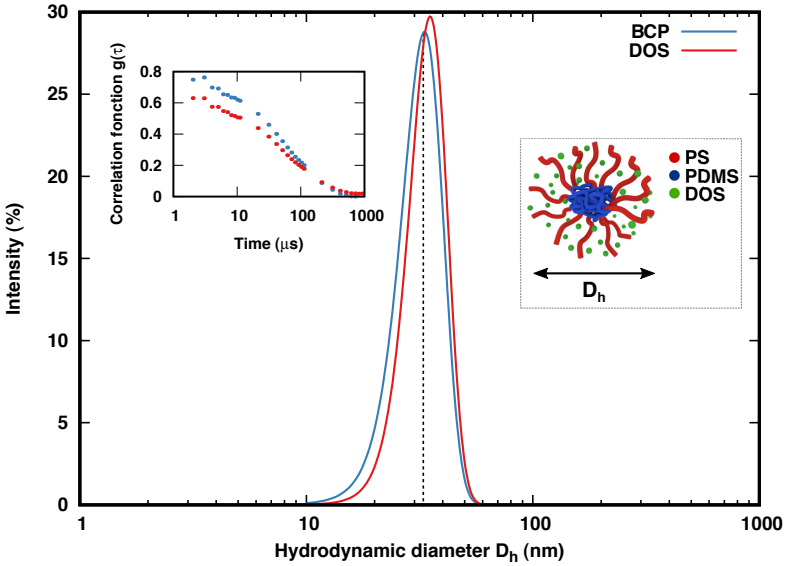

Figure 2.1.: Dynamic light scattering measurements of PS-*b*-PDMS 42 kg/mol solution (BCP42) and with the addition of DOS (DOS42 solution). Insets: (left) the respective correlation functions and (right) schematic representation of a PS-PDMS + DOS micelles.

nm^{-1} ($L_0 \sim 33$ nm), nevertheless the lack of signal does not allow to confirm the structuration and the morphology of the polymer film as no second order peaks appeared. STEM observations were then performed, cross-section view in fig. 2.2 confirms the L_0 periodicity of the spherical network in the BCP film (~ 34 nm).

Self-assembled BCP42

Fig. 2.3a illustrate the step (3), which shows a top-view SEM image of the as-spun thin film after the two-step plasma etching. This image shows the final hexagonal spheric lattice of the oxidized-PDMS having $L_0 \sim 33$ nm, which is consistent with the GISAXS analysis and STEM observations. It was shown that micelle-micelle interactions drive the system to pack in an ordered array when the hydrodynamic diameter of the micelles is comparable to L_0 [12]. In our case $D_h \sim L_0 \sim 33$ nm, as is proven by DLS, GISAXS, and STEM measurements, which is most certainly why we obtain a highly organized hexagonal spheric morphology after BCP spin-coating. For comparison, an as-spun BCP42 thin film is shown in Fig. 2.3b where a disordered and inhomogeneous system is observed.

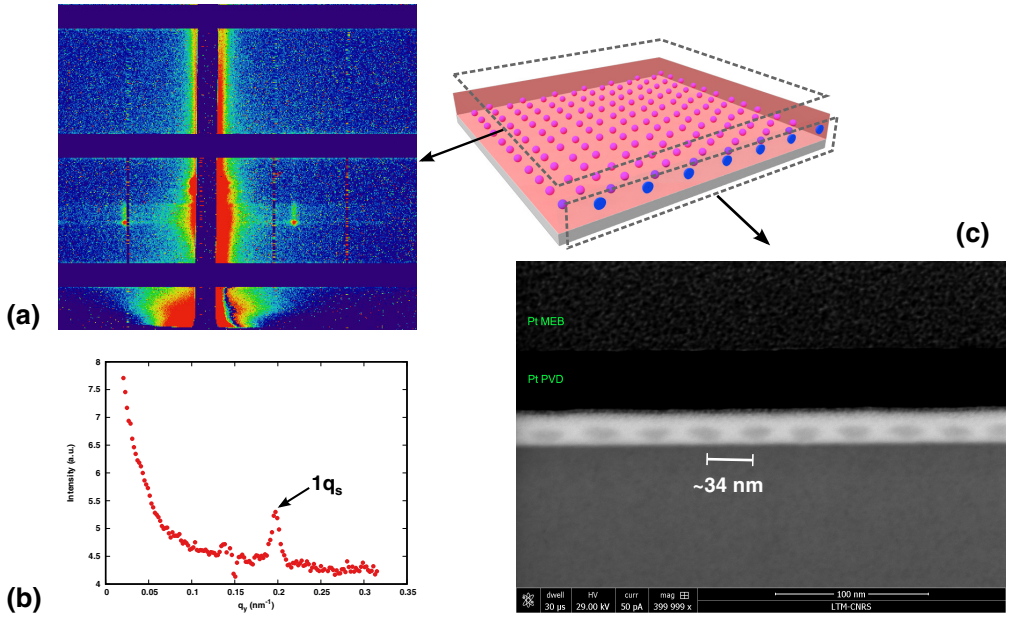

Figure 2.2.: Grazing incidence small angle X-ray scattering measurements : (a) GISAXS patterns and (b) its corresponding intensity profile of a DOS42 thin film. (c) Cross-section STEM image of the DOS42 thin film.

Due to the negligible vapor pressure of DOS and its good solubility with the PS block (Table 2.1), retention of DOS molecules in the PS matrix after spin was considered. DOS42 thin films were then studied by in situ ellipsometry. We observed that the as-spun plasticized film is twice as thick as its reference without DOS at *RT* (Fig. 2.3c). As predicted by the plasticizer theory, DOS only increases the free volume of the PS block, and decreases its T_g to *RT* or lower [13].

Consequently, the PS volume fraction increases and the BCP system phase-separates in a spherical metastable morphology according to the phase diagram predicted by self-consistent mean field theory [14]. This mechanism is similar to an SVA treatment with PS-selective solvents. The solvent molecules enter into the PS chains, giving sufficient mobility to self-assemble by swelling selectively the PS matrix and reducing its T_g [15]. Thus, the combination of PS selectivity and the low evaporation rate of plasticizer sets the PS matrix in a glass-liquid state where PS-*b*-PDMS micelles have sufficient mobility. This reduces the kinetics of self-assembly drastically to the hexagonal spheric morphology.

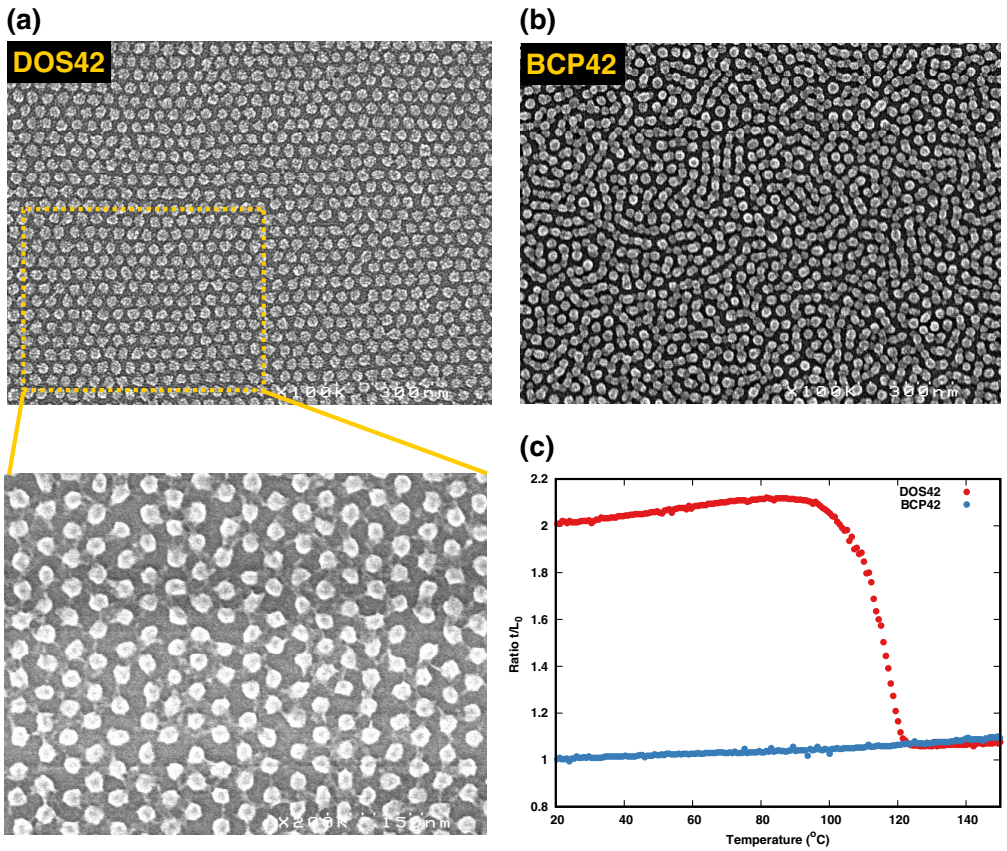

Figure 2.3.: (a) Top view SEM images of BCP thin films after the two-step plasma etching: DOS42 and (b) its reference BCP42. (c) Temperature profile of BCP42 and DOS42 film thickness by in-situ ellipsometry.

Thermal treatments

As seen in the zoomed fig. 2.3a, DOS seems to misshape interfaces between PS and PDMS. This is observed through the presence of residues around oxidized PDMS spheres, which could be troublesome for lithographic applications. The complete elimination of DOS from the BCP pattern is important to fabricate long-range ordered lithographic masks. For this reason, the evaporation of DOS was tested by thermal annealing on the DOS42 thin films.

Earlier, the DOS42 thin film was thermal annealed at a heating rate of 1 ℃/s under in-situ ellipsometry measurements for thickness control (fig. 2.3), where it was determined that DOS starts evaporating at $\sim$ 100 ℃. Then, the DOS42 thin films were heated at different temperatures (110–140 ℃) for 60 s, and the thickness was measured in-situ by ellipsometry (Fig. 2.4). Upon heating, the thin film thickness rapidly decreases after a first thermal expansion, suggesting an evaporation of DOS.

Evaporation rates depend on the temperature, as demonstrated in fig. 2.4. At 130 and 140 ℃, the PS-PDMS film rapidly drops from $2.2L_0$ to the monolayer thickness L_0, whereas at 110 and 120 ℃, DOS is not completely evaporated after 1 min. In addition to the thickness measurements, the morphology state has been observed by SEM for 30 s and 60 s of TA. A morphology evolution was observed in the DOS42 system from spheres to cylinders at 120 ℃ (from fig. 2.4c to fig. 2.4d) until reaching complete cylindrical morphology after 60 s of TA. This suggests an upper limit of $\approx 1.6L_0$ to have a morphological evolution. Then, faster transitions were found upon heating at 140 ℃ for 30 s.

The morphology obtained as-spun is trapped in an ordered metastable state. By heating, the plasticizer contained in the PS corona of the micelles starts to evaporate, thus increasing the PDMS volume fraction f_{PDMS}. According to the calculation of Liaw and co-authors [16], for a solvated BCP system, an increase in f_{PDMS} results in an increase of f_{core} and consequently triggers a morphology transition from spheres to cylinders when the system is already confined in a hexagonal spheric packing. After calculations from ellipsometry measurements, a morphology transition occurs at $f_{PDMS} \approx 0.18$, when the BCP42 thin film is swollen by DOS, which is consistent with the cylinder-sphere transition in the BCP phase diagram at χN=116 [17].

Heating for 60 s at 140 ℃ eliminates the PDMS residues on the maintained cylindrical

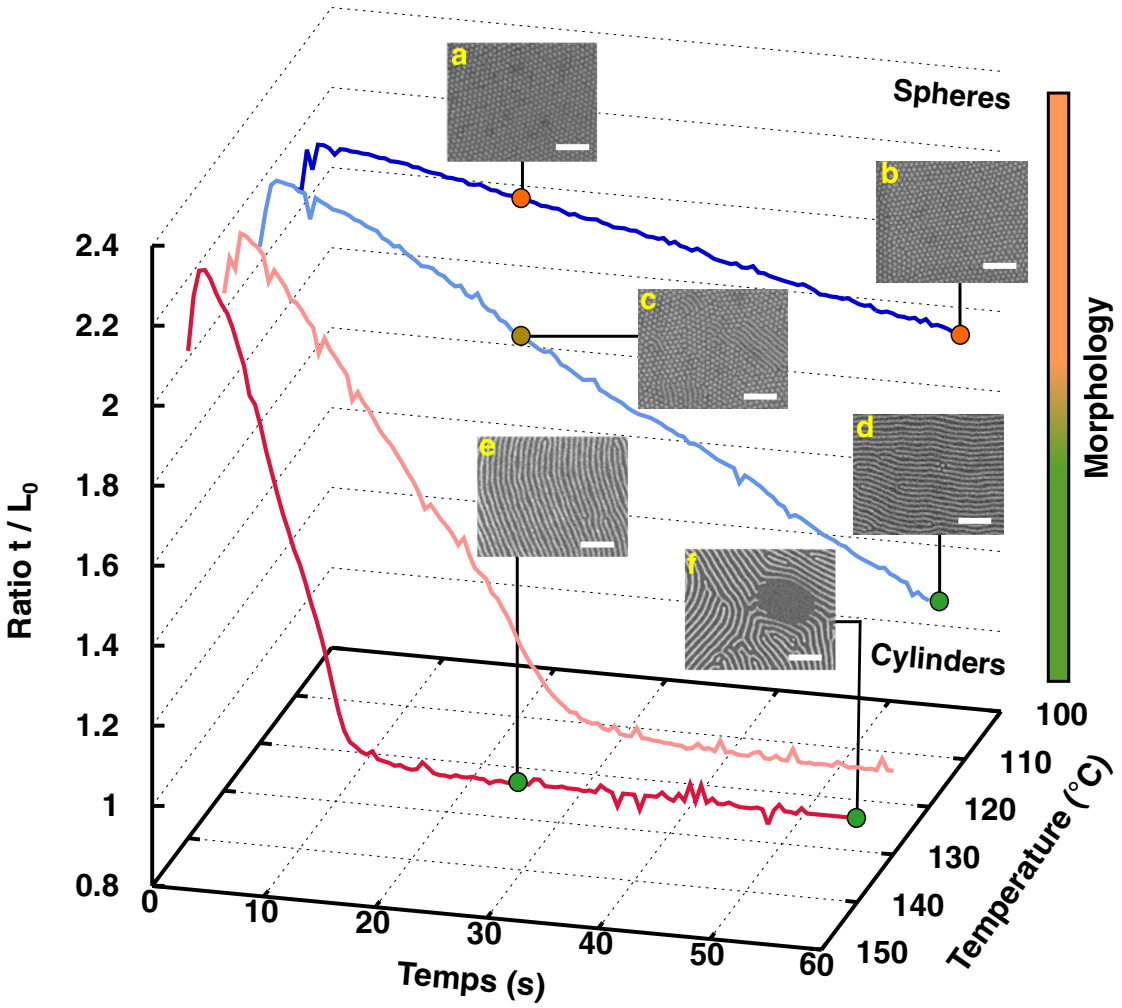

Figure 2.4.: Main image: Kinetics of film thickness of PS-*b*-PDMS 42 kg/mol with DOS under thermal annealing for temperatures between 110–140 °C by in-situ ellipsometry. Top-view SEM images of PS-*b*-PDMS after 30 s (a,c,e) and 60 s (b,d,f) of thermal annealing in the range 110–140 °C. Scale bar corresponds to 200 nm.

morphology as well, but dewetting appears at this stage (despite $t \sim L_0$, according to Fig. 2.4f). Since DOS was completely evaporated at ∼15 s, the relaxation of the PS matrix is reduced. For longer annealing times above 30 s, PDMS residues tend to decrease contact forces with the PS block by diffusing to PDMS cylinders. This long-range residual stress from non-equilibrium chain conformations might play a role in the instability of the BCP42 thin film, and dewetting occurs by the formation of holes as observed in Fig. 2.4e [18, 19].

Morphology transition by thermal annealing was tested using a sphere-forming BCP. DOS was solvated with BCP70 (both 1%wt) in PGMEA to form the DOS70 solution. Under same conditions than DOS42, a DOS70 thin film was thermally annealed at 150 ℃ during 30 s. In contrary to DOS42, the as-spun DOS70 thin film generates a disordered spherical morphology (fig. 2.5a). The BCP phase diagram in the high-segregation regime ($\chi N > 100$) is displayed in fig. 2.5 to illustrate the morphology transition. The addition of DOS, decrease the f_{PDMS}, placing it in the disordered phase of the BCP diagram. With the rapid thermal annealing, DOS evaporation generates at the same time a shift in the f_{PS} where its equilibrium morphology was obtained (fig. 2.5b) with the absence of any residues (Fig. 2.5 only shows a trend without the possible variations of χ).

From a formulation point of view, this result is of significant relevance in the use of plasticizers, as it is possible to target an initial morphology from the phase diagram, which is trapped as-spun; or to obtained the stable morphology of a BCP by the rapid thermal annealing. Additionally, this last experiment with a spherical BCP give us indications about the importance of an enhanced kinetics and a good initial order. Indeed, we observe the plasticizer to enhance the kinetics in both cases, but a better order is achieved with the cylindrical system (BCP42), certainly due to a better initial order.

2.3.2. Influence of DOA on self-assembly

To take advantage of plasticizer effects on PS-*b*-PDMS self-assembly while avoiding at the same time poor microseparated structures or dewetting issues, other plasticizers were tested on PS-*b*-PDMS. Among them was DOA which, from its physical properties, is slightly more PS selective than DOS ($\chi_{\text{PS-DOA}} = 0.04$ and vapor pressure 110 μPa from Table 2.1). DOA was tested in the same conditions as DOS and its effect on PS-*b*-PDMS self-assembly was studied.

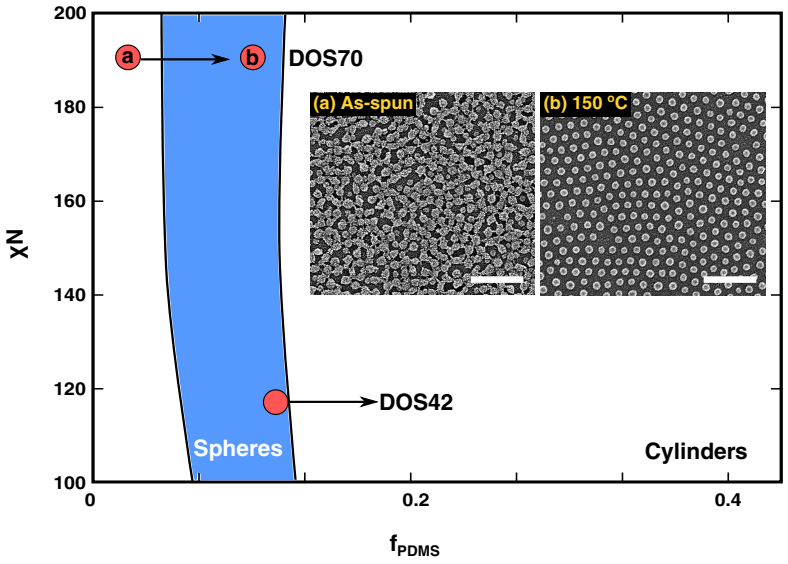

Figure 2.5.: Main image: BCP phase diagram in the high-segregation regime ($\chi N > 100$). Morphology transition of the plasticized solution PS-*b*-PDMS 70 kg/-mol with DOS: Top-view SEM images of their (a) as-spun thin film and (b) after thermal annealing during 30 s at 150 °C. Scale bar corresponds to 200 nm.

Fig. 2.6a shows a hexagonally packed lattice of oxidized-PDMS spheres observed on a plane surface. As-spun images show microseparated structures without PDMS residues after plasma etching. The faster evaporation rate of DOA in vacuum allowed to process the samples directly in the plasma chamber without intermediate steps, which is of main interest for high throughput. A SEM top-view image of the as-spun DOS42 (BCP42 with DOA) thin film on a graphoepitaxial surface is shown in fig. 2.6c, where the directed self-assembly is demonstrated, maintaining the hexagonal spheric morphology without postcoating annealing treatments. In this way, nanolithographic masks by self-assembly were fabricated effortlessly.

Similar to observations for DOS, DOA led to a transitional phase from spheres to cylinders by rapid TA (figs. 2.6b-d). BCP42 is located in the strong segregation limit with χN=116; therefore chain mobility is retarded and suffers from slow kinetics of self-assembly during TA. With the use of DOA, the PS-*b*-PDMS thin film remains swollen after spin-coating, which induces the hexagonal spheric self-assembly. During TA, high PS selectivity of DOA allows mobility in the PS matrix and greater relaxation times for PDMS chains to diffuse. Morphology transition occurs before the complete evaporation

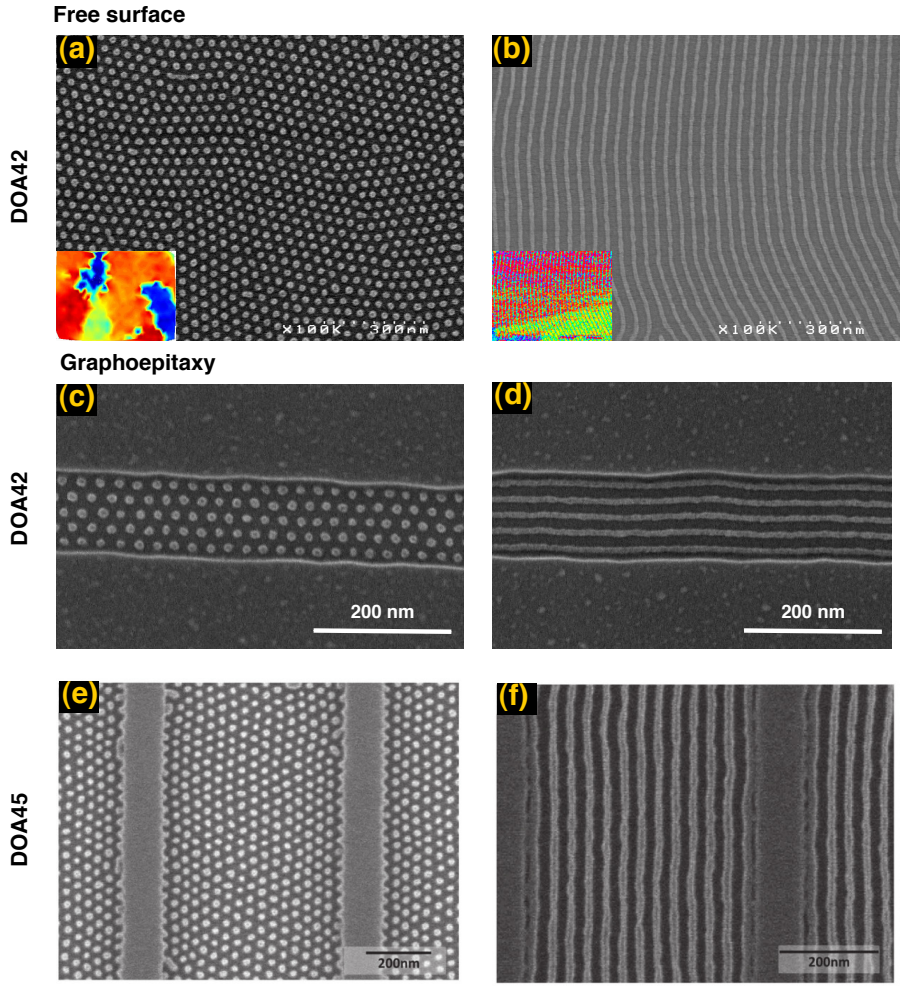

Figure 2.6.: SEM top view images of the self-assembly of different PS-PDMS thin films with DOA. Self-assembly on a plane surface: (a) as-spun DOA42 and (b) after the rapid thermal annealing (30s at 110 °C). Inset figures correspond to the orientation maps of the polymer grains. Directed self-assembly within Si guiding lines: (c) as-spun DOA42 and (d) after the rapid thermal annealing. Directed self-assembly within SOC guiding lines: (e) as-spun DOA45 and (f) after the rapid thermal annealing.

of the plasticizer, as was shown with DOS in fig. 2.4; the stable cylindrical morphology is trapped when the plasticizer is removed. Due to higher PS selectivity and evaporation rate of DOA compared to DOS, lower temperatures sufficed for phase transition (30 s at 110 °C). Thus, dewetting phenomena were avoided and a good alignment retained in both figs. 2.6b-d.

Under same experimental conditions than DOA42, a DOA45 thin film was tested (BCP45 + DOA). The same results than DOA42 were observed, were a hexagonal spherical morphology was obtained as-spun, and the cylindrical morphology obtained by rapid thermal annealing (figs. 2.6e-f respectively). In both cases, the DOA45 was directed self-assembled within SiARC/SOC trenches in view of a possible transfer (sec. 2.3.3).

In the free energy F landscape, DOA minimizes the activation energy, thus allowing an easy exceeding of the free energy barrier to a new stable cylindrical state. This statement is schematically represented in fig. 2.7 where the free energy path of BCP42 and DOA are shown for illustrative purposes. The thermodynamics of the self-assembly process via microphase separation is represented by the Gibbs free energy equation $\Delta G_{SA} = \Delta H_{SA} - T\Delta S_{SA}$, where G is the Gibbs free energy required for self-assembly, H the enthalpy and S the entropy of the system at temperature T. In order to exceed the free energy barrier to reach the free energy minimum of the stable cylindrical morphology, the enthalpy changes have to be positive [20]. Since the micelles as-spun are already in a hexagonal spheric packing, the entropy contribution becomes negligible (red path in fig. 2.7).

The free energy required for the morphology transition depends mainly on the enthalpy change associated with the chain crossing over the interfaces between PS and PDMS [14]. These interactions appear only locally at the molecular scale (sharp PS-*b*-PDMS interfaces) when the BCP system is already ordered, and the PDMS chains easily diffuse into the swollen PS matrix via the interface diffusion mechanism, to generate a cylindric morphology. Indeed, the stable cylindrical morphology for BCP42 thin films was never observed by using thermal annealing, which indicates the large free energy barrier needed to be overcome to attain the free energy minimum value (blue path in fig. 2.7).

Defects in the cylinder morphologies of the DOA42 thin films were analyzed with the ImageJ plug-in developed by Murphy *et al.* [21]. This plug-in is capable to identify three main types of defects involved during the self-assembly process of horizontal cylinders:

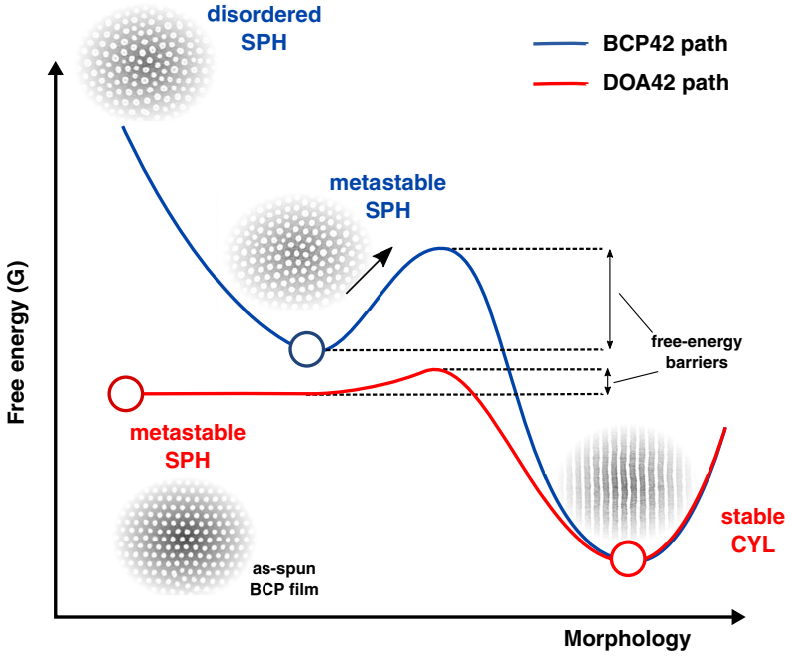

Figure 2.7.: Schematic representation of the free energy landscape of the BCP42 and DOS42 thin films as a function of the obtained morphology.

the dots, the end-point defects and the junctions [17]. In fig. 2.8a, a SEM image was analyzed, and defects quantified in fig. 2.8b. Despite fast cylinder formation, mainly end-point defects of the PDMS cylinders were observed, which generates at the same time a PS junction. This kind of dislocation appears mostly at grain boundaries, where an excess of free energy sets up and obstructs the rejoining of domains [22], usually interpreted as free energy local minima of the landscape schematized in fig. 2.7 [23].

End-point defects of the PDMS cylinders seems to be a characteristic flaw during the morphology transition, as they also appear in graphoepitaxy. In the case of DSA, the PDMS chains diffuse from spheres to cylinders in the parallel direction of the guiding lines for the morphological transition (fig. 2.8c). In this case, the passage from spheres to cylinders emphasizes the fact that the interface interactions related to the phase change are only local. The creation of defects during the morphology transition, generates a propagation of the error, which impacts on the directed self-assembled cylinders (figs. 2.8d). Otherwise, defects in the topographical lines for graphoepitaxy could create defects in the starting structure, and then create the end-point defects (fig. 2.8e).

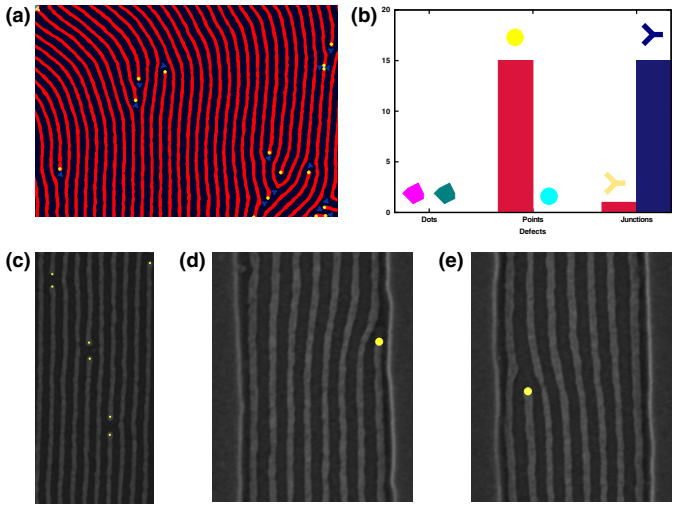

Figure 2.8.: (a) Automation of defects by imagery treatment from a top view SEM image of self-assembled cylindrical DOA42, and (b) corresponding defects quantified such as dots, ended-points and junctions. (c-e) main defects occurred during the DSA of DOA42 by graphoepitaxy.

2.3.3. Transfer on silicon

The applicability of BCP self-assembly lithography assisted with plasticizers is presented through the complete process from PS-*b*-PDMS deposition to the final pattern transfer etching. To exemplify the nanolithography principle, masks showed in the figs. 2.5b and 2.6f are used.

In both cases, the free surface and graphoepitaxy, an underlayer is used. SOC is a carbon-based resist. It has became common to use an intermediate hardmask to transfer patterns into silicon by plasma etching [24]. By using a SiARC/SOC hardmask stack, a considerable increase in achievable aspect ratio is possible [25]. SOC has strong chemical similarities to PS and shows thus a favored wetting of this block, so SOC acts as a PS brush layer.

For the spherical-forming mask DOS70, three steps were necessary to transfer the PDMS template to Si. First, the elimination of the PDMS surface layer by a CF_4 plasma for 5 s at 4 mTorr with a gas flow rate of 100 sccm at 700 W plasma power. The second step eliminates the unprotected PS matrix and transfers the PDMS spheres patterns into the SOC layer (fig. 2.9a). This is made by using a HBr-O_2 blend plasma composed of 70 sccm of O_2 and 30 sccm of HBr. This second step is realised during 25 s

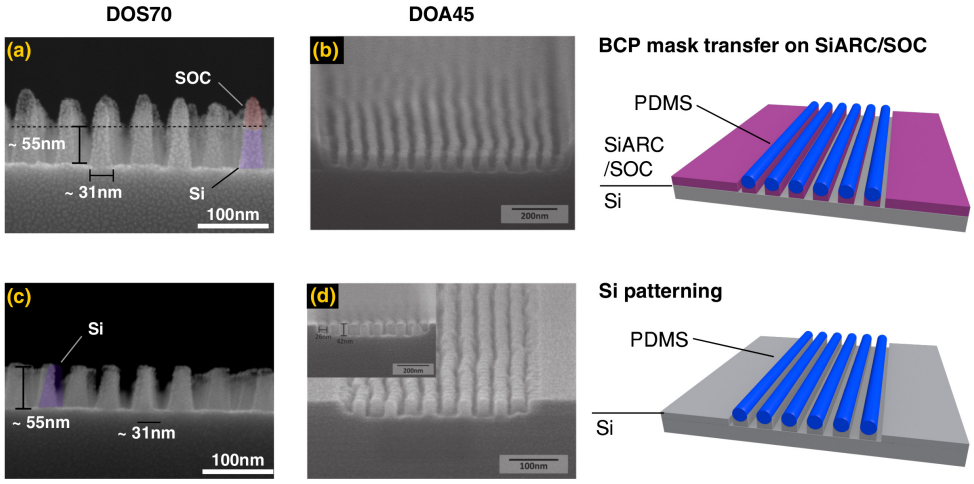

Figure 2.9.: Transfer of the PDMS patterns on Silicon: cross-section SEM images of the (a-b) spherical DOS70 and cylindrical DOA45 BCPs transfered on SOC, respectively and (c-d) their subsequent transfer on Si.

at 5 mTorr power of 500 W. Finally, third step consists in pattern transfer into Si, with a HBr-O_2 pulsed plasma during 80s to transfer on $\sim$ 55nm of Si (fig. 2.9c).

The obtained patterns of DOA45 in fig. 2.6f were used as etching mask in order to transfer the long-range cylindrical features into the silicon substrate. First, the PDMS top wetting layer at the air/BCP interface is removed by CF_4 plasma, and then HBr/ O_2 plasma was applied to remove the PS matrix and transfer the pattern in the underlying SOC layer. Simultaneously, the PDMS mask is oxidized. Fig. 2.9b shows the cross-sectional SEM image of DOA45 mask after the SOC transfer step. The SOC layer is completely open, and anisotropic nanopillars with a good CD control are obtained.

Plasma of CHF_3/SF_6/Ar was used to etch Si selectively, relative to the SiO_x/SOC mask. A successful proof of concept of the Si pattern transfer for DOA45 is shown in fig. 2.9b. $\sim$ 42 nm height nanopillars were obtained with $\sim$ 26 nm width for DOA45, which confirms the good CD control is maintained during etch.

2.4. Summary

Commercial plasticizers such as dioctylsebacate (DOS) and diisooctyl adipate (DOA) were blended with PS-PDMS polymers, and their influence on the self-assembly process was investigated. The intrinsic PS selectivity of the plasticizers brings the BCP to form PS-PDMS micelles, which results in highly ordered self-assembled hexagonal spherical PS-PDMS after spin-coating without any annealing. The negligible vapor pressure of plasticizers and the decrease of T_g allow the high mobility of PS-PDMS micelles in thin films. A transition into a stable horizontal cylindrical morphology is then possible by a rapid thermal annealing (30 s). The complete process, from the BCP deposition to the final pattern transfer into Si, was presented which makes this method promising for microelectronic industrial integration.

Bibliography

[1] D. B. Wright, J. P. Patterson, A. Pitto-Barry, A. Lu, N. Kirby, N. C. Gianneschi, C. Chassenieux, O. Colombani, and R. K. O'Reilly, Macromolecules **48**, 6516 (2015).

[2] H. Tanaka, H. Hasegawa, and T. Hashimoto, Macromolecules **24**, 240 (1991).

[3] T. Hashimoto, H. Tanaka, and H. Hasegawa, Macromolecules **23**, 4378 (1990).

[4] J. Yang, Q. Wang, W. Yao, F. Chen, and Q. Fu, Applied Surface Science **257**, 4928 (2011).

[5] J. M. Kim, Y. Kim, W. I. Park, Y. H. Hur, J. W. Jeong, D. M. Sim, K. M. Baek, J. H. Lee, M.-J. Kim, and Y. S. Jung, Advanced Functional Materials **25**, 306 (2015).

[6] C.-C. Ho, S.-J. Wu, S.-H. Lin, S. B. Darling, and W.-F. Su, Macromolecular Rapid Communications **36**, 1329 (2015).

[7] T. Ghoshal, C. Ntaras, M. T. Shaw, J. D. Holmes, A. Avgeropoulos, and M. A. Morris, J. Mater. Chem. C **3**, 7216 (2015).

[8] E. H. Immergut and H. F. Mark, in *Plasticization and Plasticizer Processes* (American Chemical Society, 1965) Chap. 2, p. 1.

[9] G. Wypych, *Handbook of Plasticizers* (William Andrew, 2013) p. 800.

[10] J. Brandrup, E. H. Immergut, and E. A. Grulke, *Polymer Handbook*, 4th ed., Vol. 2 (Wiley-Blackwell, New York, NY, 1999) p. 2336.

[11] Y. Fukumine, K. Inomata, A. Takano, and T. Nose, Polymer **41**, 5367 (2000).

[12] T. M. Bennett, K. S. Jack, K. J. Thurecht, and I. Blakey, Macromolecules **49**, 205 (2016).

[13] A. Schausberger and I. V. Ahrer, Macromolecular Chemistry and Physics **196**, 2161 (1995).

[14] F. S. Bates and G. H. Fredrickson, Physics Today **52**, 32 (1999).

[15] W. Bai, K. G. Yager, and C. A. Ross, Macromolecules **48**, 8574 (2015).

[16] C. Y. Liaw, K. J. Henderson, W. R. Burghardt, J. Wang, and K. R. Shull, Macromolecules **48**, 173 (2015).

[17] E. W. Cochran, C. J. Garcia-Cervera, and G. H. Fredrickson, Macromolecules **39**, 2449 (2006).

[18] P. Damman, S. Gabriele, S. Coppée, S. Desprez, D. Villers, T. Vilmin, E. Raphaël, M. Hamieh, S. A. Akhrass, and G. Reiter, Physical review letters **99**, 036101 (2007).

[19] A. Sharma and G. Reiter, Journal of Colloid and Interface Science **178**, 383 (1996).

[20] M. Rubinstein and R. H. Colby, *Polymer Physics* (OUP Oxford, 2003).

[21] J. N. Murphy, K. D. Harris, and J. M. Buriak, PLOS ONE **10**, e0133088 (2015).

[22] W. Li and M. Müller, Annual review of chemical and biomolecular engineering **6**, 187 (2015).

[23] V. Mishra, G. H. Fredrickson, and E. J. Kramer, ACS Nano **6**, 2629 (2012), pMID: 22339501.

[24] A. Frommhold, J. Manyam, R. Palmer, and A. Robinson, Microelectronic Engineering **98**, 552 (2012).

[25] A. Frommhold, R. E. Palmer, and A. P. G. Robinson, Journal of Micro/Nanolithography, MEMS, and MOEMS **12**, 033003 (2013).

3. Graphene electronics

3.1. Introduction

Current manufacturing infrastructure of semiconductor industry has became extremely expensive due to the highly complexity of IC fabrication and the technological steps involved, already detailed in chap. 1. There is a clear consensus in the semiconductor community that FET scaling is approaching its limits and that there is a need to introduce new materials, device concepts and designs to ensure scaling of ICs to continues on. Furthermore, efforts in performance improvements have motivated to the chip-makers to introduce devices based on materials with different physics other than silicon.

In this context, a novel lithography technique was proposed and studied in the last chapter, breaking up the top-down fabrication paradigm, in order to cheapen cost and ensure scaling of ICs in the sub-20 nm regime and beyond. Classical substrates in which the BCPs have been employed includes silicon, silica, quartz and alumina. Several works of my research group have demonstrated the patterning of these typical materials from different templates such as spherical and cylindrical PS-*b*-PDMS or cylindrical PLA-PDMS.

Towards a post-silicon era, the community looks on two-dimensional materials for their amazing electronic and mechanical properties but above all, the possibility they offer to assure the downsizing for the next several future generations of of FETs and related devices. As these materials have been studied, real needs of patterning 2D materials in the sub-20 nm to replace silicon as semiconductor material emerged, among them the most popular one: graphene. This chapter exposes the needs of graphene patterning as a way to exploit its electronic properties and a possible integration on current FETs.

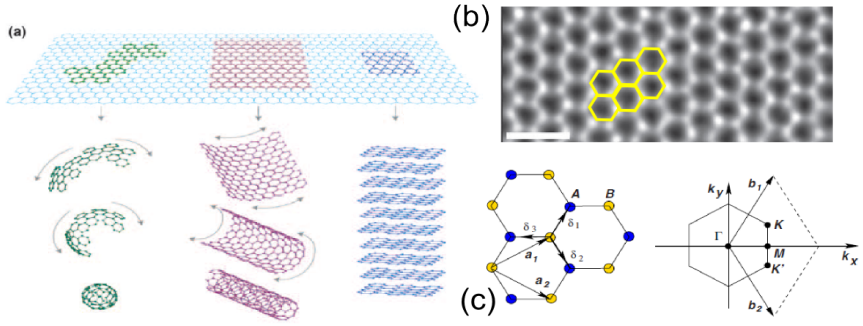

Figure 3.1.: (a) Schematic drawing of the relationship between graphene and other carbon materials. G is a 2D building material for carbon materials of all other dimensions. It can be wrapped up into 0D buckyballs, rolled into 1D nanotubes or stacked into 3D graphite [3]. (b) Lattice structure of G under TEM showing its hexagonal lattice [4]. (c) Lattice structure of G, made out of two interpenetrating triangular lattices ($\boldsymbol{a}_1$ and $\boldsymbol{a}_2$ are the lattice unit vectors, and $\sigma_i, i = 1, 2, 3$ are the nearest-neighbor vectors), at the right the corresponding Brillouin zone. The Dirac cones are located at the $\boldsymbol{K}$ and $\boldsymbol{K'}$ points.

3.1.1. Main concepts

Graphene is a two-dimensional material composed by a monolayer of carbon atoms. It is the 2D building block for sp^2 carbon allotropes (fig. 3.1a), and its atoms are packed in a characteristic honeycomb crystal lattice [1]. Graphene had been presumably inexistent in its free state before the isolation of graphene sheets by Novoselov, Geim and co-workers in 2004 at the University of Manchester [2]. Graphene researches impacted directly the electron-device community, as was discovered its singular electronic transport properties and the flexibility of its bonds.

Carbon atoms in graphene are arranged in a hexagonal lattice which has already been observed by TEM (fig. 3.1b). From graphene lattice structure in fig. 3.1c, the unit cell structure can be seen as a triangular lattice with two equivalent atoms. The unit vectors in the direct and reciprocal lattice are written respectively as,

$$\boldsymbol{a}_{1,2} = \frac{a}{2}(3, \pm\sqrt{3}), \boldsymbol{b}_{1,2} = \frac{2\pi}{3a}(1, \pm\sqrt{3}) \tag{3.1}$$

where atoms are about $a \approx 1.42$ Å apart.

The two-dimensional electron dispersion relation of a graphene monolayer was calculated in 1947 by Wallace [5]. It is expressed by the nearest neighbor tight-binding Hamiltonian

$$E(\boldsymbol{k}) = E_F \pm t\sqrt{1 + 4\cos(\frac{\sqrt{3}k_x a_0}{2})\cos(\frac{k_y a_0}{2}) + 4\cos^2(\frac{k_y a_0}{2})} \tag{3.2}$$

where t is the coupling integral between the nearest atoms and has typical values between 2.9-3.1 eV, and a_0 is the lattice constant of the hexagonal lattice with value of 2.46 Å. The electron dispersion relation is plotted in fig. 3.2a.

Graphene stability is due to its tightly carbon atoms bounds and its sp^2 orbital hybridization network. This hybridization is a combination of the (s, p_x, p_y) orbitals which constitutes the σ-bond and the p_z orbital that forms the out-of-plane π bond. The plus sign applies to the upper $(\pi*)$ and the minus sign the lower (π) band [6].

Of particular importance are the vectors $\boldsymbol{K}$ and $\boldsymbol{K'}$ that are called the Dirac points with positions in the momentum space of the first Brillouin zone given by

$$\boldsymbol{K} = (\frac{2\pi}{3a}, \frac{2\pi}{3\sqrt{3}a}), \boldsymbol{K'} = (\frac{2\pi}{3a}, -\frac{2\pi}{3\sqrt{3}a}) \tag{3.3}$$

The existence of the two Dirac points at K and K', where the Dirac cones for electrons and holes meet each other, means zero bandgap. In fig. 3.2b is shown the symmetry between the valence and conduction band.

For small k relative to the Dirac point, the dispersion relation is given by

$$E_\pm = \pm\hbar v_F \boldsymbol{K} \tag{3.4}$$

where v_F is the Fermi velocity, given by $v_F = 3ta/2h$, with a value $v_F = 1\text{x}10^6$ m/s. This result was first obtained by Wallace.

The most important aspect of graphene energy dispersion is its linear energy-momentum

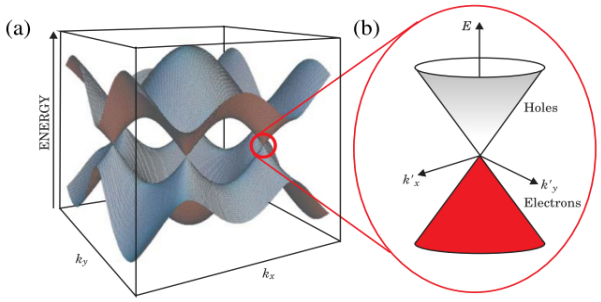

Figure 3.2.: (a) A band-structure picture of the crystal describes the energy dependence of that electronic motion. A semimetal, graphene has valence and conduction bands that just touch at discrete points in the Brillouin zone. (b) The energy-momentum dispersion relation becomes linear in the vicinity of those points, with the dispersion described by the relativistic energy equation. Consequently, an electron has an effective mass of zero and behaves more like a photon than a conventional massive particle whose energy–momentum dispersion is parabolic [10].

relationship with the conduction and valence bands intersecting at $k = 0$ [7]. Graphene is thus a zero band-gap semiconductor with a linear, rather than quadratic, energy dispersion for both electrons and holes in the conduction and valence bands (see figure 3.2). Another interesting property from eq. 3.4 is that its low-energy excitations are massless, chiral, Dirac fermions [8, 9].

3.1.2. Relevant properties and applications

Graphene is an appealing material for the developing of devices because it offers several advantages compared with other semiconductor materials, detailed as follows:

Mobility

The most frequently stated advantage is its high carrier mobility at room temperature. In graphene, the electron and hole mobility are equally high, due to the symmetric band structure. Theories have predicted that the phonon limited mobility in graphene can be as high as 2×10^5 cm^2/(V$\cdot$ s) at a carrier concentration of 10^{12} cm^{-2} and similar mobility value has already been measured experimentally in the absence of charged impurities and ripples [11]. Elsewhere, mobilities of 1×10^4 cm^2/(V$\cdot$ s) are routinely measured

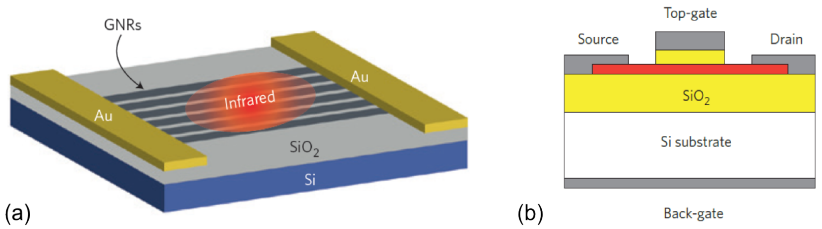

Figure 3.3.: (a) Schematic illustration of a nanoribbon-array infrared photodetector, photodetection enhancement by metallic plasmonic nanostructures and intrinsic plasmons [20]. (b) Schematics of a top-gated graphene MOSFET with a channel of graphene grown on metal and transferred to a SiO2-covered Si wafer [21].

for exfoliated graphene on SiO_2-covered silicon wafers (vs. 1.3×10^3 $cm^2/(V \cdot s)$). Its high mobility makes graphene a potential candidate in electronic applications, including radiofrecuency field-effect transistors (FET) [12].

Bandbap

The absence of gap in the graphene electronic band structure enables charge carrier generation by light absorption over a wide energy spectrum, unmatched by any other material [13]. Furthermore, since the density of states is vanishing at the Dirac points, the Fermi energy can be tuned by carrier density via electrostatic doping and wavelength-independent absorption [14, 15]. With a combination of high conductivity and transparency, graphene is expected to find applications in transparent conducting films [16], as a possible candidate to replace the increasingly costly indium tin oxide (ITO) based films. A variety of prototype optoelectronic devices have already been demonstrated (fig. 3.3a), such as transparent electrodes in displays [17], ultrafast lasers [18] and plasmonic devices [19].

Graphene properties detailed below are remarkable, but they require closer inspection. Because the bandgap is zero, it places a major obstacle in developing logic applications. FET devices with channels made of large-area graphene cannot be switched off and making them unsuitable for logic transistors. However, the band structure of graphene can be modified, and it is possible to open a bandgap. Numerous ways of opening a band gap have been investigated, such as doping or patterning. This topic will be the focus of discussion in the next section.

3.1.3. Graphene-based electronics

A FET should respond quickly to variations in V_{GS}, this requires short gates and fast carriers in the channel. Any successor to silicon must have excellent switching capabilities, as well as an on-off ratio, I_{on}/I_{off} , between 10^4 and 10^7. In a conventional FET, this requires semiconducting channels with a sizeable bandgap, preferably 0.4 eV or more [21].

The band structure of graphene can be modified, making possible a finite bandgap opening. Since the density of the states is vanishing at the Dirac points, the Fermi energy can be tuned by carrier density via a molecular doping [22, 23, 24]. Moreover, confined Dirac electrons in graphene, constraint by the edges boundaries on the tranverse motion, opens up a bandgap by quantum interferences [25], i.e. very narrow graphene structures.

It has been predicted [26, 27], that graphene nanoribbons (GNR) have a bandgap that is, to a good approximation, inversely proportional to the width of the nanoribbon [28]. Below a width of about 15 nm, bandgaps can be fitted by

$$E_G = \frac{\alpha}{w_{GNR}} \tag{3.5}$$

where α is an experimental fitting parameter, usually between 0.4 and 2, w_{GNR} is the ribbon width in nm and E_g is the bandgap energy in eV. Fig. 3.4 resumes both experimental and theorerical data for different GNR studies. It shows a pronounced dependence of the bandgap energy with the width.

Ideal GNRs are classified by their chirality orientation [30], that is when a graphene layer is terminated by zigzag edges on both sides, it is refered as zigzag GNR, otherwise the armchair GNR has armchair-shaped edges. Fig. 3.5 shows both GNR chiralities: armchair (fig. 3.5a) and zigzag (fig. 3.5b). The properties of GNRs highly depend on shape and edge shape.

However, it should be noted that real nanoribbons have rough edges and widths that change along their lengths. Even modest edge disorder obliterates any difference in the bandgap between nanoribbons with different edge geometries [32], and edge functionalization and doping can also affect the bandgap [33]. A short length of mixed edge reduces likewise the ON-OFF current ratio.

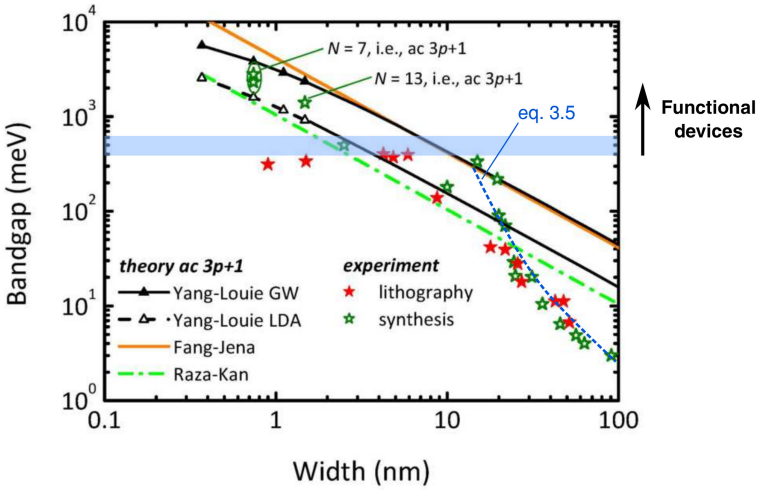

Figure 3.4.: Bandgap energy versus ribbon width for GNRs (adapted from [29]).

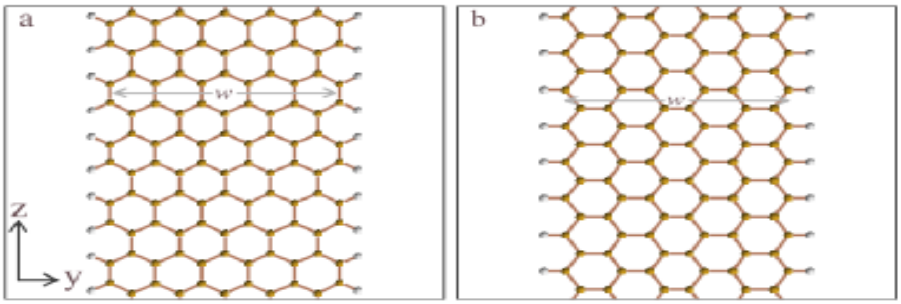

Figure 3.5.: (a) An armchair graphene nanoribbon which has dimer lines making up its width w. (b) A zig-zag GNR which has 6 zigzag chains alon the z direction. Adapted from [31]

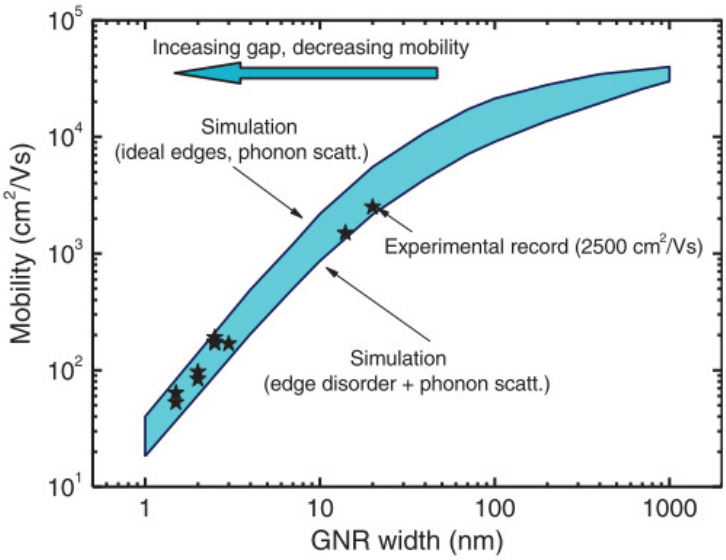

Figure 3.6.: Mobility versus ribbon width for GNRs. Adapted from [35]

Another important aspect to approach on GNRs is about carrier transport. It it questionable for perfect nanoribbons if they are adapted for electronics applications. In general, the larger the bandgap that opens in a nanoribbon, the more the valence and conduction bands become parabolic (rather than cone-shaped): this decreases the curvature around the K point and increases the effective mass of the charge carriers [34], which is likely to decrease the mobility.

Fig. 3.6 shows simulated and measured GNR mobilities as a function of ribbon width (note the good agreement between simulation and experiment). As point of comparison, record mobility on GNRs is 2500 $\mathrm{cm}^2/(\mathrm{V}\cdot\ \mathrm{s})$, lower than the mobility measured on graphene sheets ($1 \times 10^4\ \mathrm{cm}^2/(\mathrm{V}\cdot\ \mathrm{s})$).

Mobility and speed should be the subject of a compromise to develop GNR-FETs. The most attractive characteristic of graphene for use in MOSFETs for exemple, in particular those required to switch off, may be its ability to scale to shorter channels and higher speeds, rather than its mobility.

3.2. State of the art

To open a bandgap useful for conventional field-effect devices (> 0.4 eV), very narrow GNR with well-defined edges are needed. This issue represents a serious challenge given the technological capability available at the moment in the semiconductor industry. The fabrication of GNR channels with a certain length and the production of dense arrays of ordered nanoribbons still remains a significant challenge [36].

Various techniques have been developed to produce and control GNR or lattices, e.g., block copolymer lithography, nanosphere lithography, nanoimprint lithography and e-beam lithography. Next subsections focuses on the graphene patterning techniques, in particular these allowing sub-10nm GNRs fabrication such as block copolymer lithography and bottom-up synthesis with precursors.

3.2.1. Fabrication techniques

As described in sec. 3.1, GNR has a very special structure with very promising properties for technological materials. Accordingly, there are a lot of efforts in order to prepare GNRs easily with the required properties. Shortly after the discovery of GNRs properties, one after another different synthesis and fabrication methods have been developed to improve quality and to produce it at a large scale.

The most relevant methods of fabrication are summarized in table 3.1. Synthesis methods can be evaluated on the bases of different requirements [46]:

- on the purity of the graphene, which is defined by the lack of intrinsic defects, (*Quality*)
- aswell as on the size of the obtained flakes or layers (*Size*)
- one last attribute is the controllability of the method in order to achieve reproducible results (*Control*)

Basically there are three different approaches to preparing GNRs. On the one hand graphene can be detached from an already existing graphite crystal, the so-called exfoliation methods, and patterned by conventional lithography. On the other hand the GNRs can be grown directly on a substrate surface. The third approach is using CVD

Table 3.1.: GNR fabrication techniques and electric characteristics at RT.

Technique	**Advantage**	**Disadvantage**	**Width (nm)**	**Mobility (cm^2 Vs^{-1})**	**Bandgap (meV)**	I_{on}/I_{off}	**Ref.**
Mechanical exfoliation and lithography	Formation of high quality & single layer GNRs	Unscalable	~ 15		~ 200		[37]
Exfoliation & catalytic etching	Well-defined edges	Etching along crystallographic edges	~ 15				[38]
Metal-assisted etching	Aligned GNRs	Large and non-uniform width	20		~ 100	~ 7	[39]
Direct growth on SiO2	No substrate transfer	Formation of plateaus	20	1000	~ 50	~ 2	[40]
Growth on SiC trenches	Well-defined and precise dimensions	Limited to SiC substrate	~ 1.5		~ 500		[41]
Polymerization of molecular precursors	Bandgap similar to silicon	Unpredicted length	~ 1		~ 1300		[42]
CVD on germanium	High aspect ratio ($\sim$ 12nm)	Low control on GNR placement	8.2			~ 20	[43]
CVD & e-beam	Large-scale production	Low throughput	12	~ 100		~ 10	[44]
CVD & STM lithography	Narrow GNRs and defined crystallographic orientations	Edge roughness and unscalable	~ 3		~ 300		[45]

growth graphene and patterning using lithography methods listed above in table 3.1. This table recaps the techniques developed in the fabrication of GNRs, with the main advantages and disadvantages from a manufacturing point of view. Few of them are able to generates graphene nanostructures in the sub-10 nm, as it is discussed below.

3.2.2. Sub-10nm graphene patterning

Bottom-up synthesis

Bottom-up approach is essential for the generation of robust crystalline architectures with a well-defined structure that result from the self-assembly nature of various macromolecular architectures [47]. The recent developments efforts of this synthesizing GNRs method focus on well-controlled size, distribution, and geometry of the GNR edges.

In this process, GNRs are formed of monomeric precursors molecules that react at the surface of Au (111) or Ag(111). The synthesis mechanism consists in using DBBA (10,10'-dibromo-9,9'-bianthryl) or its derivatives, which are sublimated onto a slightly hot metallic surface ($\sim$ 200 ℃) to stimulate the production of linear polymeric chains after dehalogenation and C-C coupling. A subsequent higher temperature annealing ($\sim$ 400 ℃) favours the dehydrogenation of the polymer chains, resulting in graphene nanoribbons, as shown by a STM (fig. 3.8d) [48].

Atomically precise GNRs with different topologies and defined width and edge periphery can be obtained depending on the structure of the precursor, then narrow armchair GNRs (AGNRs) of few atoms width (9 and 13) synthesized by the bottom-up approach revealed that the ribbons have a large electronic bandgap of $\sim$ 1.3 eV [49].

Therefore, it is possible to fabricate defect-free GNRs on Au/Ag surfaces and organic solvents, but one of the main issue is to obtain the adequate precursor. The latest efforts reside in the catalyst-free bottom-up growth of GNRs [50], nevertheless the proposed methods continue being substrate-dependent and the risk of molecular residues from precursors in the graphene structures is not evoked. In all cases, the bottom-up synthesis path of GNRs fabrication leaves no possibility of large-scale production and the directional control of the GNRs is limited.

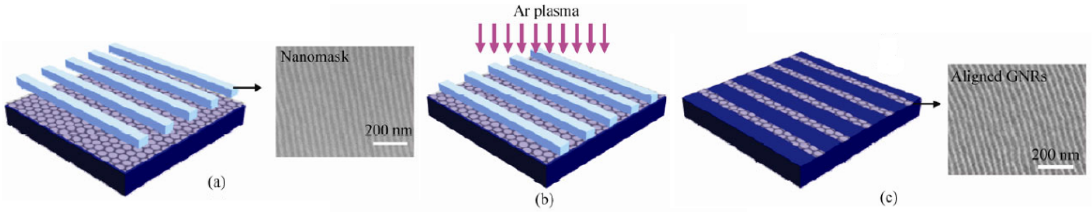

Figure 3.7.: Schematic process for patterning graphene using the oxidized PDMS nanomask. (a) The nanomask was put in intimate contact with peel-off graphene on a SiO2/Si substrate. The SEM image shows the well-aligned line array in the mask. (b) Ar plasma was used to transfer the patterns on the nanomask to the underlying graphene. (c) An aligned GNR array was obtained after lifting up the nanomask. The SEM image shows the GNR array made by this approach [51].

BCP lithography

The development of block copolymer lithography seems to respond properly to issues in the patterning of 2D materials such as graphene, as it is adequate for sub-10nm lithography on large surfaces, and then adaptable for device development.

Jiao *et al.* was the first group to fabricate GNR structures by BCP lithography and demonstrate their electrical properties [51]. The etch mask was derived from a cylinder-forming PS-*b*-PDMS BCP film. The aligned line structures of the mask self-assembled on a Au film and were etched by CHF_3 and O_2 plasma to removed the PS matrix and oxidize PDMS cylinders. They were then transferred on graphene by the "Scotch tape" method. Line patterning was then transferred to underlying graphene by Ar plasma etching, thus generating an array of dense parallel GNRs (GNR width $\sim$ 12 nm, pitch $\sim$ 35 nm) (fig. 3.7). Finally, the mask was lifted up, leaving GNR arrays on SiO_2/Si substrate without leaving obvious residue. The I_{on}/I_{off} current ratios of these devices were low since the $\sim$ 12 nm wide GNRs were not narrow enough to open up sufficient band gaps.

Further studies in fabricating GNR structures by BCP lithography were showed. Liang & Wi fabricated sub-10 nm half-pitch GNR [52]. They deposited a top cross-linking polymer on graphene, suitable for thermal nanoimprint lithography to direct the self-assembly of PS-*b*-PDMS. A silicon mold was applied to imprint 200 nm period grating features into the top polymer layer through a thermal imprint cycle. Afterward, the film of BCP was spun onto the prestructured underlayer, then the sample was thermally annealed to induce the microphase separation of PS and PDMS domains in the copolymer.

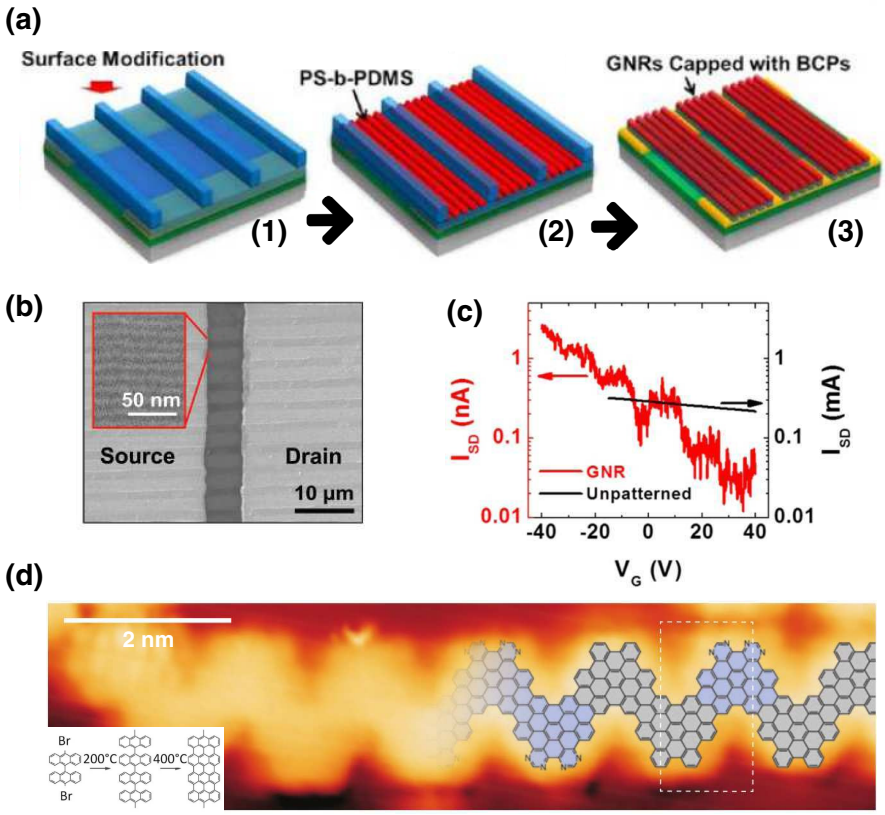

Figure 3.8.: The fabrication route for patterning sub-10 nm half-pitch graphene nanoribbons using directed self-assembly of block copolymers: (a) Directed self-assembly of PS-b-PDMS block copolymer. Before BCP spin-coating, the graphene surface was prepatterned with electrical contacts and an underlayer cross-linkable PMMA. (1) This polymer was nanoimprinted with directing nanostructures for (2) DSA of PS-b-PDMS with cylindrical segregating morphology. (3) plasma etching for patterning graphene nanoribbons using PDMS cylinders as the etching mask. Adapted from [52]. (b) Second approach of GNRs fabrication by BCP lithography. SiARC trenches were used as soft guiding lines for DSA of PS-b-PDMS. Electric contacts were deposited directly on the GNRs array. The corresponding SEM image is showed [53]. (c) Best electric performances of a GNR-FET fabricated via a BCP lithography exhibit a $I_{on}/I_{off} \approx 96$. Transfer curve, I_{SD} as a function of V_G, for FETs based on GNRs and unpatterned bulk graphene sheets measured at $V_{SD} = 1$ V and 20 mV respectively [54]. (d) Scanning tunnelling microscope image (main) and potential chemical structure of GNRs created by a bottom-up synthesis method. Inset: polymeric chain assembly reaction for DBBA molecules. Adapted from [55, 48].

After PDMS oxidation by CF_4 RIE, directional CF_4/O_2-based RIE was performed to transfer the PDMS cylinder patterns into the cross-linked underlayer as well as the underlying graphene to form sub-10 nm GNR. Some steps process are display and detailed in fig. 5.10a.

Son *et al.* described FET characteristics and photoelectric properties of GNR arrays having 9 nm widths which were fabricated using the same BCP mask to pattern graphene [53]. They complemented photolithography to create 1.4 μm-wide and 32 nm-deep line-space SiARC trenches to direct PS-*b*-PDMS self-assembly. They carried out 15 s of CF_4 RIE and annealed at 400 ℃ for 10 min in order to remove the oxidized PDMS and ARC that where still covering the GNR arrays. Back-gated FETs were fabricated from the GNR arrays using conventional photolithography. The three-terminal device consisted of a GNR channel with Ti/Au source and drain contacts, a p^{++}-Si back gate and a thermally grown 300 nm-thick SiO_2 gate dielectric (fig. 3.8b). The electrical measurements were carried out in vacuum to eliminate hole doping effects due to absorption of oxygen and water molecules at the graphene surface. Electric measures showed the strong temperature dependence of the I_{DS}-V_G curves. At RT they mesured a $I_{on}/I_{off} \approx 10$.

Table 3.2.: Electric properties of graphene-nanostructures devices patterned by block copolymer lithography.

Width (nm)	**Carrer mobility (cm^2 Vs^{-1})**	**Bandgap (meV)**	I_{on}/I_{off}	**Dimension (lxw μm^2)**	**Reference**
8	7.3		95	0.1x0.05	[54]
8	287		13	10x5	[52]
9	120		5	2.4x1.4	[53]

Better electrical performances in GNR-FET, fabricated by BCP lithography, were showed recently by the Samsung Research Institute [54]. They used prepatterned Au electrodes as guiding trenches to direct the self-assembly of the PS-*b*-PDMS. Then self-assembled multichannel GNRFETs were fabricated at the wafer scale. (6-inch SiO_2 wafers). They mesured a $I_{on}/I_{off} \approx 96$ at RT (fig. 3.8c). On table 3.2, electrical characteristics of GNRs devices using block copolymer lithography are summarized. GNRs structures are mainly fabricate by cylinder-forming PS-*b*-PDMS of 16kg/mol.

3.3. Summary

Graphene and its related materials have outstanding properties and will undoubtedly find applications in different fields. This chapter gave the reader the main concepts to understand the needs and issues of graphene patterning, i.e., the bandgap opening in graphene by lateral confinement (< 10nm) of the Dirac electrons which generates a transition to semiconductor from its intrinsic semi-metal behavior.

In this context, the high-χ BCP lithography responds to the current demands in nanosciences and materials science for ultra high-resolution patterning. The state-of-the-art about this subject showed some few studies on graphene nanoribons fabrication using PS-*b*-PDMS BCP, with highly promising results in the bandgap opening. From a nanofabrication point of view, there is a growing appeal to develop large-area and CMOS compatible processes that can uniformly pattern sub-10 nm graphene features with controlled orientation, edge structure and passivation.

Next chapters are dedicated to design a clean room compatible procedure generating ~ 10 nm half-pitch graphene features. For this, a cylindrical-forming self-assembled PS-*b*-PDMS thin film is used as lithography mask. Main carbon analysis techniques such as Raman spectroscopy, X-ray photoelectron spectroscopy and the atomic force microscopy were used along this study. A briefly theorical background of these techniques is offered in app. B. The ultimate goal is to fabricate uniform GNRs on large surfaces to ensure the device reproducibility for any applications.

Bibliography

[1] K. S. Novoselov, A. K. Geim, S. V. Morozov, D. Jiang, Y. Zhang, S. V. Dubonos, I. V. Grigorieva, and A. A. Firsov, Science (New York, N.Y.) **306**, 666 (2004).

[2] K. S. Novoselov, A. K. Geim, S. V. Morozov, D. Jiang, M. I. Katsnelson, I. V. Grigorieva, S. V. Dubonos, and A. A. Firsov, Nature **438**, 197 (2005).

[3] A. K. Geim and K. S. Novoselov, Nature materials **6**, 183 (2007).

[4] P. Y. Huang, C. S. Ruiz-Vargas, A. M. van der Zande, W. S. Whitney, M. P. Levendorf, J. W. Kevek, S. Garg, J. S. Alden, C. J. Hustedt, Y. Zhu, J. Park, P. L. McEuen, and D. A. Muller, Nature **469**, 389 (2011).

[5] P. Wallace, Physical Review **71**, 622 (1947).

[6] S. Reich, J. Maultzsch, C. Thomsen, and P. Ordejón, Physical Review B **66**, 035412 (2002).

[7] S. Das Sarma, S. Adam, E. H. Hwang, and E. Rossi, Reviews of Modern Physics **83**, 407 (2011).

[8] A. H. Castro Neto, N. M. R. Peres, K. S. Novoselov, and A. K. Geim, Reviews of Modern Physics **81**, 109 (2009).

[9] X. Wang and Y. Shi, in *Nanofabrication and its Application in Renewable Energy*, 32, edited by G. Zhang and N. Manjooran (The Royal Society of Chemistry, 2014) Chap. 1, pp. 1–30.

[10] M. Wilson, Physics Today **59**, 21 (2006).

[11] C. R. Dean, A. F. Young, I. Meric, C. Lee, L. Wang, S. Sorgenfrei, K. Watanabe, T. Taniguchi, P. Kim, K. L. Shepard, and J. Hone, Nature nanotechnology **5**, 722 (2010).

[12] Y.-M. Lin, C. Dimitrakopoulos, K. A. Jenkins, D. B. Farmer, H.-Y. Chiu, A. Grill, and P. Avouris, Science (New York, N.Y.) **327**, 662 (2010).

[13] F. H. L. Koppens, T. Mueller, P. Avouris, A. C. Ferrari, M. S. Vitiello, and M. Polini, Nature Nanotechnology **9**, 780 (2014).

[14] F. Wang, Y. Zhang, C. Tian, C. Girit, A. Zettl, M. Crommie, and Y. R. Shen, Science (New York, N.Y.) **320**, 206 (2008).

[15] J. M. Dawlaty, S. Shivaraman, J. Strait, P. George, M. Chandrashekhar, F. Rana, M. G. Spencer, D. Veksler, and Y. Chen, Applied Physics Letters **93**, 131905 (2008).

[16] K. S. Novoselov, V. I. Fal'ko, L. Colombo, P. R. Gellert, M. G. Schwab, and K. Kim, Nature **490**, 192 (2012).

[17] K. S. Kim, Y. Zhao, H. Jang, S. Y. Lee, J. M. Kim, K. S. Kim, J.-H. Ahn, P. Kim, J.-Y. 2013, and B. H. Hong, Nature **457**, 706 (2009).

[18] Z. Sun, T. Hasan, F. Torrisi, D. Popa, G. Privitera, F. Wang, F. Bonaccorso, D. M. Basko, and A. C. Ferrari, ACS nano **4**, 803 (2010).

[19] T. Low and P. Avouris, ACS nano **8**, 1086 (2014).

[20] M. Freitag, T. Low, W. Zhu, H. Yan, F. Xia, and P. Avouris, Nature communications **4**, 1951 (2013).

[21] F. Schwierz, Nature nanotechnology **5**, 487 (2010).

[22] X. Wang, X. Li, L. Zhang, Y. Yoon, P. K. Weber, H. Wang, J. Guo, and H. Dai, Science (New York, N.Y.) **324**, 768 (2009).

[23] Y. Zheng, Y. Jiao, L. Ge, M. Jaroniec, and S. Z. Qiao, Angewandte Chemie **125**, 3192 (2013).

[24] S. Zhou, D. Siegel, A. Fedorov, and A. Lanzara, Physical Review Letters **101**, 086402 (2008).

[25] C. Berger, Z. Song, X. Li, X. Wu, N. Brown, C. Naud, D. Mayou, T. Li, J. Hass, A. N. Marchenkov, E. H. Conrad, P. N. First, and W. A. de Heer, Science **312** (2006).

[26] K. Nakada, M. Fujita, G. Dresselhaus, and M. Dresselhaus, Physical Review B **54**, 17954 (1996).

[27] Y.-W. Son, M. L. Cohen, and S. G. Louie, Nature **444**, 347 (2006).

[28] V. Barone, O. Hod, and G. E. Scuseria, Nano letters **6**, 2748 (2006).

[29] C. Nanmeni Bondja, Z. Geng, R. Granzner, J. Pezoldt, and F. Schwierz, Electronics **5**, 3 (2016).

[30] Y.-W. Son, M. L. Cohen, and S. G. Louie, Physical Review Letters **97**, 216803 (2006).

[31] L. Yang, C. H. Park, Y. W. Son, M. L. Cohen, and S. G. Louie, Physical Review Letters **99**, 6 (2007), 0706.1589 .

[32] M. Evaldsson, I. V. Zozoulenko, H. Xu, and T. Heinzel, Physical Review B **78**, 161407 (2008).

[33] Q. Yan, B. Huang, J. Yu, F. Zheng, J. Zang, J. Wu, B.-L. Gu, F. Liu, and W. Duan, Nano letters **7**, 1469 (2007).

[34] C.-H. Park, L. Yang, Y.-W. Son, M. L. Cohen, and S. G. Louie, Nature Physics **4**, 213 (2008).

[35] F. Schwierz, *Emerging Nanoelectronic Devices*, edited by A. Chen, J. Hutchby, V. Zhirnov, and G. Bourianoff (John Wiley & Sons Ltd, Chichester, United Kingdom, 2014) pp. 298–314.

[36] C. Stampfer, J. Güttinger, S. Hellmüller, F. Molitor, K. Ensslin, and T. Ihn, Physical Review Letters **102**, 056403 (2009).

[37] M. Han, B. Özyilmaz, Y. Zhang, and P. Kim, Physical Review Letters **98**, 206805 (2007).

[38] S. S. Datta, D. R. Strachan, S. M. Khamis, and A. T. C. Johnson, Nano Letters **8**, 1912 (2008), arXiv:0806.3965 .

[39] X. Wang and H. Dai, Nature chemistry **2**, 661 (2010).

[40] I. Martin-Fernandez, D. Wang, and Y. Zhang, Nano Letters **12**, 6175 (2012).

[41] J. Baringhaus, M. Ruan, F. Edler, A. Tejeda, M. Sicot, A. Taleb-Ibrahimi, A.-P. Li, Z. Jiang, E. H. Conrad, C. Berger, C. Tegenkamp, and W. A. de Heer, Nature **506**, 349 (2014).

[42] Y.-C. Chen, T. Cao, C. Chen, Z. Pedramrazi, D. Haberer, D. G. de Oteyza, F. R. Fischer, S. G. Louie, and M. F. Crommie, Nature nanotechnology **10**, 156 (2015).

[43] R. M. Jacobberger, B. Kiraly, M. Fortin-Deschenes, P. L. Levesque, K. M. McElhinny, G. J. Brady, R. Rojas Delgado, S. Singha Roy, A. Mannix, M. G. Lagally, P. G. Evans, P. Desjardins, R. Martel, M. C. Hersam, N. P. Guisinger, and M. S. Arnold, Nature communications **6**, 8006 (2015).

[44] W. S. Hwang, K. Tahy, X. Li, H. G. Xing, A. C. Seabaugh, C. Y. Sung, and D. Jena, Applied Physics Letters **100**, 203107 (2012).

[45] G. Z. Magda, X. Jin, I. Hagymasi, P. Vancso, Z. Osvath, P. Nemes-Incze, C. Hwang, L. P. Biro, and L. Tapaszto, Nature **514**, 608 (2014), arXiv:1411.1196 .

[46] N. Krane, Physics of Nanoscale Carbon **4**, 1 (2014).

[47] L. Jiang and Z. Fan, Nanoscale **6**, 1922 (2014).

[48] J. Cai, P. Ruffieux, R. Jaafar, M. Bieri, T. Braun, S. Blankenburg, M. Muoth, A. P. Seitsonen, M. Saleh, X. Feng, *et al.*, Nature **466**, 470 (2010).

[49] J. P. Llinas, A. Fairbrother, G. Borin Barin, W. Shi, K. Lee, S. Wu, B. Yong Choi, R. Braganza, J. Lear, N. Kau, W. Choi, C. Chen, Z. Pedramrazi, T. Dumslaff, A. Narita, X. Feng, K. Müllen, F. Fischer, A. Zettl, P. Ruffieux, E. Yablonovitch, M. Crommie, R. Fasel, and J. Bokor, Nature Communications **8**, 633 (2017).

[50] M. Min, S. Seo, Y. Yoon, K. Cho, S. M. Lee, T. Lee, and H. Lee, Nanoscale **8**, 17022 (2016).

[51] L. Jiao, L. Xie, and H. Dai, Nano Research **5**, 292 (2012).

[52] X. Liang and S. Wi, ACS nano **6**, 9700 (2012).

[53] J. G. Son, M. Son, K.-J. Moon, B. H. Lee, J.-M. Myoung, M. S. Strano, M.-H. Ham, and C. A. Ross, Advanced Materials **25**, 4723 (2013).

[54] S.-J. Jeong, S. Jo, J. Lee, K. Yang, H. Lee, C.-S. Lee, H. Park, and S. Park, Nano Letters , acs.nanolett.6b01542 (2016).

[55] X. Wang, Nature nanotechnology **9**, 875 (2014).

4. Self-assembly of PS-PDMS on graphene

4.1. Introduction

As block copolymer lithography is as an efficient technique for high-resolution patterning, BCP lithography tries to fulfill and exploit the current demand in the applications needing ultra high-resolution patterning. The low-χ PS-*b*-PMMA BCP was already used for graphene patterning [1, 2, 3]. These investigations were limited to the vertical cylindrical morphology to produce graphene nanomesh structures [4]. PS-*b*-PMMA was limited in resolution ($\sim$ 34 nm of period) by the reasons detailed in chapter 1. Greater advances in the high$-\chi$ PS-*b*-PDMS self-assembly has led the research to study graphene patterning by producing graphene nanoribbons [5, 6].

Very few studies have been carried out, focusing on the self-assembly of PS-*b*-PDMS on graphene [7]. It includes the searching of the equilibrium conditions at which the desired morphology can be obtained, dealing with graphene surface energy and the PS-*b*-PDMS own challenges as orientation control and the large surface energy mismatch between the blocks. Otherwise, the large-area nanopatterning of graphene raises itself an arduous technological issue. For all these reasons, an effective nanofabrication process integrating PS-*b*-PDMS BCP lithography and graphene have to be proposed for semiconducting GNRs study and their eventual device application, assuring a high quality during the fabrication process.

The scope of the work presented in this chapter, is to study the self-assembly of PS-*b*-PDMS in order to obtain a cylindrical hard mask of oxidized-PDMS. This is in the context to develop a feasible procedure of fabrication of a lithographic mask by the self-assembly of BCPs. It is of interest that this mask would be capable to generate sub-10 nm width channels. Compared to chapter 2, A smaller molecular weight PS-*b*-PDMS is used to create a self-assembled silica mask of $\sim$ 10 nm half-pitch size. Of prime importance was the study of the PS-*b*-PDMS-graphene interactions to understand

the best compromise, the eventual need to interpose underlayers to achieve flawless self-assembly of BCP.

4.2. Experimental procedure

4.2.1. Materials

Graphene

Monolayer graphene on 300-nm SiO_2 4-in wafer was obtained from Graphenea. According to their specifications, this graphene is produced by CVD and transferred by a wet transfer process. The graphene wafer was carefully cleaved to 1x1 cm^2 SiO_2 samples and used as received.

Block copolymer

Cylinder-forming PS-*b*-PDMS BCP (M_w=11-5 kg/mol, PDI=1.08, f_{PDMS}=33%) was purchased from Polymer Source Inc. (Canada) and used as received. Microelectronic-grade PGMEA was used as the solution solvent for BCP solutions. Solutions of 1 wt % were prepared and spin-coated at 1800 rpm on graphene substrate. BCP thicknesses were measured by ellipsometry on 300-nm thick SiO_2 layer on Si substrate and were estimated at approximately 20±2 nm, which corresponds to one BCP natural period. A hot plate was used for heat treatment at different temperatures and time to trigger the cylinder-forming self-assembly of the BCP.

Plasma Etching

Experiments were performed in an industrial 300 mm diameter wafer AdvantEdge ICP (inductively coupled plasma) etch tool from Applied Materials. Samples were first etched by CF_4 plasma (etching time = 6 s, gas flow rate = 20 sccm, working pressure = 4 mTorr, plasma source power = 500 W and plasma bias power = 5 W) to remove the top-segregated Polydimethylsiloxane (PDMS) layer. The PS block was than etched by O_2 plasma (etching time = 6 s, gas flow rate = 90 sccm respectively, working pressure

= 5 mTorr, plasma source power = 400 W, plasma bias power = 5).

4.2.2. Characterizations

Observations

Self-assembled morphologies were investigated by SEM, STEM or even TEM. SEM images were performed at 30 kV with a field emission electron source (Hitachi S-5000).

Sample preparations and STEM observations were carried out in a Helios 450S-FEI equipment. An 1 μm thick layer of Pt was deposited on the BCP thin film inside the STEM using a high energy ion beam. After a careful alignment perpendicular to the patterns, a small sample was extracted and thinned to approximately 100 nm. An in-situ observation was finally carried out using the STEM detector.

Raman spectroscopy

Raman spectra were obtained by a Raman microscope system from Horiba Scientific facilitated by the LMGP lab at PHELMA, Grenoble. Measurements were performed using a 100x objective with a blue laser having an excitation wavelength of 488 nm. The laser power was 4 mW and the acquisition time was of the order of 2 seconds to avoid sample degradation. Lateral focus of the laser was a few µm. We concentrate on the G, D and 2D bands of the spectrum, which are expected to appear at 1585 cm^{-1}, 1350 cm^{-1} and 2700 cm^{-1}, respectively.

Contact angle measurement

Static contact angles were measured by the drop shape analyzer DSA100 from Krüss. All measurements were performed at room temperature by depositing a liquid droplet with volume 7 μL on the surface. Liquid dispense rate and volume are controlled with the help of the the ADVANCE software from Krüss. The contact angle was measured based on the image capture by a CDD camera using the same software. Surface free energy calculations were performed using the OWRK method, using the mean disperse and the polar part of the surface tension with water, diiodo-methane and ethylene glycol

Explanation of the OWRK calculation method is detailed in [8, 9].

4.2.3. Methods

Three approaches were tested in order to obtain a self-assembled hard mask for graphene patterning using the PS-*b*-PDMS 16kg/mol. On one side, two paths were studied simultaneously: the self-assembly of the PS-*b*-PDMS on graphene and the same using an underlayer in the case of major issues of self-assembly directly on graphene. On the other side, a third approach aimed the directed self-assembly of the PS-*b*-PDMS by graphoepitaxy. Table 4.1 recaps the experimental design used in the search for a PS-PDMS lithographic hard mask for sub-10nm graphene patterning. The table details the specific purpose of every approach and the difficulties which must be addressed. Section 4.3 expands the experimental procedures and results of the three approaches.

In all cases, a long range order self-assembly ($\xi \approx 100$ nm) is required for further GNRs studies and device fabrication. And secondly, the self-assembly activation must be carried out by thermal means for possible integration in the semiconductor industry. Indeed, most studies using PS-PDMS have used the less suitable solvent vapor annealing for industry (1.3.2).

4.3. Results

4.3.1. Middle layer approach

Conventionally, to promote spontaneous self-assembly and avoid any PDMS layer at the substrate–BCP interface, an interfacial layer called brush is used. For instance, hydroxyl end-group polystyrene (PS–OH) homopolymer can be grafted onto the surface, usually Si. Excellent results in self-assembling the PS-*b*-PDMS 16kg/mol on Si were obtained previously in our research group by optimizing PS–OH grafting on Si [10]. The terminated groups attach to the surface and then the surface is chemically modified. This chemical modification cannot occur in graphene by conventional thermal means as it is a sp^2 carbon network and then chemically inert [11, 12]. This fact was verified by ellipsometry measurements, where no PS-brush grafting on graphene occurred using the usual procedure on Si adopted in chapter 2.

Table 4.1.: Experiment design followed for self-assembly of a PS-PDMS mask .

Approach	**Section**	**Difficulty**	**Interest**
Middle layer	4.3.1	Choice of an undercoat layer for PS-*b*-PDMS transfer and graphene patterning	• Protection of graphene quality • Controlled underlayer transfer scheme
Direct spin-coating	4.3.2	Control of graphene surface energy and its impact on the BCP final morphology	• Direct spread of the PS-PDMS thin film on graphene • Technologically lightened procedure
Graphoepitaxy	4.3.3	Development of a specific soft graphoepitaxy on graphene with removable trenches	• Fabrication of self-aligned channels of GNRs • Conceivable for device development

The absence of –OH radicals on the inert graphene monolayer makes difficult the grafting of brush layers to facilitate self-assembly of PS-*b*-PDMS. The use of brush layers to change the graphene surface energy was proposed by Park *et al.*, without a pertinent study on the graphene properties impact [13]. Moreover, fragile polycrystalline CVD graphene could be damaged during the procedure of grafting. That is the main reason why a middle layer approach was developed in parallel with direct spin-coating of the PS-PDMS on graphene.

Indeed, this path could be an effective way to protect graphene from damaging and chemical contamination during the patterning procedure. They play the role of sacrificial layers, that could be removed selectively after graphene patterning. Nonetheless, an effective middle layer have to satisfy some requirements :

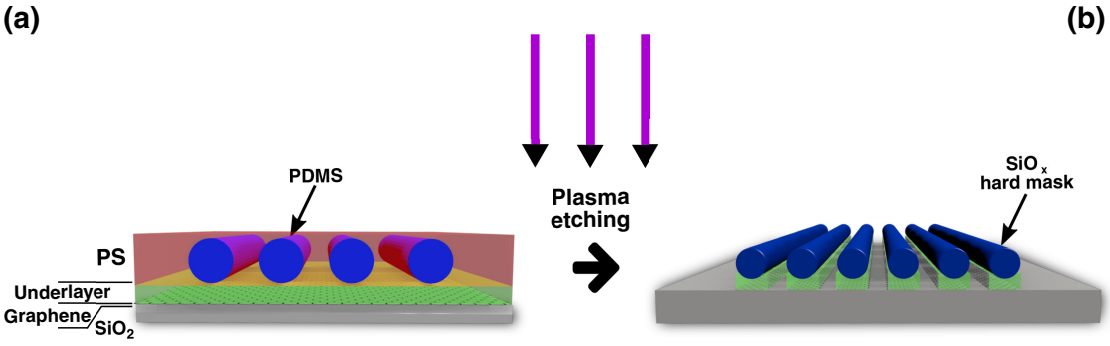

Figure 4.1.: Schematic representation of the graphene patterning by the middle layer approach. (a) Layer stack used (b) After the corresponding plasma etching steps, the PS-PDMS is transformed into a SiO_x hard mask which at the same time is transfer in graphene.

- Create at least van der Waals bonds with graphene to assure adhesion
- Have chemical affinity with PS like PS-brush, to avoid a PDMS wetting layer
- Be efficient in high aspect ratio pattern transfer

Schematic representation of the ideal middle layer is showed in Fig. 4.1a. At the end of the plasma etching step, the PS-PDMS template has been transformed in a SiO_x hardmask and then transfered into the underlayer and finally graphene (Fig. 4.1b). This chapter focuses on the correct self-assembly of the PS-PDMS on the different underlayers studied, achieving the desired stable morphology with its corresponding dimensional characteristics. A proper transfer by plasma etching will be the object of chapter 5

PMMA is commonly used as a transfer carrier polymer to the target substrate (SiO_2 in this case) from Cu growth substrate [14, 15]. PMMA coating forms covalent bonds with graphene [16]. It can be easily spin-coated on any substrate and is fairly available in the semiconductor manufacturing environments. Then, a thin PMMA layer ($\sim$ 20 nm) was used on G as middle layer. The BCP thin film was spread out on PMMA and the self-assembly at 150°C evaluated by SEM. Fig. 4.2a shows the self-assembled PS-*b*-PDMS on PMMA. Cross-linked PMMA was tested as well, however unsatisfactory results were observed with a low ξ value (fig. 4.2b). Cross-linked PMMA was annealed at 220 °C to start the chemical reactions and irreversibly harden the PMMA. After heating, uncross-linked chains are removed with solvent. The resulting cross-linked PMMA layer

is likely highly rugged influencing negatively the self-assembly process.

Another middle layer tested was the SOC, a carbon-based underlayer. It is used as an intermediate hardmask to transfer patterns into silicon by plasma etching [17]. Generally, by using a SOC hardmask stack, a considerable increase in achievable aspect ratios is possible [18]. SOC has strong chemical similarities to PS and shows thus a favored wetting of this block, so SOC acts as a PS brush layer. Result is shown in fig. 4.2c.

In the same way, an inorganic middle layer was tested . Alumina is a high-κ dielectric material, commonly used in microelectronics as an insulator. The deposition of high-κ dielectrics is usually achieved using Atomic Layer Deposition (ALD), which requires an chemically active surface with –OH functional groups [19]. As it was the case with PS-brush, the inert surface of graphene make impossible any Al_2O_3 growth on G. Moreover functionalization of graphene surface for ALD either introduces undesired impurities or breaks the chemical bonds in its lattice, leading to a carrier mobility degradation [20].

Physical Vapor Deposition (PVD) such as evaporation is a technique used for dielectric deposition without the need of surface activation. The technique consists in depositing a few-nanometer-thick layer of Al ($\sim$ 3 nm). The deposited Al layer is oxidized spontaneously by the air during several hours, as it can oxidize the first nanometers. The rest of the alumina layer is concluded by ALD. The alumina layer was doubled by depositing 3 nm of Al_2O_3. Subsequently alumina was functionalized with PS brush and the BCP self-assembled on it using the experimental parameters detailed in sec. 4.2. Here a combination of cylinders and perforated lamellae is observed (fig. 4.2d).

Unsatisfactory results of self-assembly at 150 ℃ during 15 min were observed in all the middle layers tested. For a better legibility of pattern ordering and grain sizes, orientation mappings are displayed as inset in each SEM images and the correlation length values displayed in 4.2f. The procedure of image treatment is detailed in appendix A. The four values of correlation lengths were just few times the L_0 which is considered a poor self-assembly ($\xi \ncong 100$nm). For comparison, the PS-*b*-PDMS directly spin-coated on graphene is showed in fig 4.2e without improvement in the self-assembly.

The BCP and the underlayer interface were studied by STEM. The BCP-PMMA interface is showed in fig. 4.3b. A PDMS layer at the interface is observed which is annoying for pattern transfer. In an ideal BCP template, the PS matrix should directly wet the underlayer, like visualized in the fig. 4.1. The undesirable situation presented

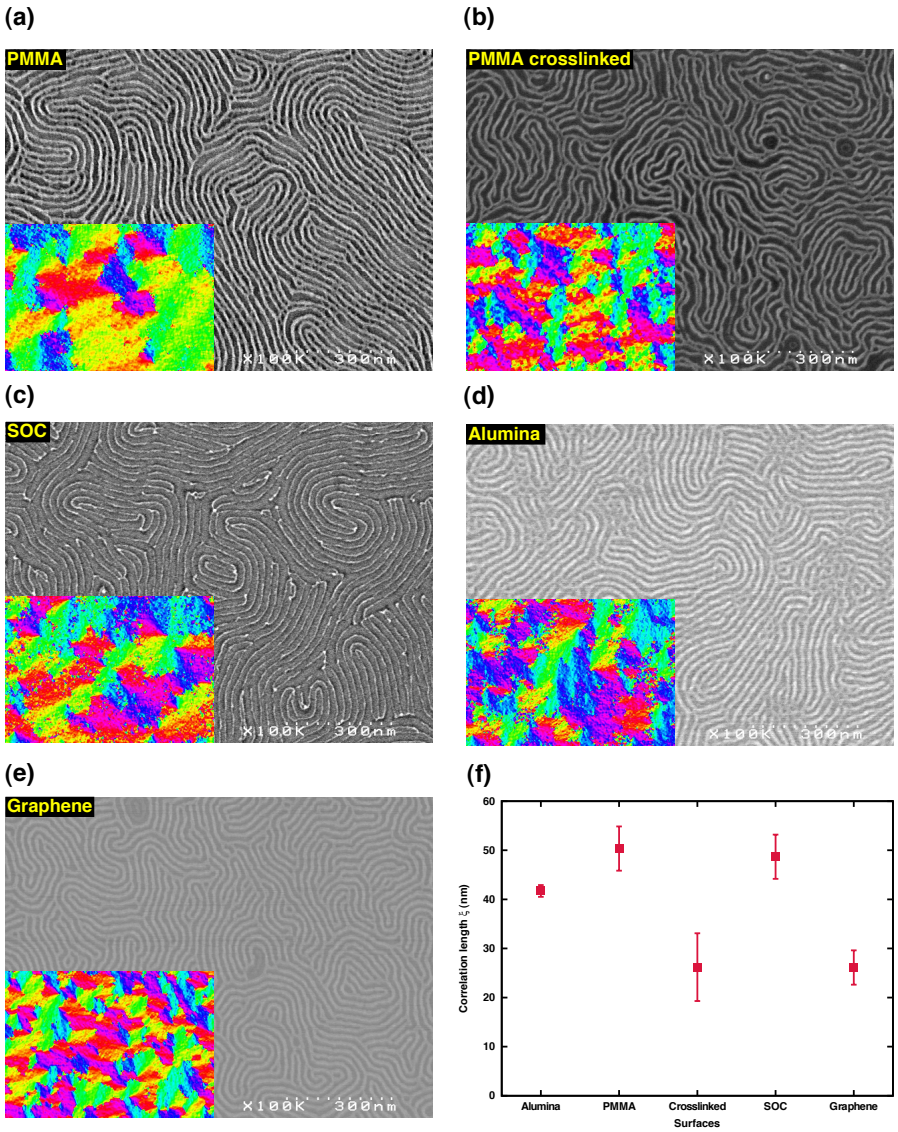

Figure 4.2.: Self-assembly of PS-PDMS during 15 min at 150 °C on different middle layer surfaces: (a) PMMA, (b) crosslinked PMMA, (c) SOC, (d) Alumina and (e) Graphene. Inset images show the orientation map of each image. (f) Correlation lenghts measured from the orientation map images. The calculation method is detailed in the appendix A.

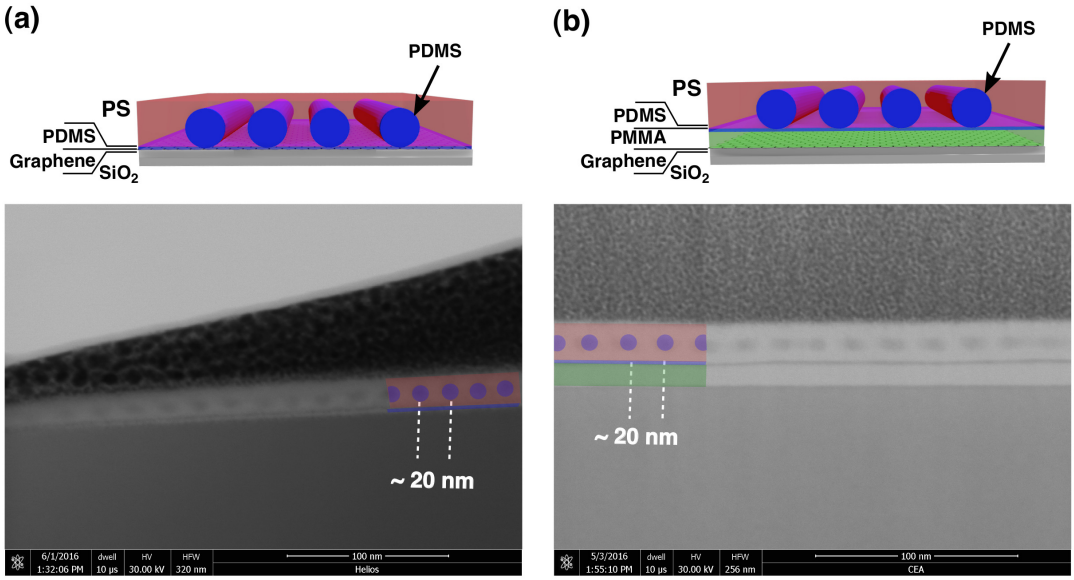

Figure 4.3.: STEM cross-section images of (a) PS-PDMS on graphene and (b) PS-PDMS on PMMA/graphene. The above diagrams represent the expected thin films stack. For comparison and help the reader, the STEM images were partially colored with the observed interfaces. In both cases, the natural period correspond to $\sim$ 20 nm, as expected.

here is schematized in fig.4.3b. As a comparison, in fig. 4.3a, the BCP-graphene interface as observed by STEM is shown too, where is also observed the obstructive PDMS layer at the dark interface. As PMMA is a widely used polymer support for CVD graphene transfer, it is expected that PMMA residues on graphene remain after PMMA removal. Indeed, graphene surface used is rather hydrophilic, in opposition to exfoliated graphene [21]. The average contact angle was measured: the water droplet contact angle on graphene was 62° near that of PMMA: 70° [22]. Consequently, it is expected than the low energy surface PDMS block wets the surface at the BCP-substrate interface, rather than the PS bloc.

4.3.2. Direct spin-coating approach

Better results were obtained with a direct BCP self-assembly on graphene. From the three deepen approaches, it is the simplest path technologically speaking. A direct spin-coating avoids the use of transfer layers that makes the pattern procedure heavier. Moreover it needs to overcome the delicate procedure of BCP mask and underlayer

stripping without any GNR damaging. Once the graphene is nanostructurated, reactive edges play an important role of its properties in terms of stability [23, 24, 25].

Table 4.2.: Free energy values of different surfaces by the contact angle measurements.

Material	**Surface energy (mJ/m^2)**	**Dispersive (mJ/m^2)**	**Polar (mJ/m^2)**
PDMS[a]	19.8	19.0	0.8
PMMA	40.0 ± 8	37.5 ± 6	2.5 ± 2
PS[a]	40.7	34.5	6.1
LOR	44.2 ± 4	44.2 ± 4	0.0 ± 0.1
PMMA crosslinked	45.0 ± 6	40.7 ± 4	4.3 ± 2
SOC	45.0 ± 3	44.9 ± 2.87	0.1 ± 0.2

[a] Theoretical values from [26].

The surface state of graphene is determined by its chemical structure, homogeneity and crystallinity [27]. Modification and control of the surface energy allow a precise control of wetting issues, BCP orientation and long-range order. Kim *et al.* observed a graphene surface energy modification via a thermal treatment, for potential use of block copolymer lithography [28]. Indeed, by thermal annealing treatment at 170 °C an inversion of the surface character from hydrophilic to hydrophobic is achieved, which is characteristic of graphene [29]. We verified this by the contact angle measurements with a water droplet, where the average contact angle changed from 68.1°before thermal treatment (Fig. 4.4b) to 94.8° (Fig. 4.4a). The thermal treatment is expected to partially remove water and some of the polar functional groups situated at the extreme surface which favor water wetting [28].

Raman measurements were performed on pristine graphene after thermal annealing, for checking its crystalline structure state. The Raman fingerprint of graphene is characterized by the D (1350 cm^{-1}), G (1580 cm^{-1}) and 2D (2690 cm^{-1}) peaks [30]. The main two peaks G and 2D are caused by the in-plane vibrational modes under laser excitation, meanwhile the first order D peak appears because of crystal dissymmetries, i.e. defects. (for more theoretical details, refer to appendix B). Fig. 4.4c does not show any significant increase of the D peak intensity, nevertheless a blue shift of the G and 2D peaks was observed. As defects were not introduced to graphene under thermal annealing, blue shifts are attributed to a compressive stress on graphene induced by the thermal annealing [31].

Direct spin-coating of the PS-*b*-PDMS was then tested on the annealed graphene.

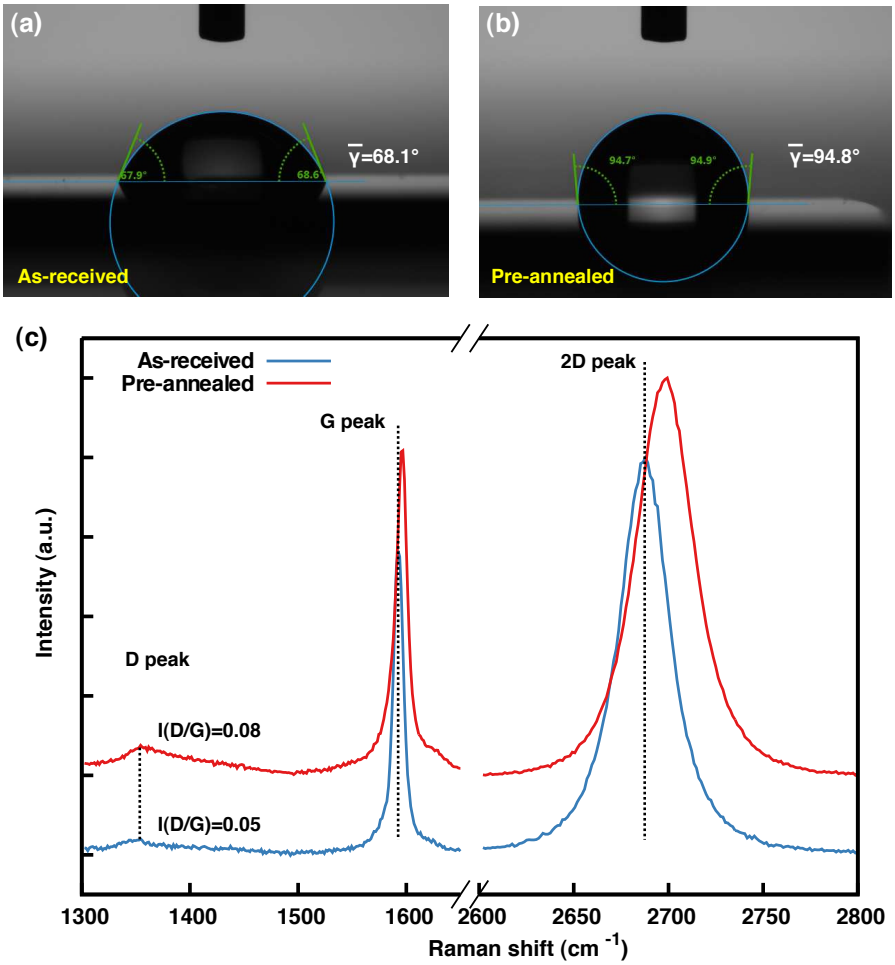

Figure 4.4.: Thermal pre-annealing of graphene to favor self-assembly of PS-PDMS. Contact angle measurements were performed in the (a) as-received graphene surface and (b) after thermal annealing at 170 °C. (c) a Raman spectra was obtained in both cases. For comparison, the spectras were normalized with respect to the G peak.

Results of the self-assembled BCP are showed in Fig 4.5a. A light improvement in the self-assembly BCP was observed and measured by the corresponding ξ value, in comparison that obtained in Fig. 4.2e, when the graphene was not pre-annealed. Even the significant changed in the graphene wettability, PDMS continues wetting the graphene at the BCP-graphene interface, which is annoying for the lithography application (Fig. 4.5b).

The interfacial tension γ of graphene and water in Fig. 4.4 can be given by the Young`s equation as follows

$$\gamma_{G-w} = \gamma_G - \gamma_w \cos\theta \tag{4.1}$$

where γ_G, γ_w and $\gamma_G - w$ represent the graphene surface free energy, water surface free energy, and graphene-water interfacial energy, respectively. θ is the contact angle between the graphene and water. Using the Good and Girifalco model estimation of the interfacial energy [32],

$$\gamma_{G-w} = \gamma_G - \gamma_w - 2\Phi(\gamma_G\gamma_w)^{1/2}, \Phi = \frac{4(V_G V_w)^{1/3}}{(V_G^{1/3} + V_w^{1/3})^2} \tag{4.2}$$

the interfacial energy of graphene could be estimated (4.2 in 4.1) as

$$\gamma_G \approx \gamma_w(\frac{(1+\cos\theta)^2}{4\Phi^2}) \tag{4.3}$$

On the hand, the work of adhesion W between the graphene surface and a polymer is defined as

$$W_{G-P} = \gamma_P(1+\cos\theta) \tag{4.4}$$

Using the γ_G calculated with eq. 4.3, it is possible to estimate the expected contact angle of a polymer, PS or PDMS, on graphene. According to the experimental θ values and eq. 4.4, the work of adhesion between graphene and PS or PDMS were calculated and displayed in Table 4.3. The experimental values at RT of surface tension for water,

PS and PDMS are $\gamma_w = 72.75$ mJ/m^2, $\gamma_{PS} = 40.7$ mJ/m^2 and $\gamma_{PDMS} = 19.8$ mJ/m^2 [33, 34, 35].

Table 4.3.: Work of adhesion between graphene-polymer interfaces.

Polymer	$\mathbf{W_{G\text{-}P}}$ **(mJ/m^2)**		
	$\theta = 68.1°$	$\theta = 94.8°$	$\theta = 120°$
PS	61.8	41.2	14.6
PDMS	44.8	29.9	16.3

The work of adhesion values expose an important information about the preference wettability of the blocks as a function of the wetting angle. In the two contact angles θ measured (fig. 4.4a-b), a lower work of adhesion was calculated for the PDMS block, then the PDMS wetting correspond to the minimal energetic configuration and it is coherent with that observed in fig. 4.3a and 4.5b. It is expected to switch the preference for wetting graphene for higher values of θ. Indeed the table 4.3 shows the hypothetical situation $\theta = 120$ °, where the PS wettability tends to be energetically more favorable. As the literature predicts a high hydrophobicity for exfoliated graphene, high θ values are expected by thermal or chemical treatments [36, 21].

These results further supported the above discussion on wettability of solid materials and the work of adhesion for the solid-liquid interface. Temperature is limited at 300 °C in G, to avoid any interaction with oxygen and structural changes, beyond must be annealed in vacuum.

Based on the above discussion on wettability of graphene and the work of adhesion for the graphene-polymers, PS-PDMS was thermal annealed directly on graphene at 280 °C. Thermal annealing time was reduced to 3 minutes to avoid dewetting of the BCP film, degradation or undesirable BCP-graphene interaction at the surface. The results of the self-assembled thin film are showed in Fig. 4.5c. Correlation length value calculations demonstrated the improvement in self-assembly ($\xi = 330$ nm). It corresponds to ten times the correlation length obtained in fig. 4.5a. Fig. 4.5d shows the TEM cross section image of the self-assembled PS-PDMS 16kg/mol on graphene. It is observed that the PS matrix directly wets graphene, which supports the calculations of work of adhesion. Higher temperatures may generate a local change of free energy at the BCP-graphene interface, allowing the wetting of the PS matrix. Moreover, by temperature elevation, the activation energy ΔE_a from eq. 1.16 is reduced and the defect elimination with [37]. It explains the increase the self-assembled grains and kinetics of the stable

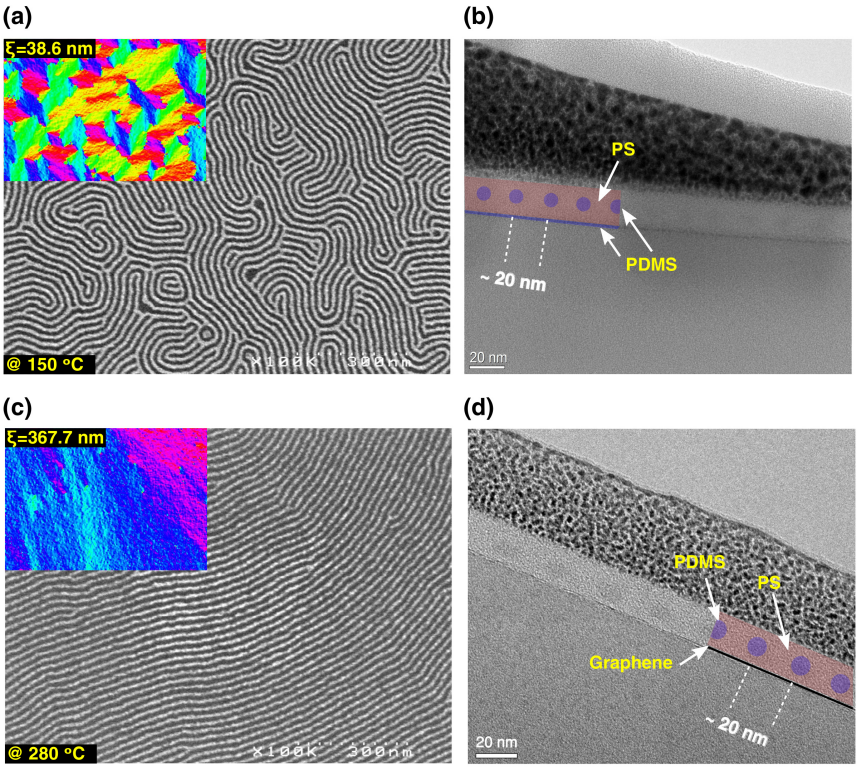

Figure 4.5.: Direct self-assembly of PS-PDMS 16kg/mol on graphene at different thermal annealing temperatures. Top-view SEM images for (a) 150 °C and (c) 280 °C. Insets: corresponding orientation map images. Cross-section TEM images for (b) 150 °C and (d) 280 °C. For comparison and help the reader, the TEM images were partially colored with the observed interfaces. In both cases, the natural period correspond to $\sim$ 20 nm, as expected.

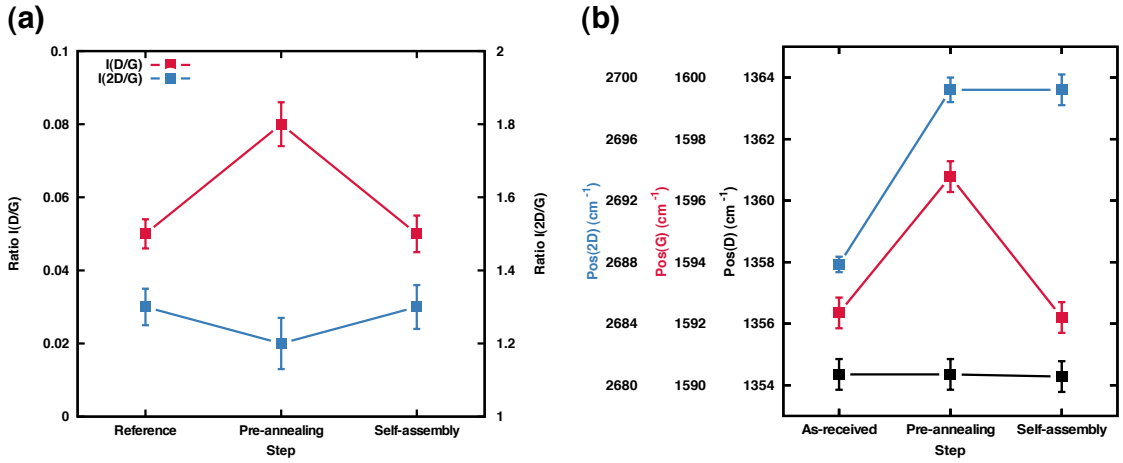

Figure 4.6.: Control of the characteristic features of the Raman spectra for the graphene substrate after every step: as-received, pre-annealing and self-assembly of PS-PDMS. (a) Evolution of the intensity ratios I(D/G) and I(2D/G). (b) Position values of the D, G and 2D peaks.

cylindrical morphology.

Raman measurements were performed after self-assembly for quality control. The main characteristic features of the Raman spectra are showed at every step. For comparison, the data from fig. 4.4c was included. Intensity ratios displayed in fig. 4.6a do not show a variation of the ratios with respect to the reference after self-assembly. Similarly the peak positions (fig. 4.6b) do not show variations, except the blue shift in the 2D induced by the pre-annealing, which is kept after the self-assembly process. So the thermal annealing steps involved in the self-assembly process on graphene do not induce structural modifications in graphene, but a compressive stress on the graphene substrate. As excellent results on self-assembly had been obtained by direct spin-coating at 280°C, the middle layer approach was set aside to deepen the directed self-assembly of PS-*b*-PDMS and transfer by plasma etching.

4.3.3. Soft graphoepitaxy approach

Soft graphoepitaxy has been introduced as an alternative approach to direct the self-assembly and being able to remove the prepatterned trenches after BCP aligment [38, 39]. Standard soft graphoepitaxy uses an organic negative photoresist, usually used for deep ultraviolet photolithography, to create the topography necessary to direct the BCP self-

assembly. Therefore, patterned substrates can be generalized on any type and size of surface and is highly compatible with conventional device fabrication process.

In the objective to develop a directional array of GNRs, graphoepitaxy is the more adequate way to direct the self-assembly of PS-*b*-PDMS chains and generate a straight-line mask. Chemoepitaxy is not adapted to be used on graphene since any chemical modification could modify its electrical properties. Then, intermediate layers should be used here in this case. For further overlay processes, in particular device fabrication, it was required to develop an adapted soft graphoepitaxy on graphene for two main reasons. First, usual Si trenches are made by the expensive 193nm photolithography patterning, requiring wafer scale surfaces. Conventional surfaces in graphene and BCP research are of the order of ~ 1 cm^2. Second, any trace of the topographic pattern that directs self-assembly can be completely eliminated during the plasma etching step, while removing the PS matrix with O_2 plasmas.

Chemical solubility of AZ1512 photoresist in PGMEA, motivated to look for another insoluble resist in PGMEA. LOR is a metal lift-off resist used beneath the photoresist in a bilayer stack to extend the limits of the the lift-off processing. Some resist attributes are its solubility in TMAH or KOH based developers, high thermal stability and of course insolubility in PGMEA [40]. It allows to fabricate well-defined carbon-based topography, unaffected by the solvent of the BCPs when they are spread out on the surface. Material selection is crucial as the height of the trenches is critical (height ~ 30 nm).

The overall process of soft graphoepitaxy is schematized in Fig. 4.7a. In a first part LOR resist was spread out directly on graphene at 3000 rpm to create a $\sim$ 27 nm thickness (fig. 4.7a-2). The LOR was previously diluted in thinner solvent to make a 1% LOR solution. LOR thickness was verified by ellipsometry and is supposed to be the height of the trenches. This height is chosen to be slightly higher than the natural period of the BCPs as an important effect of the trench height on the directed self-assembly was already reported [41]. LOR was thermally annealed on a hot plate for 10 minutes at 190 °C.

A positive tone photoresist AZ1512 was uniformly spin-coated directly on LOR and topographically patterned by conventional photolithography (I-line source, wavelength 365 nm, 4 mW/cm^2, fig. 4.7a-3). The exposition time was determined to 4 seconds. Then, it was developed on a 2:1 solution of M823 developer MIF for 14 s. It dissolved the exposed areas to UV of AZ1512 and the underlying resist LOR (fig. 4.7a-4). Finally the

AZ1512 was removed with acetone, leaving the LOR trenches on graphene (fig. 4.7a-5), the LOR trenches on graphene making 1 μm width as expected (fig. 4.7a-5). By optical microscopy it is possible to observe the G grains and multilayers from the CVD growth (fig. 4.7b).

Of special difficulty was to determine a good compromise between LOR hardening and AZ1512 development. The solubility of LOR in the developer depends directly on the hardening made by the thermal annealing (time and temperature). LOR must be hard enough to have an approximative development rate similar than that of the AZ1512 after exposure. So this is added to the complicated task of the development itself by finding the optimal parameters, M823 concentration and time. Fig. 4.7c-d shows SEM images of LOR trenches at the end of the process. Notwithstanding it is noticed that many resist residues stays at the bottom of the trench (Fig. 4.7c) and a high line roughness (Fig. 4.7d) is observed. This may happen from the fact of dealing with the resolution limits of the contact photolithography ($\sim$ 1µm) and resist thickness ($\sim$ 30nm), where the M823 and acetone could "bite" at the trenches borders.

A thin film of PS-*b*-PDMS BCP was spin-coated on the prepatterned LOR trenches on graphene at 3000 rpm (Fig. 4.8a-2). The self-assembly procedures developed in sec. 4.3.2 were tested, then the BCP thin films were thermal annealed at 150 °C and 280 °C (Fig. 4.8a-3).

For PS-*b*-PDMS observation, the well known two-step plasma etching is implemented: a CF_4 followed by an O_2 plasma etching step to remove the PDMS top layer and the PS matrix respectively. The O_2 plasma etches at the same time the uncovered zones of graphene and the LOR trenches. Then the oxidized PDMS cylindrical mask is revealed (Fig. 4.8a-4).

Unfortunately, extremely disordered BCPs confined between the 1µm-spaced trenches are observed at 150 °C (Fig. 4.8b). These bad results of directed self-assembly of PS-*b*-PDMS are definitely induced by the strong line roughness of the prepatterned LOR topography and by the too large multiplication factor. As discussed before, lateral confinement leads the self-assembly of the polymer microdomains, so the quality of the alignment is closely related to the wall roughness. Moreover, from SEM images it is observed that self-assembled cylinders split from the edges, likely due to a LOR wetting by the PDMS block.

Better results of self-assembly were expected when annealing at 280 °C. As observed in

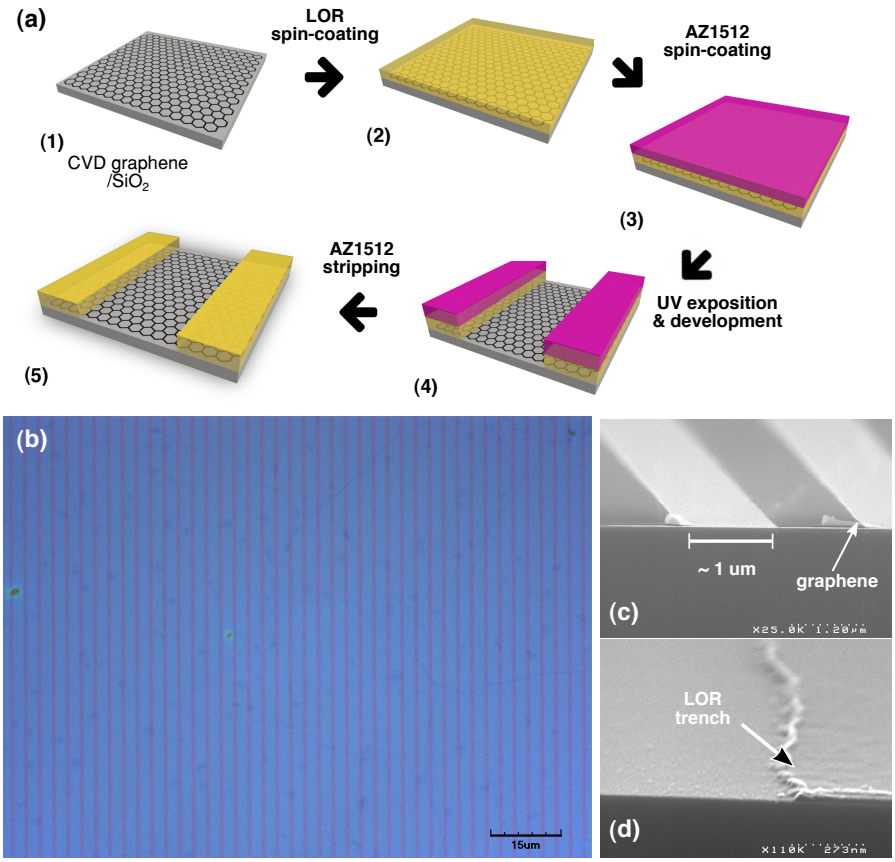

Figure 4.7.: (a) General procedure for soft graphoepitaxy on graphene: (1) graphene on 300 nm SiO_2 substrate, spin-coating and annealing of (2) LOR and (3) AZ1512 resists, (4) UV exposition and development and (5) AZ1512 removing with acetone; (b) Optical microscope image of the LOR patters on graphene. Multilayers graphene and grain wrinkles are observed below the patterns; cross-section SEM images of the (c) LOR trenches on graphene with $\sim$ 1μm width and $\sim$ 30nm height; (d) high roughness of the LOR trenches.

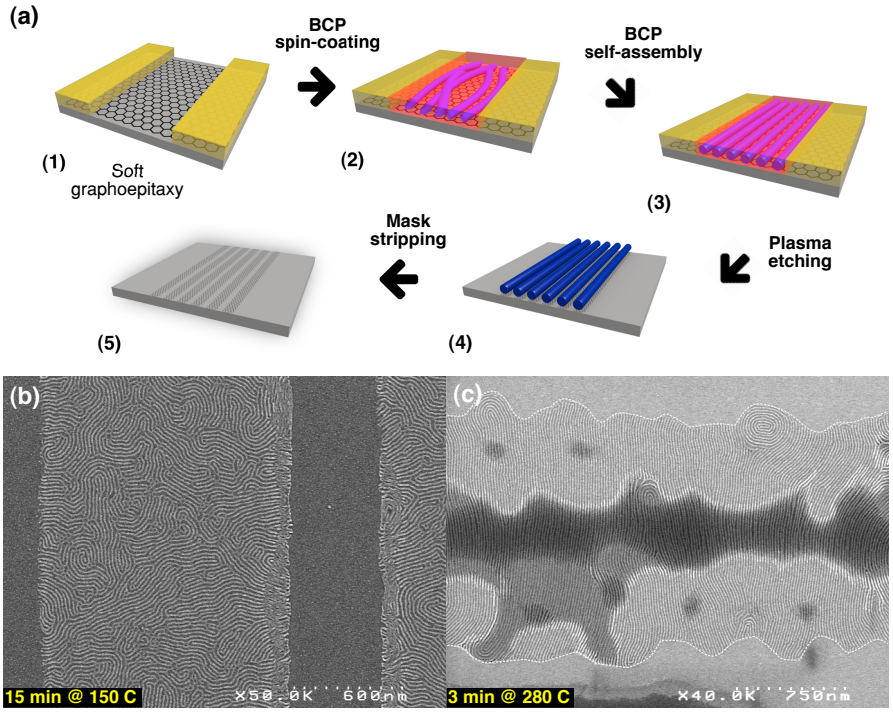

Figure 4.8.: General procedure for graphene patterning (a) graphene on 300 nm SiO_2 substrate is thermal annealing for graphene relaxation and avoid detachment; (b) BCP solution is directly spin coated on graphene and the BCP self-assembly is thermally promoted; (c) PS matrix is removed and PDMS block is oxidized by plasma etching; (d) the mask is stripped and the patterned graphene is obtained.

the fig. 4.8c, cylinders aligns perpendicular to the guiding lines, suggesting one more time a chemical affinity of the PDMS block to the LOR resist. Surface energy measurement gave 44.2 $\pm$ 4 mJ/m^2, where it is a fully disperse energy component. Very low polar forces in PDMS explains this chemical affinity [42]. Even if the alignment increased at 280 °C, disorder is enhanced by the propagation of the lateral disordering and the presence of the many resist residues remaining of G after LOR development.

Greater technological issues in the developed soft graphoepitaxy procedure (reproducibility, high roughness) lead to stand by for this pathway. In the following, patterning transfer with the PS-*b*-PDMS presented in sec. 4.3.2 will be used for the studies on plasma etching and the corresponding characterizations.

4.4. Summary

The self-assembly of the PS-*b*-PDMS 16kg/mol was studied to obtain a ∼10 nm resolution hard mask for graphene patterning. Three approaches were investigated: an underlayer approach, direct spin-coating and the directed self-assembly with soft graphoepitaxy. In the middle layer approach, low self-assembly was attained ($\xi \sim 30 - 50$). Better results were obtained with direct spin-coating by annealing at higher temperatures ($\xi \sim 300$). At the same time, a desired morphology of the PS-*b*-PDMS thin film was obtained (PS wetting on graphene). These results were used with the soft-graphoepitaxy approach, meanwhile high LER on guiding lines affected the direct self-assembly of the PDMS cylinders. The lithography procedure developed in this investigation could also be generalized to fabricate different graphene nanostructures such as graphene nanomeshes or quantum dots that could be envisaged for other applications in functional devices.

Bibliography

[1] J. Bai, X. Zhong, S. Jiang, Y. Huang, and X. Duan, Nature nanotechnology **5**, 190 (2010).

[2] M. Kim, N. S. Safron, E. Han, M. S. Arnold, and P. Gopalan, Nano Letters **10**, 1125 (2010).

[3] X. Liang, Y.-S. Jung, S. Wu, A. Ismach, D. L. Olynick, S. Cabrini, and J. Bokor, Nano letters **10**, 2454 (2010).

[4] T. Pedersen, C. Flindt, J. Pedersen, N. Mortensen, A.-P. Jauho, and K. Pedersen, Physical Review Letters **100**, 136804 (2008).

[5] X. Liang and S. Wi, ACS nano **6**, 9700 (2012).

[6] J. G. Son, M. Son, K.-J. Moon, B. H. Lee, J.-M. Myoung, M. S. Strano, M.-H. Ham, and C. A. Ross, Advanced Materials **25**, 4723 (2013).

[7] T. Li, Z. Wang, L. Schulte, and S. Ndoni, Nanoscale **8**, 136 (2015).

[8] D. H. Kaelble, The Journal of Adhesion **2**, 66 (1970).

[9] D. K. Owens and R. C. Wendt, Journal of Applied Polymer Science **13**, 1741 (1969).

[10] J. Garnier, J. Arias-Zapata, O. Marconot, S. Arnaud, S. Böhme, C. Girardot, D. Buttard, and M. Zelsmann, ACS applied materials & interfaces **8**, 9954 (2016).

[11] D. C. Elias, R. R. Nair, T. M. G. Mohiuddin, S. V. Morozov, P. Blake, M. P. Halsall, A. C. Ferrari, D. W. Boukhvalov, M. I. Katsnelson, A. K. Geim, and K. S. Novoselov, Science **323** (2009).

[12] A. Eftekhari and H. Garcia, Materials Today Chemistry **4**, 1 (2017).

[13] S. Park, J. M. Yun, U. N. Maiti, H.-S. Moon, H. M. Jin, and S. O. Kim, Nanotechnology **25**, 014008 (2014).

[14] Y. Lee, S. Bae, H. Jang, S. Jang, S.-E. Zhu, S. H. Sim, Y. I. Song, B. H. Hong, and J.-H. Ahn, Nano letters **10**, 490 (2010).

[15] X. Liang, B. a. Sperling, I. Calizo, G. Cheng, C. A. Hacker, Q. Zhang, Y. Obeng, K. Yan, H. Peng, Q. Li, X. Zhu, H. Yuan, A. R. H. Walker, Z. Liu, L.-M. Peng, and C. a. Richter, ACS nano **5**, 9144 (2011).

[16] J. Kang, D. Shin, S. Bae, and B. H. Hong, Nanoscale **4**, 5527 (2012).

[17] A. Frommhold, J. Manyam, R. Palmer, and A. Robinson, Microelectronic Engineering **98**, 552 (2012).

[18] A. Frommhold, R. E. Palmer, and A. P. G. Robinson, Journal of Micro/Nanolithography, MEMS, and MOEMS **12**, 033003 (2013).

[19] B. Lee, S.-Y. Park, H.-C. Kim, K. Cho, E. M. Vogel, M. J. Kim, R. M. Wallace, and J. Kim, Applied Physics Letters **92**, 203102 (2008).

[20] L. Liao, J. Bai, Y. Qu, Y.-c. Lin, Y. Li, Y. Huang, and X. Duan, Proceedings of the National Academy of Sciences of the United States of America **107**, 6711 (2010).

[21] R. Raj, S. C. Maroo, and E. N. Wang, Nano letters **13**, 1509 (2013).

[22] D. Briggs, H. Chan, M. J. Hearn, D. I. McBriar, and H. S. Munro, Langmuir **6**, 420 (1990).

[23] K. Nakada, M. Fujita, G. Dresselhaus, and M. Dresselhaus, Physical Review B **54**, 17954 (1996).

[24] Y. Banadaki and A. Srivastava, Electronics **5**, 11 (2016).

[25] C. Stampfer, J. Güttinger, S. Hellmüller, F. Molitor, K. Ensslin, and T. Ihn, Physical Review Letters **102**, 056403 (2009).

[26] J. Brandrup, E. H. Immergut, and E. A. Grulke, *Polymer Handbook*, 4th ed., Vol. 2 (Wiley-Blackwell, New York, NY, 1999) p. 2336.

[27] C. Ozcan and N. Hasirci, Journal of Applied Polymer Science **108**, 438 (2008).

[28] B. H. Kim, J. Y. Kim, S.-J. Jeong, J. O. Hwang, D. H. Lee, D. O. Shin, S.-Y. Choi, and S. O. Kim, ACS nano **4**, 5464 (2010).

[29] S. Wang, Y. Zhang, N. Abidi, and L. Cabrales, Langmuir : the ACS journal of surfaces and colloids **25**, 11078 (2009).

[30] A. C. Ferrari, Solid State Communications **143**, 47 (2007).

[31] Z. H. Ni, H. M. Wang, Y. Ma, J. Kasim, Y. H. Wu, and Z. X. Shen, ACS Nano **2**, 1033 (2008).

[32] R. J. Good, L. A. Girifalco, and G. Kraus, The Journal of Physical Chemistry **62**, 1418 (1958).

[33] N. B. Vargaftik, B. N. Volkov, and L. D. Voljak, "International Tables of the Surface Tension of Water," (1983).

[34] J. C. Moreira and N. R. Demarquette, Journal of Applied Polymer Science **82**, 1907 (2001).

[35] B. B. Sauer and G. T. Dee, Macromolecules **24**, 2124 (1991).

[36] Y. J. Shin, Y. Wang, H. Huang, G. Kalon, A. T. S. Wee, Z. Shen, C. S. Bhatia, and H. Yang, Langmuir : the ACS journal of surfaces and colloids **26**, 3798 (2010).

[37] H. Yokoyama, Materials Science and Engineering R: Reports **53**, 199 (2006).

[38] S.-J. Jeong, J. E. Kim, H.-S. Moon, B. H. Kim, S. M. Kim, J. B. Kim, and S. O. Kim, Nano letters **9**, 2300 (2009).

[39] D. Borah, S. Rasappa, M. Salaun, M. Zellsman, O. Lorret, G. Liontos, K. Ntetsikas, A. Avgeropoulos, and M. A. Morris, Advanced Functional Materials **25**, 3425 (2015).

[40] Y. Chen, K. Peng, and Z. Cui, Microelectronic Engineering **73-74**, 278 (2004).

[41] S. Böhme, C. Girardot, J. Garnier, J. Arias-Zapata, S. Arnaud, R. Tiron, O. Marconot, D. Buttard, and M. Zelsmann (2016) p. 97771W.

[42] M. Żenkiewicz, Journal of Achievements in Materials and Manufacturing Engineering **24**, 137 (2007).

5. Graphene patterning by plasma etching

5.1. Introduction

After the preparation of a self-assembled BCP template, which was the object of chapter 4, now a pattern transfer into the active layer of the device is required. This step is crucial as an efficient transfer must preserve the original template features, and in particular in our case it is critical to control the line width of the nanoribbons. In the nanometer dimension range, a high etching selectivity toward the mask is crucial to guarantee an accurate directional transfer without lateral loss and without damaging the underlayer.

Plasma etching is the most used and efficient technology to generate an anisotropic (vertical) transfer from a lithographic mask [1, 2]. After gas ionization and dissociation by the energetic electrons of the plasma, atoms, radicals and ions species interact chemically and/or physically with the sample surface to produce a directional etching. This plasma etching principle is widely used in nanoelectronics and it has been developed up to an atomic precision [3]. With the outburst of carbon nanotubes and graphene, applications of plasma have been broadened to carbon nanomaterials, in particular for their ability of accurate etching [4].

The major concerns of this chapter are the development of the technological steps and experimental conditions allowing a correct transfer from the self-assembled PS-*b*-PDMS thin film into graphene using plasma etching. It includes the PS etching, PDMS oxidation and graphene etching in a single step. The different mask paths are developed here namely the middle layer and direct spin coating approaches. In view to a potential device development or simply GNRs investigation, it is mandatory to develop a correct mask stripping process. Further, a dry way to clean GNRs by hydrogen plasma after the stripping is also presented. This way, the chemical quality of the GNRs structures is ensured. Since the target substrate is a single atomic carbon monolayer and the lithography mask a 20-nm thick layer, the transfer step is asserted as very challenging.

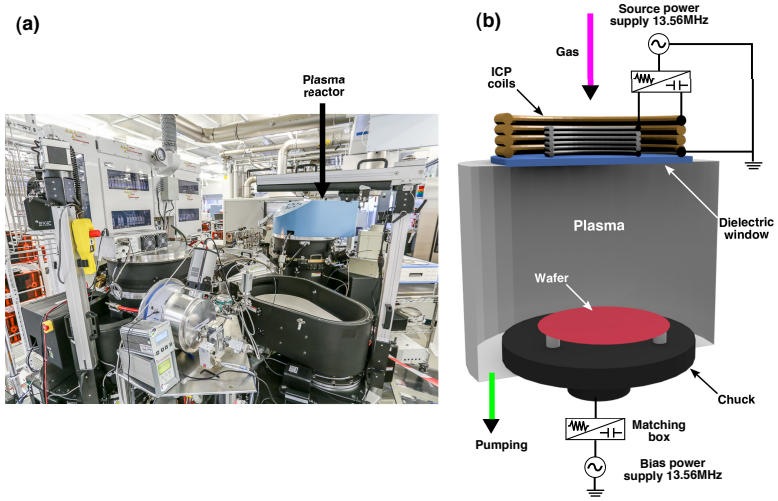

Figure 5.1.: The Centura AdvantEdge Mesa plasma etch ICP reactor used for graphene patterning: (a) Plasma etching equipment in the clean room (©CNRS-LTM), (b) schematic cut view of the etching ICP reactor for CW plasmas (adapted from [5]).

5.2. Experimental procedure

5.2.1. Plasma etching equipment

Experiments were carried out in a plasma reactor adapted for 300 mm wafers. This reactor is an AdvantEdge decoupled plasma source (DPS) from Applied Materials, Inc. An image of the plasma machine in the clean room, and its corresponding schematic cut view, used during this PhD work are depicted in fig. 5.1 a-b respectively.

The reactor internal walls are composed of yttrium and the chamber temperature is kept at 65 °C. The dimension of the reactor are 50 cm and 17.2 cm of diameter and height respectively. The reactor is equipped with two RF power generators which are used to produce the inductively coupled plasma and to control the ion energy. The ICP source generator, supplies a power from 0 to 3000 W at 13.56 MHz, to the two concentric ICP antenna coils that lies on the ceramic roof of the reactor. The RF power is inductively coupled to the plasma through a dielectric alumina window: the RF current flowing in the antenna induces a time varying axial magnetic field in the plasma, which, in turn induces an azymuthal oscillating electric field that accelerates electrons parallel to the reactor walls, making it possible to maintain the plasma at very low pressures with a

high ion density (down to 1 mTorr at 10^{11} to 10^{12} ions/cm^3).

The thermally regulated wafer holder, usually called "chuck", is capacitively coupled to the second RF power supply which afford a "bias"power from 0 to 190 W at 13.56 MHz. The bias power result in the charging of a blocking capacitor between the power supply and the chuck: a DC self-bias voltage develops on the electrode and accelerates ions perpendicularly to the wafer up to, hundreds of volts if necessary. When the bias generator is not in used, ions are only accelerated to about 15 eV, the value of the plasma potential.

For all the experiments, small samples of 1 cm^2 were patched on 300 nm Si wafers coated with 100-nm thermally grown SiO_2, because the carrier wafer type should be similar to the surface composition of the sample (in this case graphene on 300-nm thermally grown SiO_2). The condition of the reactor walls can have a strong influence on the plasma process and consequently the etching result. To guarantee the reproducibility of the chamber conditions, typical cleaning and conditioning steps were made before every plasma etching.

At first, the reactor is cleaned by a SF_6/O_2 plasma without bias to remove silicon oxide layers or similar materials remaining from the preceded experiments. Then the chamber is conditioned by operating the etching recipe on a dummy wafer.

5.2.2. Characterizations

Ellipsometry measurements were performed using a UVISEL ellipsometer from Horiba Scientific installed on the plasma reactor to perform in-situ measurements. Spectral range from 300 to 800 nm and a model composed by Si, SiO_2, graphene and the copolymer layer were used to measure the BCP film thickness in real time during etching.

An Atomic Force Microscopy (AFM) (Bruker Dimension FastScan) was used in automatic mode with a Si tip to evaluate the mask stripping process efficiency. The typical parameters for image acquisition used here were 512 lines with a scan rate of 1.98 Hz. Scan size of images was 1 μm$^2-$ and the image treatment was performed using the free software Gwyddion.

The chemical quality of GNRs was studied by X-Ray Photoelectron Spectroscopy (XPS). XPS was carried out at a base pressure of 10^{-9} mbar with a customized Thermo

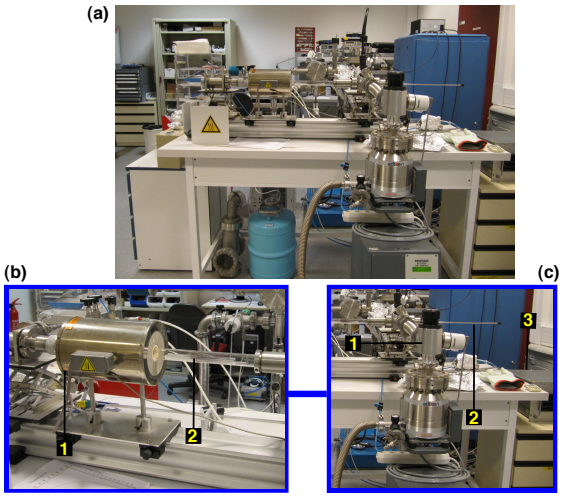

Figure 5.2.: (a) Vacuum oven system used for graphene deshydrogenation, (b) thermal equipment: 1. thermal source and 2. glass sample holder, (c) vacuum equipment: 1. turbo pump, 2. cane to catch the sample holder, 3. temperature set up.

Electron Theta 300 spectrometer using a monochromatic X-ray source Al-Kα (1486.6 eV) with an electron flood gun to reduce surface charging during acquisition. Emitted photoelectrons are collected using an electrostatic lens with 60° angular acceptance. The overall energy resolution of the analysis was 0.5 eV. CASAXPS software was used for fitting and quantification.

GNRs were characterized by Raman spectroscopy using the LabRAM HR Evolution equipment from Horiba Scientific. Measurements were performed using a 100x objective with a blue laser having an excitation wavelength of 488 nm. The laser power was 4 mW and the acquisition time was of the order of 2 seconds to avoid sample degradation. The laser is focused on a few µm and special attention is given to the G, D and 2D bands of the spectrum, which are expected to appear at 1585 cm^{-1}, 1350 cm^{-1} and 2700 cm^{-1}, respectively.

For thermal annealing under vacuum, samples were annealed at 420 °C during 15 min at 10^{-6} mbarr. The oven set up is showed in 5.2a, where the system is composed by a primary and a turbo pumps (5.2c-1) and a thermal source (5.2b-1). The sample was manipulated with a holder (5.2b-2), where it was introduced into the thermal source using a rod (5.2c-2) when the system was at vacuum.

The characterization techniques listed above are supposed to give a specific information at each technological step from the graphene etching to cleaning of the fabricated structures. XPS, Raman and AFM are the most used carbon characterization techniques, as briefly mentioned in the appendix B. Table 5.1 lists the information given by every technique and the step involved.

Table 5.1.: Carbon characterization techniques used for GNRs identification.

Technique	**Information**	**Step**
XPS	• Quantitative analysis of Csp^2 and Csp^3 hybridizations • Detection of carboxyl contaminants	GNR cleaning
Raman	• Crystalline structure of graphene • Quantification of defects	Graphene etching
AFM	• Image patterned graphene • Measurement of GNR height and width	Mask stripping

5.3. Results

5.3.1. BCP & Graphene etching

Middle layer approach

First tested approach was the graphene patterning through the middle layer. This path was developed as an efficient mean to protect graphene during the self-assembly process, meanly from chemical contamination and other damaging agents present in the clean room such as Si dusts and other polymers contaminants from the BCPs. However, as discussed before in sec. 4.3.1, existing PDMS wetting layer is in fact problematic for

any lithography utilization. Indeed, Fig. 5.3a shows the schematic mask transfer of PS-*b*-PDMS into the PMMA middle layer where some residues are observed between the line patterns. The corresponding cross-section SEM image is reported in Fig. 5.3b.

The wetting PDMS bottom layer is resistant to O_2 plasma, and a continuous HBr/O_2 plasma step fails to produce a correct transfer from the PDMS cylinders to the PMMA middle layer. This kind of results have already been observed in other PS-*b*-PDMS studies for nanolithography applications [6], and the solution was to use a short CF_4 plasma step to remove PDMS interfacial layers. However, with the PS-*b*-PDMS 11-5kg/mol used here, the self-assembly process generates horizontal cylinders which height is a few nanometers only. When trying to apply an additional CF_4 plasma to remove the exposed PDMS wetting layer (Fig. 5.3c), it is observed that the oxidized PDMS patterns are etched at the same time. The remaining mask is not resistant enough to allow an efficient transfer of the very thin PDMS template layer into the PMMA (Fig. 5.3d).

Clearly, the fact of adding supplementary technological steps complicates the process optimization. That was the main reason I set aside the middle layer approach as an efficient way to pattern CVD growth graphene by BCPs lithography and to focus rather in the template mask generated by direct spin-coating on graphene.

Direct spin-coating

Using expertise of the LTM lab in PS-PDMS dry etching, first tests on graphene patterning were carried out using the already existing plasma processes (table 5.2). These receipts were modified and adapted to be efficient for our application as it will be described in detail below. The specifications of the etching processes that were tested are depicted in Table 5.2. Every line table corresponds to a plasma etching step, where the experimental conditions are detailed.

The first receipt developed was needed to transfer the PS-*b*-PDMS mask, having the morphology displayed in fig. 4.5a, i.e. annealed at 150 °C, presenting a PDMS wetting layer at the bottom. It was an already existing process though it was necessary to add an additional CF_4 step to remove the PDMS bottom layer and etch the graphene. Experimental conditions are specified in 5.2, receipt "double PDMS". This is made by using a HBr/O_2 mixture composed of 70 sccm of O_2 and 30 sccm of HBr. Both PS

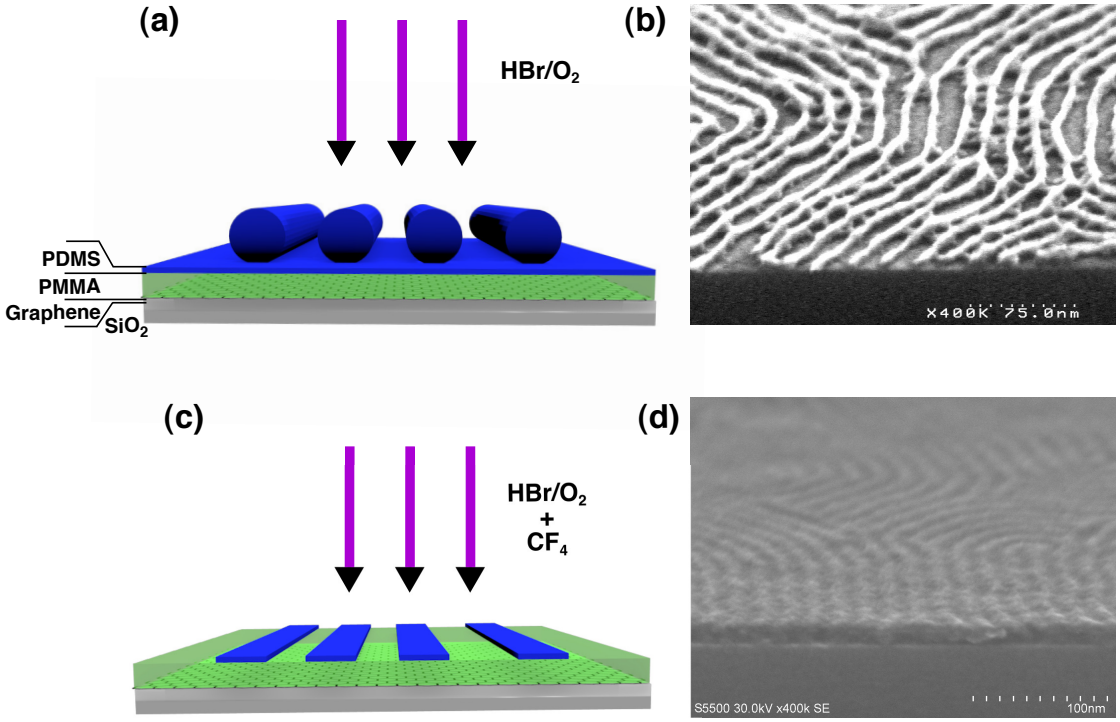

Figure 5.3.: (a) Schematic representation of the PS-PDMS mask transfer on a PMMA film. Cross-section SEM images of PS-PDMS thin film on PMMA underlayer (b) after a 20-second HBr/O_2 plasma etching, faulty transfer is due to the PDMS wetting layer at the BCP-PMMA interface (c) after a 6-second HBr/O_2 plasma etching followed by a 6-s CF_4. Mask intake precludes transfer into PMMA. (a) and (b) SEM images were both tilted of 45°.

Table 5.2.: Experiment details of the etching process tested for the pattern transfer of the PS-*b*-PDMS 16kg/mol into G and its cleaning.

Receipt	**Etching purpose**	**Gas**	**Source Power (W)**	**Bias Power (W)**	**Flow (sccm)**	**Time (s)**
1. Double PDMS	PDMS top layer	CF_4	700	20	100	6
	PS & PDMS oxidation	HBr/O_2	500	10	70/30	
	PDMS bottom layer & graphene	CF_4/He	400	0	25/75	6
2. Chemical	PDMS top layer	CF_4	700	20	100	6
	PS & graphene etching, PDMS oxidation	HBr/O_2	500	10	70/30	-
3. Physical	PDMS top layer	CF_4	700	20	100	6
	PS & graphene etching, PDMS oxidation	HBr/O_2	150	70	70/30	-
4. Cleaning	Conditioning	NF_3	600	0	200	180
	Conditioning	H_2	600	0	200	120
	Cleaning	H_2	800	0	200	20

and graphene are carbon-based materials so they are equaly etched in this step. The HBr/O_2 mixture is used here mainly to provide O atoms that etch PS and oxidize the PDMS. However, the use of HBr with an energetic ion bombardment also guarantee an anisotropic etching (of the PDMS which is simultaneously getting oxidized) thanks to the formation a Br-rich layer on the sidewalls, which prevent them from lateral etching [7]. These species are eliminated during the end of the process and it does not present any source of contamination for graphene.

On the other hand, using the PS-*b*-PDMS mask showed in 4.5, two different plasma conditions were evaluated in term of graphene transfer with the HBr/O_2 plasma: one more "chemical" and the other more "physical". Table 5.2 details in lines 2 and 3 the experimental conditions tested using the same HBr/O_2 gas mixture. At this stage, in-situ ellipsometry was used to measure the etching time of the PS matrix. This step was considered crucial to accurately reproduce the BCP mask patterns into graphene by etching the PS matrix, oxidizing the PDMS cylinders and finally removing the exposed graphene regions between the patterns. As the dimensions of the BCP mask are critically

small, any over-exposition to the etching plasma can generate a lateral etching of the PDMS cylinders and then of GNRs or even completely remove the graphene. It is therefore mandatory to perform a precise etching time of the BCP thin film.

On one side the chemical-type plasma etching was tested with 500W and 10W source and bias power respectively. At this low bias power the ion energy is relatively small, this way the chemical species (mostly O atoms) generated in the plasma phase interact chemically with the sample surface, etching the PS matrix and then graphene when the PS is entirely spent [8]. As a reminder, the PDMS is chemically modified, forming a SiO_x hard mask that protects graphene from etching. On the other hand, when reducing the source power to 150 W and increasing the bias power to 70 W, etching conditions are much physical, i.e. assisted by a very energetic ion bombardment [9].

Fig. 5.4a schematically shows the BCP film morphology and the tested plasma etching. Fig. 5.4b shows the in-situ ellipsometry measurements for both plasma etching receipts. The goal is to calculate the time required to completely etch the PS matrix in both cases. As pointed out in the figure, every plasma etching steps is preceded by a stabilization step (pressure, gas flow). First, the 6-s CF_4 step is used to etch the PDMS superficial layer and then the HBr/O_2 etching step is run. CF_4 etched in both cases around 4nm of PDMS.

As expected, some differences in the etching time of the PS matrix were observed. For the physical etching, 14s were required to remove the PS film while it takes 18s for the the chemical etching. This small time difference turns out to have a considerable impact in terms of graphene etching. Indeed, the corresponding Raman spectra of each sample is shown in Fig. 5.4c. There is no footprint of graphene in the sample etched chemically meanwhile the two characterizatic peaks of graphene plus the D peak appeared in the case of the physical etching, suggesting a correct etching of graphene in this case. This will be subjet to further characterizations.

Chemical etching has a more isotropic action, thereby chemical species could laterally overetch PDMS cylinders during PS removal. Moreover, during PDMS oxidization, oxygen radicals could diffuse into the PDMS chains as a product of its disorganization and finally reach and deteriorate the underlying graphene. In the physical etching, more energetic ions allow a faster etching of the PS matrix without any over-etching and O atoms cannot diffuse down to the underneath graphene. Therefore, physical etching parameters seems to be the better option to accurately reproduce patterns from the

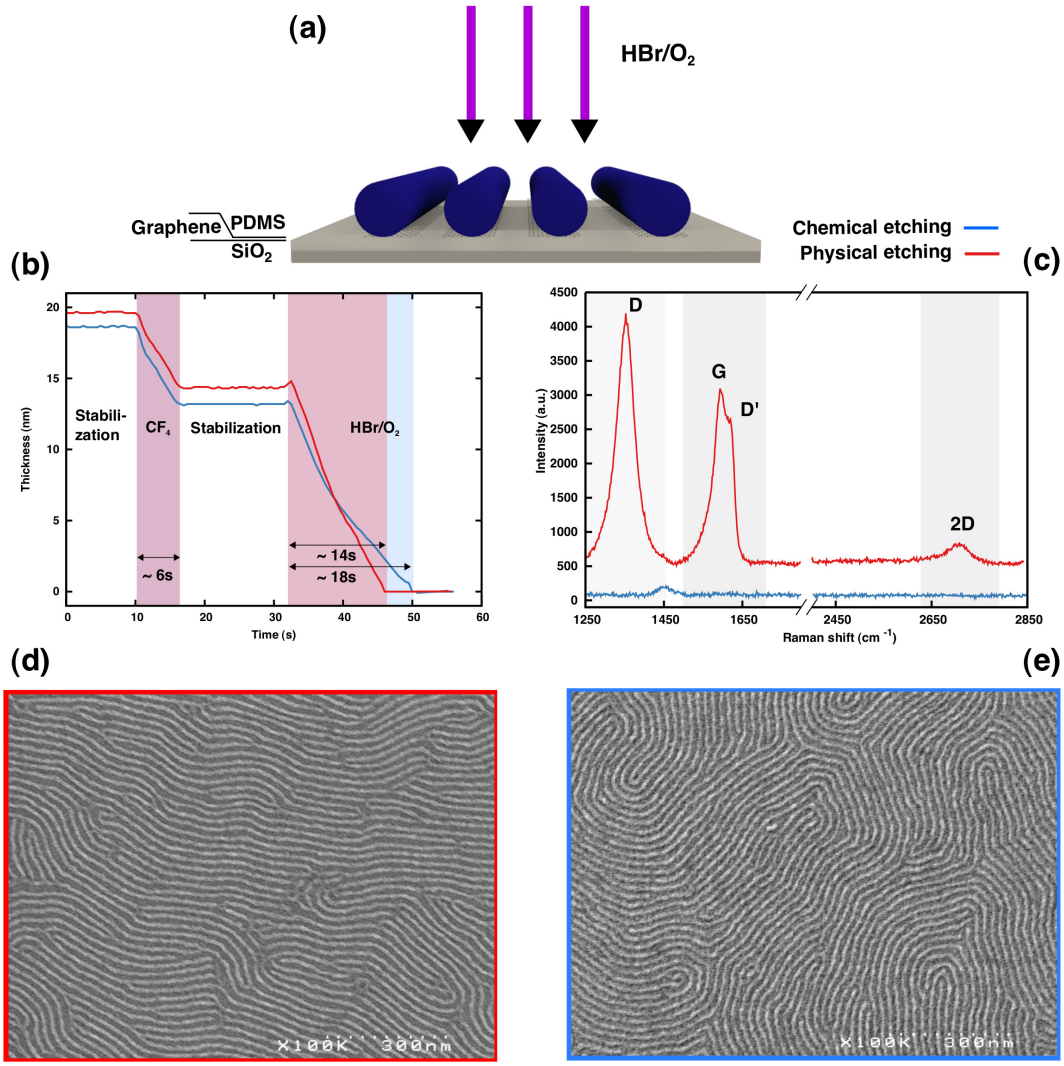

Figure 5.4.: Physical vs. chemical etching conditions for graphene patterning using HBr/O−2 plasmas. (a) In-situ ellipsometry measurements during etching to determine the time required to remove the PS matrix. (b) Raman spectra of samples to evaluate graphene condition after patterning, (c) and (d) top-view SEM images following the physical and chemical HBr/O_2 plasma etching respectively.

PS-*b*-PDMS thin film. Any significant changes in the oxidized PDMS hard mask were observed by SEM 5.4d-e. With the physical process, the bottom of the PDMS mask in contact with graphene is not fully oxidized: this allowed to protect graphene, but this add some complexity when the mask must be stripped in the next step, as will be explained below.

5.3.2. Mask stripping

To demonstrate the real possibilities of BCPs as a sub-10nm lithography technique to fabricate graphene nanoribbons, it is necessary to find processes which are able to remove the remaining mask after graphene etching. BCP stripping is considered as critical since it must preserve the underneath graphene layer. Further studies of the GNRs, such as electrical characterization for example, implies the deposition of metal contacs. Then, a correct stripping of the PDMS mask is mandatory to make good electrical contacts and investigate the intrinsic GNRs electrical properties. Few studies in the literature, specially for the PS-*b*-PDMS BCP template, properly transfer and strip the oxidized PDMS. Among them, Park's group used a base to strip the mask such as TMAH or KOH [10]. Then, the etching rate depends strongly on the temperature and the concentration of the solution. Using standard conditions with TMAH (25% v/v at 50 °C), one can easily lifted off the GNRs.

The usual solution in microelectronics to remove silica by wet etching is the HF solution. Typical concentrations includes 49% and 1% and it is commonly applied at RT [11]. With the aim of avoiding lift-off of GNRs, I started testing the 1% to strip the oxidized PDMS hard mask and reveal the GNRs. Fig. 5.5a shows the result after exposing a sample to HF 1% during 10s. It is clear that lift-off occurs as some graphene grain sheets are lifted off and expelled by capillarity. This is caused by the etching of SiO_2 underneath the GNRs. Then 20s after, all graphene has been lifted off (Fig. 5.5b). The challenge is thus to find the optimal conditions where oxidized PDMS would be removed without lift off, which means that the silica etching rate from the substrate should be lower than that from the mask.

Rather than decreasing the HF etching time, I choose to reduce the HF concentration. A 0.5% solution was tested to strip the PDMS hard mask. I found more satisfactory results using these conditions were the freely orientated GNRs are observed in Fig. 5.5c after 10s of HF treatment. For comparison, I show the case after 20s of treatment

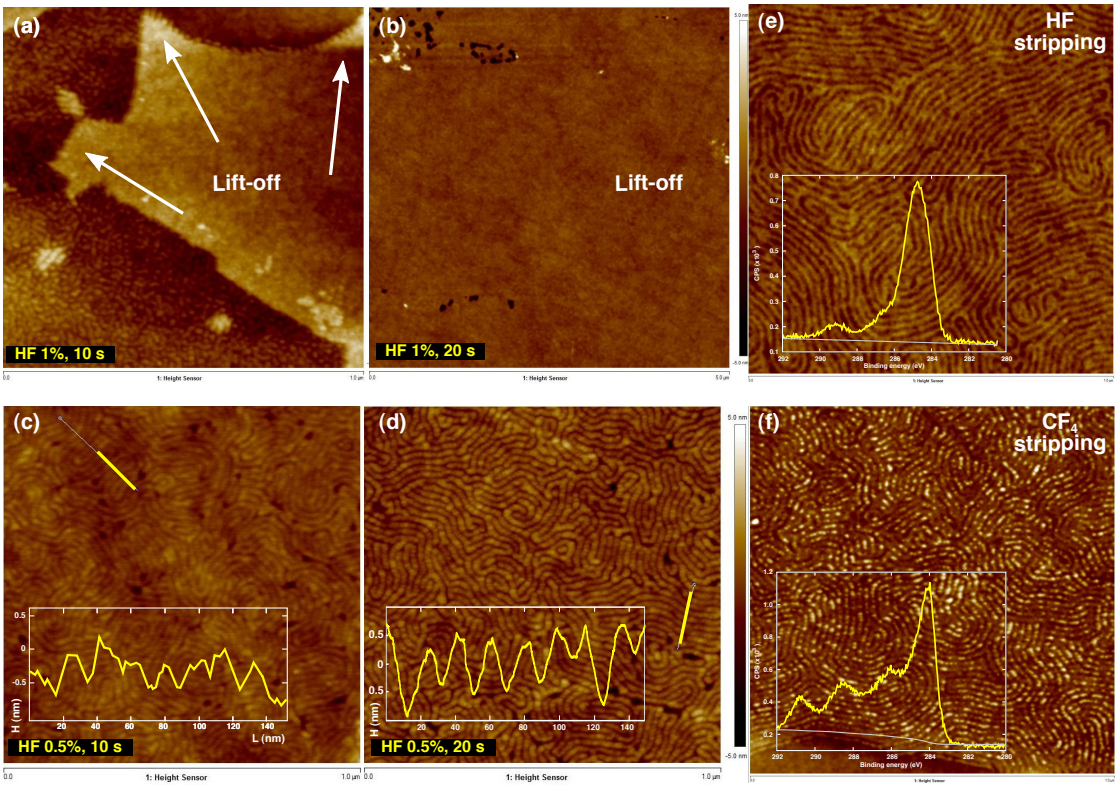

Figure 5.5.: AFM images of the structured graphene after PDMS hard mark stripping by HF at different conditions of HF concentration and time. Higher concentration of HF 1 % v during (a) 10 s and (b) 20 s caused partial and complete lift-off of graphene, respectively. At lower concentrations of HF solution (0.5 % v), the oxidized PDMS hard mask is adequately stripped. (c) After 10 s of wet etching, the measured mean height of GNRs is $\sim$ 5Å, meanwhile for 20 s (d) the mean height is $\sim$ 15 Å. The AFM height profile of the yellow line is inset in images (c) and (d).As a comparison, images (e) and (f) juxtapose wet and dry stripping of the PDMS hard mask by HF and CF_4, respectively. Inset: the XPS carbon peak.

(Fig. 5.5d), where clearly HF start etching the substrate and where a deeper separation between the ribbons is observed.

Dry stripping of the mask by CF_4 was tested too, as it was the selected method used by Son *et al.* [12]. Nevertheless, they did not give any chemical and structural information of the GNRs after the mask stripping. It has been showed an irreversible modification in the valence band state of graphene after fluorine incorporation in graphene by plasma-treatments, to the point of making it an insulator [13, 14]. Inset of Fig. 5.5e-f compares the C1s peak by XPS from wet and dry stripping, which suggests a fluorination of the GNRs (C-F_x bonds are clearly observed in the C1s peak). Moreover the wet mask stripping stir more uniformly the silica mask.

Oxidation

As mentioned earlier, even if the PS matrix of the PS-*b*-PDMS is completely removed, it is possible that the PDMS morphology is not oxidized enough. Indeed, there is one aspect that we had not taken into account before: the oxidation state of PDMS. It is an important condition for correct mask stripping. Not completely oxidized PDMS could not be properly removed by HF, as it is supposed to remove silica. The only way we found to evaluated this was qualitatively by AFM imaging. After in-situ ellipsometry measurements, it was suggested to perform a 14s etching using the physical type conditions to completely etch the PS matrix. The oxidation state of the PDMS hard mask was evaluated by using 12s, 14s and 16s long processes and measuring the thickness of the GNR + mask residues by AFM after HF stripping.

Resulting images are shown in Fig. 5.6. For the three cases, some differences in the GNRs height were observed. Noticeably for 14 s, some mask residues are observed after the HF treatment. It suggests a partial oxidation of the mask, which leaves some carbon residues in the SiO_x matrix that cannot be correctly removed by HF. More uniform stripping was observed for 16s. The corresponding AFM image is shown in Fig. 5.6, which supports the hypothesis of the oxidation state. The 12s case is shown too, where a higher level of mask remains after the HF treatment.

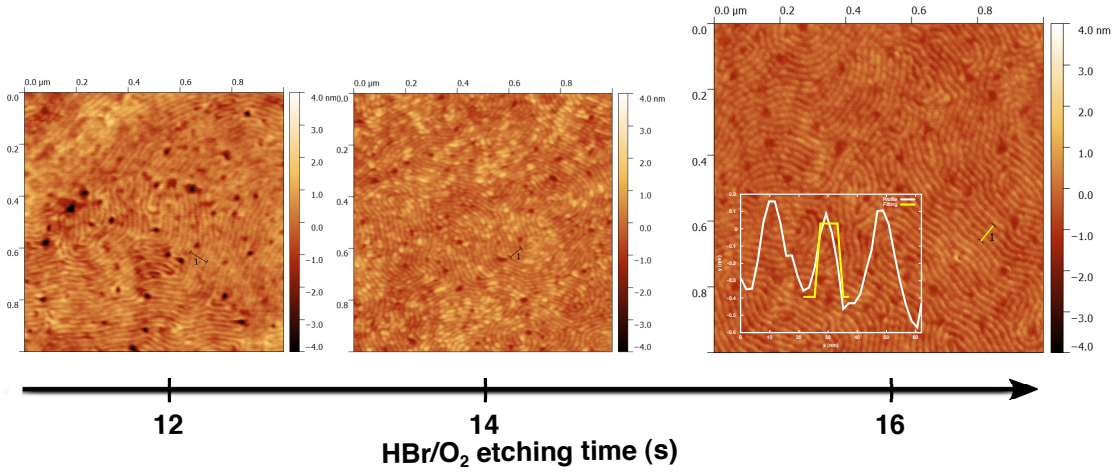

Figure 5.6.: Oxidation evolution in time of the PDMS features for (a) 12 s, (b) 14 s and (c) 16 s of HBr/O2 plasma etching. The mask was stripped with the optimal conditions found in fig. 5.5, i.e., 10 s with HF 0.5 % v. Inset in image (c): AFM height profile of the yellow line.

5.3.3. Dry cleaning

BCP lithography designed here implies the direct spin-coating of PS-*b*-PDMS solution on graphene, and the thermal annealing of the substrate to trigger self-assembly. Even if the graphene crystalline structure quality was investigated in every single step with Raman characterizations, this technique does not provide information on the chemical quality of the as-received state of the graphene nanostructures. The whole graphene patterning procedure, from graphene transfer on SiO_2 substrates to BCP lithography, involves the use of organic materials being a source of contamination for graphene. Amorphous carbon or carboxyl species (O=C-O, C=O) and C-O from Poly(methyl methacrylate) (PMMA) for example, *p*-dopes graphene which results in electronic properties modifications [15, 16].

XPS is a powerful surface-sensitive technique that can be used to analyze a surface by measuring the elemental composition and the chemical state of the elements that composes the first few nanometers (up to 4 nm) of a material surface. XPS is used to quantify contamination, if any exists, at the sample surfaces at the end of each step to investigate graphene damages and surface contaminations.

Several methods have been used primarily to remove PMMA residues following graphene transfer (here the term transfer refers to a change of substrate from copper being the

substrate for graphene CVD growth to SiO_2 and during wich PMMA is used as polymer carrier and already made by Graphenea) and it is a huge problematic nowadays. Methods such as hazardous solvents, during many hours, have been tested without good enough results. Moreover, long immersion of CVD graphene in solvents produce detachment.

On the other hand, hydrogen plasmas are used as an efficient dry cleaning procedure of carbon species coming from PMMA and other polymer contaminants [17]. However, from the published articles focused on GNRs fabrication, no research group has raised the subject of the GNRs contamination associated to their fabrication method and on its impact on their properties. Thus, this issue is addressed and proposes for the first time a solution to provide chemically purified graphene nanostructures. GNRs cleaning is composed of two steps after the mask stripping (sec. 5.3.2) : H_2 plasmas exposition, followed by a thermal annealing for graphene dehydrogenation.

The $C1s$ peak was studied before and after H_2 plasma cleaning by XPS. The presence of functional groups such as O-C=O, C-O, C-C are attributed to PMMA and PS residues. After using the receipt "cleaning" detailed in table 5.2, all these species disappear as highlighted in Fig 5.7f. The $C-Si$ peak growth is explained from PDMS residues that were not properly stripped as it was seen by AFM in Fig 5.7d. The Csp^2 peak is attributed to the graphene. Some Fluorine is detected by XPS as well: it originates from the HF bath and from the reactor walls during the H_2 plasma. However, this impurity vanishes during the final annealing step (Fig 5.7e & g).

Fig. 5.7 shows the cleaning evolution on each technological step. As comparison, the chemical state of the pristine graphene and uncleaned GNRs are showed. The XPS element survey shows a relative decrease of carbon peak intensity during the successive steps. The large reduction of the C1s peak after patterning (with respect to the unpatterned reference), is simply due to the formation of GNRs: the graphene coverage is reduced by approximately 50% by patterning. The C1s peak further decrease during the cleaning step due to the elimination of carboneous polymeric residues from its surface.

The C1s peak was deconvoluted into 7 peaks corresponding to carbon atoms in different chemical environments. Those contributions have been identified [17] and include the sp^2 hybridized carbon from graphene, a sp^3 peak (either hydrogenated graphene or amorphous polymeric residues) and several contributions of C linked to O, which corresponds to PS and PMMA residues and atmospheric contamination. Table 5.3 details fitting parameters of the C1s peak decomposition used for pristine graphene. In Fig. 5.7

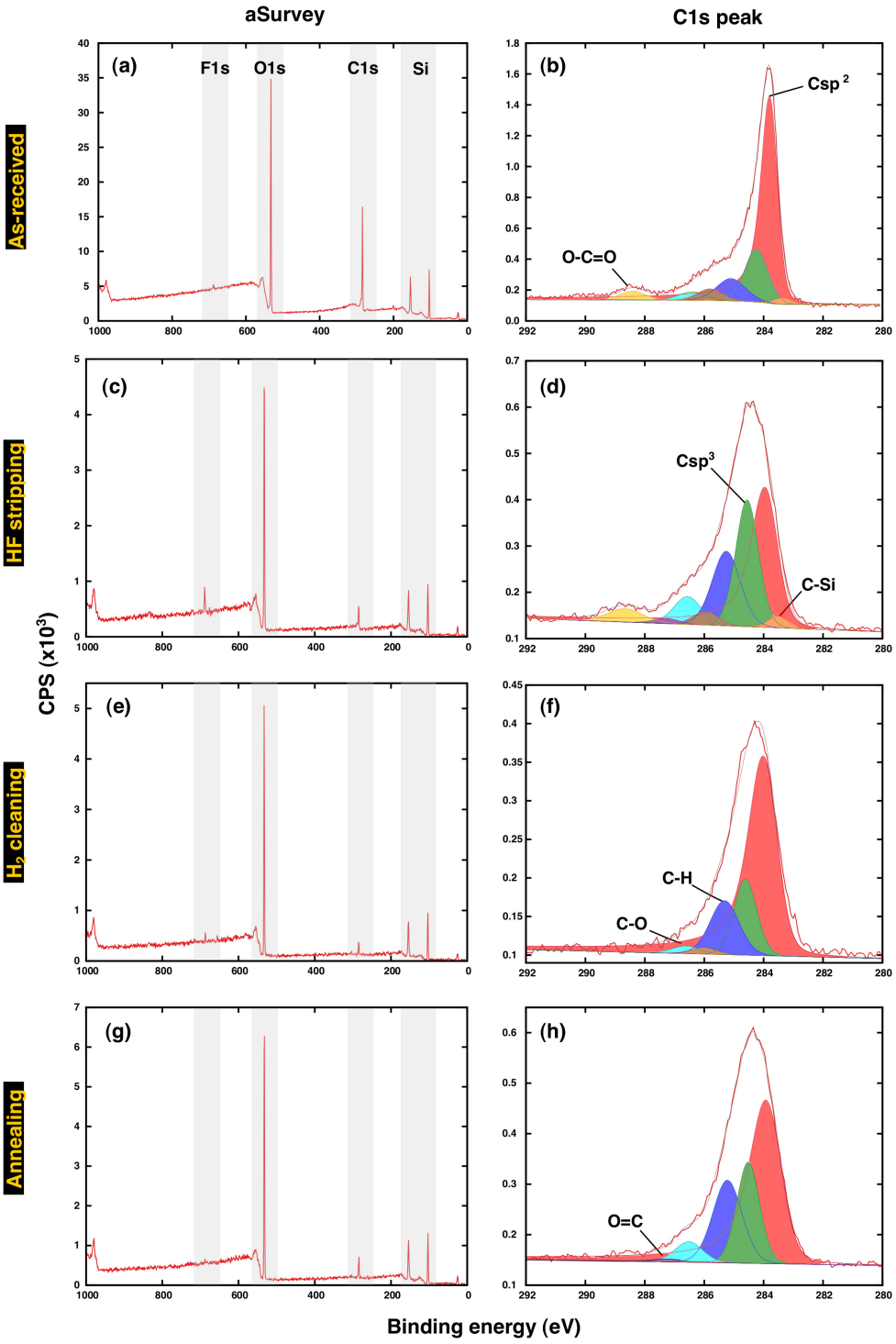

Figure 5.7.: Element survey and evolution of the C1s peak by X-Ray photoelectron spectroscopy at every technological step: (a-b) as-received graphene as referece spectra, (c-d) after PS-PDMS transfer on graphene by HBr/O_2 plasma etching and mask stripping by HF, (e-f) GNR cleaning by H_2 plasmas, (g-h) thermal annealing for graphene deshydrogenation

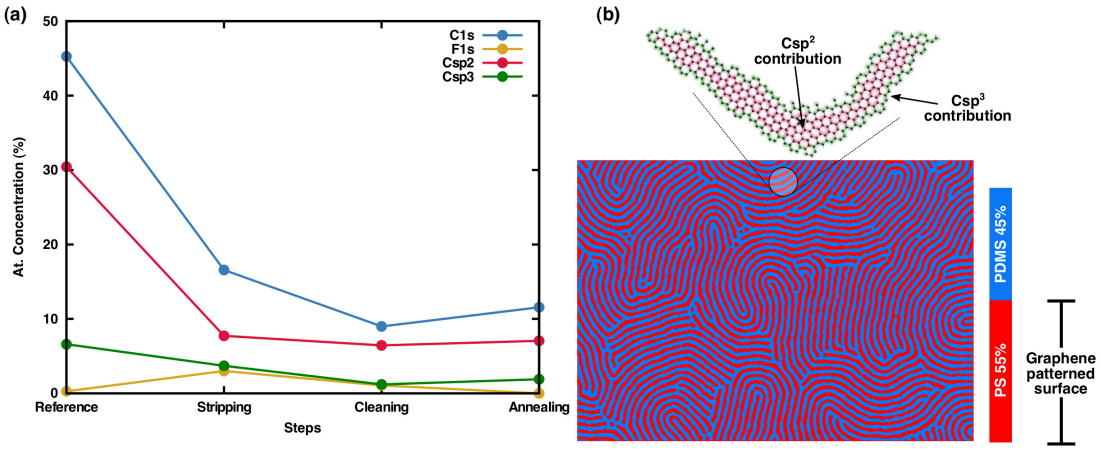

Figure 5.8.: (a) Atomic concentration of carbon and fluor at every step measured from 5.7. The Csp^2 and Csp^3 components are represented similarly. (b) Schematic representation of the portion of the graphene surface that is etched ($\sim 55\%$), using our PS-PDMS lithography mask, and the Csp^2 and Csp^3 main contributions of the GNRs structures to the C1s peak.

the fitted peaks of plasma-cleaned GNRs samples are shown. The more electronegative carboxyl related peaks (such as O-C=O and C=O) appear to vanish during exposure to hydrogen plasma meanwhile C-O peak area diminishes [18]: the cleaning plasma efficiently removes amorphous and oxidized residues from the GNRs. The sp^2 peak relative intensity increase while the sp^3 one diminishes.

Table 5.3.: Fitting C1s peak components parameters of pristine graphene. Binding energy (BE) and the full with at the full width at half maximum (FWHM) are both in eV.

Treatment	**Species**	**BE (eV)**	**Position**	**FWHM (eV)**
	C=C	284.0		0.7
	C-C	284.6	+ 0.6	0.9
	C-H	285.3	+1.3	1.05
	C-C	286.0	+2.0	1.15
	C-O	286.6	+2.6	1.1
	C=O	287.3	+3.3	1.3
	O-C=O	288.7	+4.7	1.4

Hydrogen atoms diffuse into the surface sample where they react easily with carboxyl species O-C=O and C=O. The breaking of C=O bonds in the materials form volatile products, most probably OH and H_2O. Once the hydrogen has saturated the surface, it

leads to the PMMA and PS etching through the formation of volatile CH_4 molecules. Amorphous residues are rapidly etched by this way. However it was shown that highly resistant and 2D residues, heavily oxidized and partially sp^2 hybridized are present at the graphene surface: they corresponds to molecules with aromatic cycles, which stick on graphene by π-stacking. Since the plasma cleaning process relies on etching selectively sp^3 versus sp^2 hybridized carbon, it has difficulties to etch those "ultimate" 2D residues. Actually, the literature suggests that the plasma etches these residues from the edges [19, 20]: this is efficient if the H_2 plasma duration is long enough.

In a similar way, GNRs edges are exposed, and thus subject to lateral etching by hydrogen. The edges of the GNR are highly reactive due the presence of dangling bonds and it is easy for any plasma generated radical to chemisorb on the GNR edges. The high contribution from sp^3 carbon and C-O bonds after GNR patterning is significant from the formation of edges on which O atoms have chemisorb.

After graphene patterning, the GNR edges are thus decorated by O atoms. This probably slows down the lateral etching rate of GNRs by H atoms during the plasma cleaning step in H_2 since H atoms must first extract O from the edges before they can attack the edges. By contrast, the top of GNRs cannot be etched by H atoms because it is protected by an electronic cloud from its unlocalized π-electrons which generates an energy barrier for H chemisorption. This is indeed the way to obtain an etching selectivity between sp^3 carbon and graphene using hydrogen plasmas [21].

Indeed fig. 5.8 shows the relative atomic concentrations of carbon at every step, starting from the reference. The carbon peak intensity drops drastically (around 60% of carbon) due to patterning and cleaning. In the ideal case, after graphene patterning, around 50-60% of graphene surface is removed. Considering the fact that the edges (decorated by O and F) are sp^3, and that a significant lateral etching may have take place, also generating a loss of the sp^2 carbon amount, sp^2 carbon decay (75%) could match with graphene patterning. During hydrogen cleaning, the C1s peak still diminishes mainly due to a reduction of sp^3 carbon while sp^2 one keep relatively constant. Finally, some introduction of contamination was found, due to transportation of the sample out of the cleanroom (to bring them to vacuum oven annealing fig. 5.2 and after annealing when going to the XPS). An amount of C-O and C-H thus remains on the GNRs due to a typical and small atmospheric contamination. GNRs are structures with very reactive edges, the most energetically favorable state is likely these C-O and C-H species.

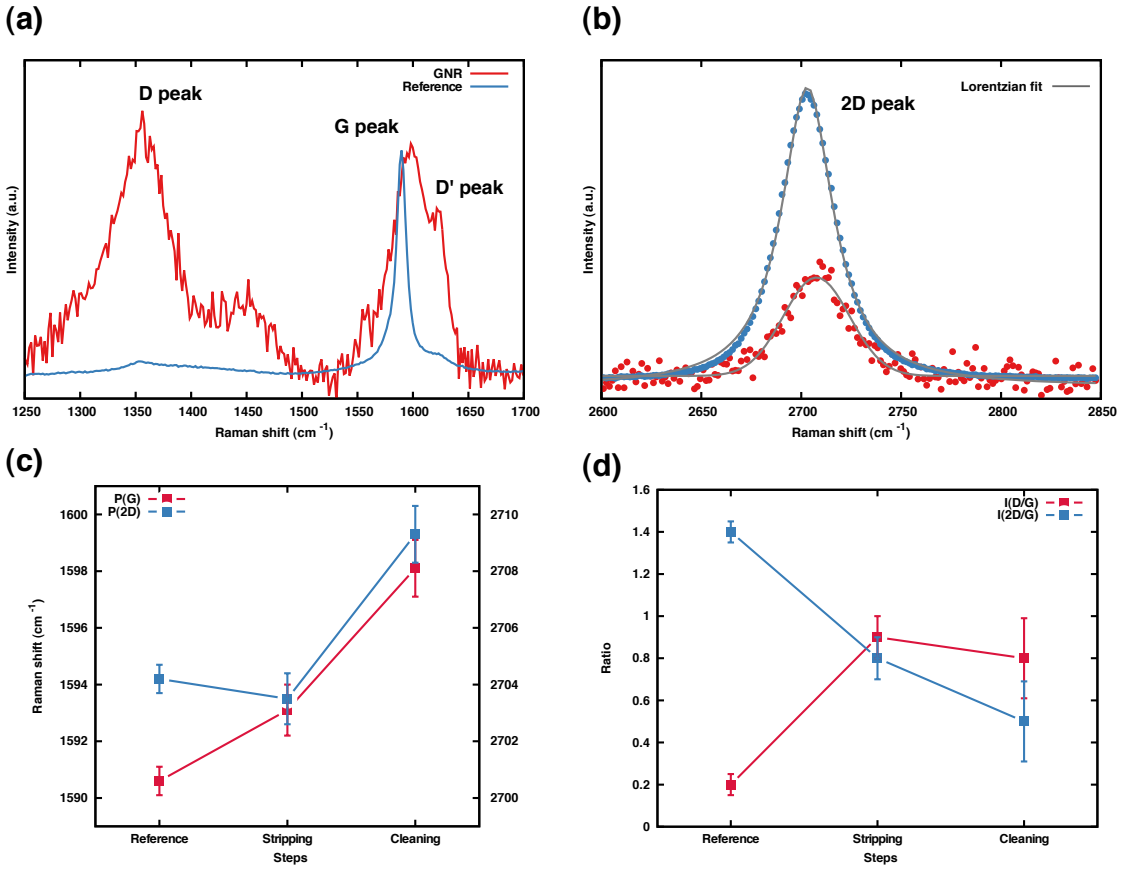

Figure 5.9.: (a) Spectra region showing the G peak and the D and D' defect-induced peaks of reference graphene and GNRs. (b) Region of the 2D peak of the as-received graphene sheets and GNRs both fitted with a Lorentzian function (gray line). (c) Mean positions of the G and 2D peaks at every step: reference, after mask stripping by HF and after GNR cleaning. (d) Mean intensity ratios I(D/G) and I(2D/G) at every step.

After deshydrogenation, the samples were analyzed using Raman spectroscopy to verify GNRs footprint at every step. Raman is a versatile tool and it has been widely used to characterize the electronic structure of graphene, doping state as well as to explore quantum confinement in GNRs [22].

Characteristic G peak is showed in Fig. 5.9a, with the defect induced D and D'peaks. In unpatterned graphene, the G peak is predominant, while the D peak is negligibly small. As few defects are induced during self-assembly, the as-received graphene spectra is compared. After patterning, the intensity of the D peak becomes comparable to that of the G peak, with the display of a first order D peak. This is an evidence of the formation of edges of GNRs: edges act as defects, leading to the strong enhancement of the D peak intensity.

Fig. 5.9b shows representative Raman spectra for patterned and unpatterned graphene in the 2D peak region. Spectra was normalized to the G peak for comparison. It is first noticeable that there is a large difference between the intensities of the 2D bands before and after patterning. Because the intensity is proportional to the number of sp^2-bonded carbon atoms irradiated by the laser spot, the intensity drops after patterning (in the same manner than the sp^2 contribution in XPS) [23]. Both 2D peaks kept the same Lorentzian shape with FWHM equal to ~ 32 cm^{-1}

The evolution of intensities at each step is showed in Fig. 5.9d. Cleaning does not introduce additional defects to structured graphene while a slight reduction in the 2D-G ratio is observed after this step. It is attributed to the lateral consumption of GNRs by hydrogen plasmas. In Fig. 5.9c, the positions of the G and 2D peak are compared. After the mask stripping, the 2D band remains roughly constant but a slight blue shift (about 2.5 cm^{-1}) is observed for the GNRs spectra, which can be attributed to the introduction of oxygen at the edges [24] causing a p-doping. Higher blue shift was observed after cleaning. Smoothing of the GNRs edges by hydrogen plasmas can produce a stiffening of the transverse G-mode in the GNRs. This is due to a lateral confinement effect, accompanied by a stress during the thermal annealing deshydrogenation, both of which produce a blue shift in the G and 2D peaks [25].

At the end of the process, AFM was used for the dimensional characterization of GNRs. Fig. 5.10 shows a $1\mu m^2$ area of structured graphene. The average width spacing and the GNR height are 10.5 ± 2.1 nm and 0.45 ± 0.1 nm, respectively. The height and width distributions are provided as histograms in Fig. 5.10 b and c respectively.

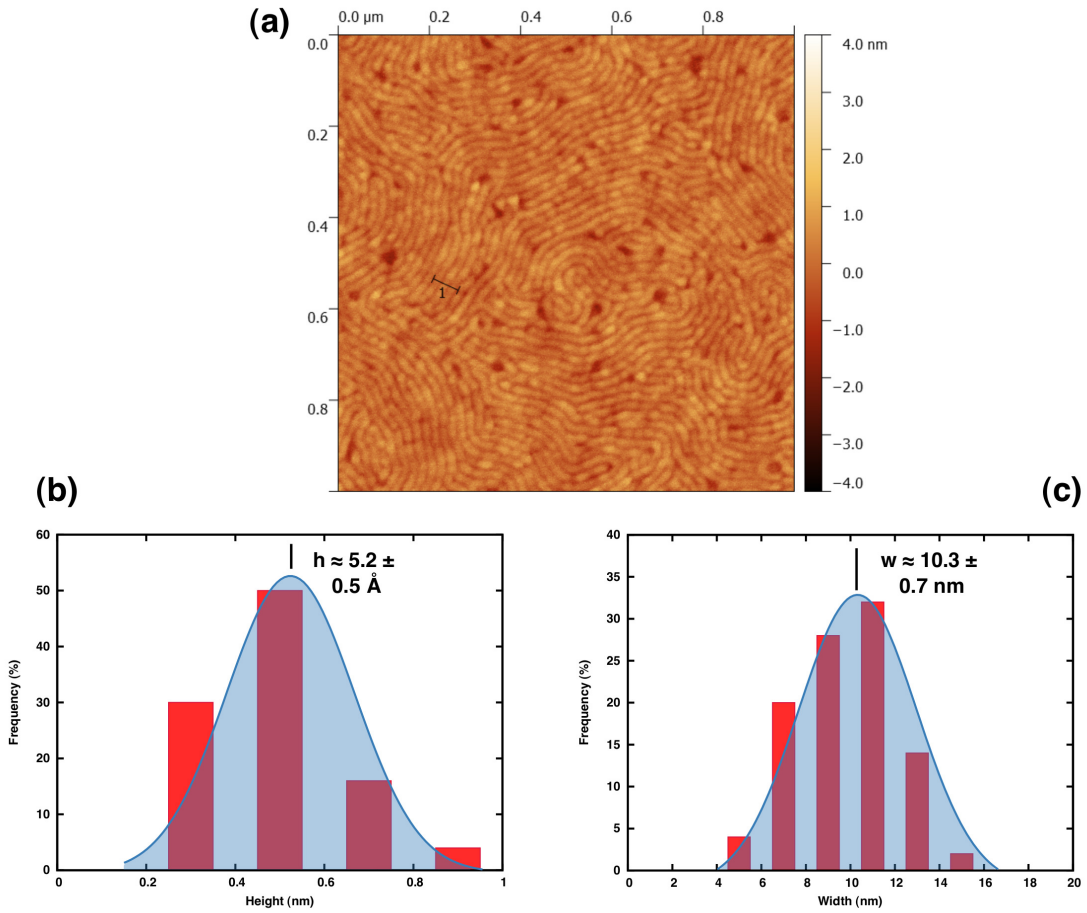

Figure 5.10.: (a) AFM image of GNRs after H_2 plasma cleaning and thermal annealing. (b) Histogram distribution of GNR height. The Gaussian distribution is centered at 0.52 nm. (c) Histogram distribution of GNR width. The Gaussian distribution is centered at 10.3 nm.

Histograms were constructed by sampling 50 profiles in the image and by fitting the positive step to calculate the height and the width of the GNR.

Table 5.4.: Main results of the GNR characterization techniques obtained for the three tested plasma conditions.

Receipts	**Results**			
	Ellipsometry	**XPS**	**Raman**	**AFM**
1. Double PDMS		No Csp^2 atomic concentration decrease observed	G & 2D peaks + D defect peak in spectra	Smooth surface without patterns R_{max} $\sim$ 2 nm
2. Chemical	18 s need for PS-matrix etching	Csp^2 atomic concentration reduction in 70%	No graphene signature	Patterned surface with R_{max} $\sim$ 1 nm
3. Physical	14 s for PS-matrix etching	Csp^22 atomic concentration reduction in 70%	G & 2D peaks + D defect peak in spectra	Patterned surface with R_{max} $\sim$ 1 nm

Table 5.4 summarizes the main results obtained from the characterization techniques at each plasma etching step and how this information can be helpful to determined the quality of graphene patterning. The information given by the table 5.4 grants the physical type etching as the adequate way to tranfer the PS-*b*-PDMS mask toward graphene. Characterization techniques suggest an efficient graphene patterning with: a decrease of Csp^2 concentration by XPS, the graphene signature with defects by Raman and the GNRs with the expected height and width by AFM. Meanwhile, additional characterization will (and need to) be added to confirm this fact. For the other plasma processes, the lack of Raman signature or the constancy of the Csp^2 concentration, leaves a doubt about the quality of GNRs. Indeed the chapter 6 is about electrical characterization and Raman quantification of defects.

5.3.4. Summary

The patterning of graphene is showed through BCP self-assembly lithography. The understanding of plasma etching was a key element for the successful transfer fabrication of GNRs. Better comprehension of plasmas allowed an efficient patterning of atomic

layers thin materials such as graphene by using BCP as a lithography mask. Physical type etching was preferred to avoid a lateral etching of graphene during transfer.

Structuration of graphene was supported by many characterization techniques. Common carbon characterization techniques were used for GNRs, Raman as a practical tool with a graphene footprint, and a D peak for defects, as it is interpreted as edges defects of ribbons. AFM allowed to determine dimensions of graphene nanoribbons: height and width.

GNRs were cleaned after mask stripping by dry methods. XPS showed the efficient removal of carboxyl and amorphous carbon species from PMMA and PS. Graphene patterning by oxygen creates lots of carboxyl species at edges, hydrogen plasmas is an efficient and smooth way to clean and tailor GNRs.

Bibliography

[1] D. B. Graves, AIChE Journal **35**, 1 (1989).

[2] D. M. Manos and D. L. Flamm, *Plasma etching : an introduction* (Academic Press, 1989) p. 476.

[3] K. J. Kanarik, T. Lill, E. A. Hudson, S. Sriraman, S. Tan, J. Marks, V. Vahedi, and R. A. Gottscho, Journal of Vacuum Science & Technology A: Vacuum, Surfaces, and Films **33**, 020802 (2015).

[4] A. Dey, A. Chroneos, N. J. St Braithwaite, R. P. Gandhiraman, and S. Krishnamurthy, Citation: Applied Physics Reviews J. Vac. Sci. Technol. A Appl. Phys. Lett. J. Vac. Sci. Technol. B J. Appl. Phys. Appl. Phys. Lett **31**, 21301 (2016).

[5] M. Darnon, G. Cunge, and N. S. J. Braithwaite, Plasma Sources Science and Technology **23**, 025002 (2014).

[6] Y. S. Jung and C. A. Ross, Nano Letters **7**, 2046 (2007).

[7] G. Cunge, D. Vempaire, R. Ramos, M. Touzeau, O. Joubert, P. Bodard, and N. Sadeghi, Plasma Sources Science and Technology **19**, 034017 (2010).

[8] P. Fauchais, Techniques de l'ingénieur **TIB109DUO**, 1 (2000).

[9] A.-m. Pointu, J. Perrin, and J. Jolly, Techniques de l'Ingénieur **TIB251DUO**, 1 (1997).

[10] S.-J. Jeong, S. Jo, J. Lee, K. Yang, H. Lee, C.-S. Lee, H. Park, and S. Park, Nano Letters , acs.nanolett.6b01542 (2016).

[11] K. Williams, K. Gupta, and M. Wasilik, Journal of Microelectromechanical Systems **12**, 761 (2003).

[12] J. G. Son, M. Son, K.-J. Moon, B. H. Lee, J.-M. Myoung, M. S. Strano, M.-H. Ham, and C. A. Ross, Advanced Materials **25**, 4723 (2013).

[13] R. R. Nair, W. Ren, R. Jalil, I. Riaz, V. G. Kravets, L. Britnell, P. Blake, F. Schedin, A. S. Mayorov, S. Yuan, M. I. Katsnelson, H.-M. Cheng, W. Strupinski, L. G. Bulusheva, A. V. Okotrub, I. V. Grigorieva, A. N. Grigorenko, K. S. Novoselov, and A. K. Geim, Small **6**, 2877 (2010).

[14] S. D. Sherpa, S. A. Paniagua, G. Levitin, S. R. Marder, M. D. Williams, and D. W. Hess, Journal of Vacuum Science & Technology B, Nanotechnology and Microelectronics: Materials, Processing, Measurement, and Phenomena **30**, 03D102 (2012).

[15] X. Liang, B. a. Sperling, I. Calizo, G. Cheng, C. A. Hacker, Q. Zhang, Y. Obeng, K. Yan, H. Peng, Q. Li, X. Zhu, H. Yuan, A. R. H. Walker, Z. Liu, L.-M. Peng, and C. a. Richter, ACS nano **5**, 9144 (2011).

[16] M. T. Pettes, I. Jo, Z. Yao, and L. Shi, Nano Letters **11**, 1195 (2011).

[17] G. Cunge, D. Ferrah, C. Petit-Etienne, A. Davydova, H. Okuno, D. Kalita, V. Bouchiat, and O. Renault, Journal of Applied Physics **118**, 123302 (2015).

[18] S. Yumitori, Journal of Materials Science **35**, 139 (2000).

[19] P. Nemes-Incze, G. Magda, K. Kamarás, and L. P. Biró, Nano Research **3**, 110 (2010).

[20] Z. Shi, R. Yang, L. Zhang, Y. Wang, D. Liu, D. Shi, E. Wang, and G. Zhang, Advanced Materials **23**, 3061 (2011).

[21] B. Thedjoisworo, D. Cheung, and V. Crist, Journal of Vacuum Science & Technology B, Nanotechnology and Microelectronics: Materials, Processing, Measurement, and Phenomena **31**, 021206 (2013).

[22] A. C. Ferrari and D. M. Basko, Nature nanotechnology **8**, 235 (2013).

[23] D. Bischoff, J. Güttinger, S. Dröscher, T. Ihn, K. Ensslin, and C. Stampfer, Journal of Applied Physics **109**, 073710 (2011).

[24] S. Ryu, J. Maultzsch, M. Y. Han, P. Kim, and L. E. Brus, ACS Nano **5**, 4123 (2011).

[25] J. W. Suk, W. H. Lee, J. Lee, H. Chou, R. D. Piner, Y. Hao, D. Akinwande, and R. S. Ruoff, Nano letters **13**, 1462 (2013).

6. Graphene nanoribbons characterization

6.1. Introduction

As manufacturing methods of GNRs has improved in terms of throughput, cost and defects, it has opened up a field of study of their electronic, magnetic, mechanical and optical properties, and simulation frameworks for modeling electronics devices [1]. In this context, there is a growing interesting in designing devices for logic circuitry based on sub-10 nm GNRs, as enough bandgap opening allows the development of high-speed transistor channels for a wide range of silicon-based nanoelectronics.

One of the challenges of graphene-based devices is to reduce the off-state leakage current and improve the I_{on}/I_{off} ratios achieved so far (typically 1 or 2 orders of magnitude) for realistic applications [2]. Added to this, developing a fab-compatible process for producing large-area and high-performance complementary metal oxide semiconductors (CMOS) based on GNR-incorporated nanoelectronics remains a fundamental challenge. This involves not only the difficulties of nanofabrication methods, but also the growth of high quality crystalline graphene on wafer-scale surfaces.

This chapter focuses on electrical characterization of the fabricated GNRs, as possible candidates for digital applications. As these electrical measurements implicate the use of larger surfaces, as contacts are separated from 1 to 10 μm, Raman mapping was used to showed the uniformity on properties and width over these areas. The entire procedure of GNRs fabrication developed during my PhD research is resumed just below.

6.2. Experimental procedure

6.2.1. Entire procedure

Fig. 6.1 resumes the entire procedure developed in chaps. 4 and 5, from graphene patterning and GNRs fabrication.

The method in Fig. 6.1 allows a facile and effective large-area integration of field-effect transistors (FETs) based on densely packed multichannel GNR arrays using advanced BCP nanolithography with PS-*b*-PDMS or other device development. The design of our strategy includes:

1. The use of CVD-grown graphene on 4-inch wafers on 300nm-SiO_2, which is suitable for large-scale device fabrication

2. Annealing of CVD graphene on SiO_2 under vacuum (10^{-2} mbarr) for surface funcionalization and compression at 170 °C during 1 h

3. Direct spin-coating of a 1% v/v PS-*b*-PDMS 11-5kg/mol solution in PGMEA during 30s at 1800 rpm and thermal annealing at 280 °during 3 min, which is a fab-compatible process enabling spontaneous phase separation and formation of densely packed periodic arrays of cylindrical BCP nanodomains

4. Two steps plasma etching of the BCP thin film. CF_4 to etch PDMS surface layer using 500W and 20W source and bias power respectively and a 100sccm flow rate during 6 s. HBr/O_2 plasmas achieved the triple task of PS removal, graphene etching and PDMS oxidation. Accurate patterning was achieved using 150W and 70W source and bias power respectively, and a 70/30sccm flow rate during 16 s

5. Mask stripping of the oxidized PDMS hard mask with a 0.5% v HF solution during 10 s

6. A dry cleaning step using hydrogen plasma at 200 mT using 800W source power and 100sccm flow rate during 20 s and a final thermal annealing to remove the hydrogen atoms which may have remained stuck in the GNRs

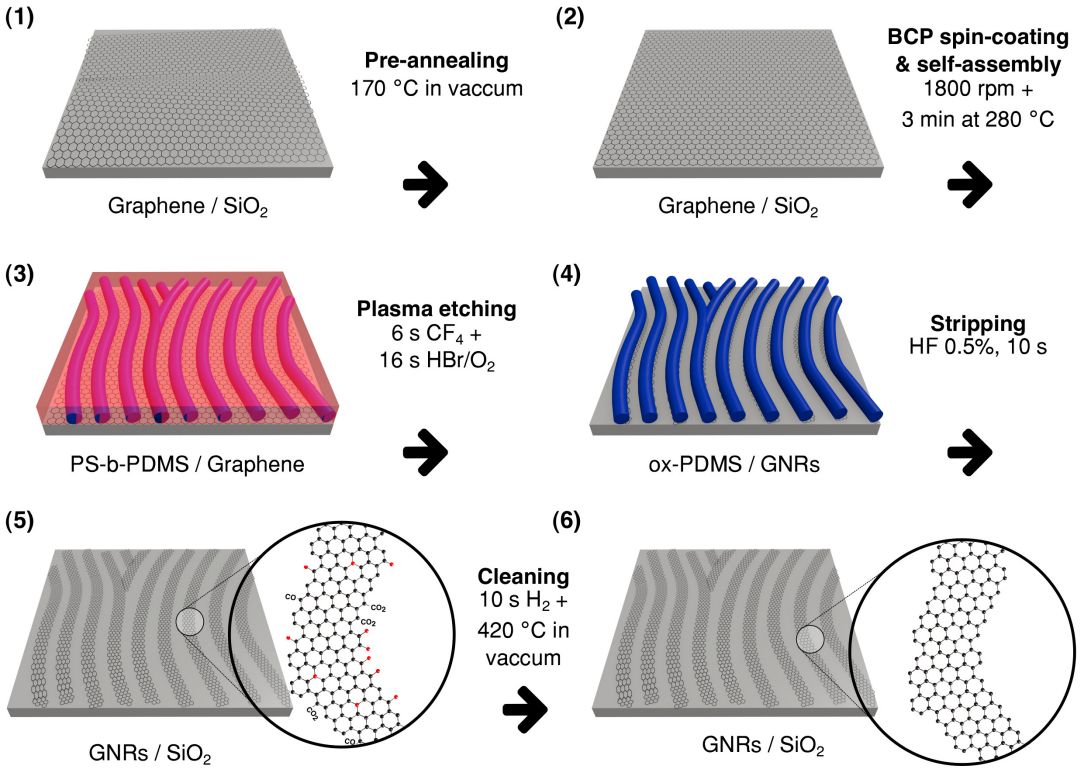

Figure 6.1.: Generic procedure of GNRs fabrication on large surfaces. (1) As-received commercial CVD graphene on 300nm-SiO_2 substrate is cleaved into 1cm^2 samples and (2) thermal annealed in vacuum at 170°C during 1h. (3) PS-*b*-PDMS BCP solution in PGMEA is spin-coated and thermal annealing to trigger self-assembly of the PDMS cylinders. (4) Plasma etching is achieved in two step: CF_4 to remove the upper PDMS film at the BCP-air interface and the HBr/O_2 plasma to remove the PS matrix, oxidize the PDMS cylinders and to etch graphene. (5) Stripping of the mask with a HF solution and (6) cleaning of the GNRs with H_2 and thermal annealing in vacuum.

6.2.2. Raman spectroscopy

Raman mapping GNRs was performed by Raman spectroscopy using the LabRAM HR Evolution equipment from Horiba Scientific. Measurements were performed using a 70x objective with a green laser having an excitation wavelength of 532 nm. The laser power was 4 mW and the acquisition time was of the order of 30 seconds. Lateral focus of the laser was 1 $\sim$ μm. Mapping area was 100 μm^2, scanning from 0 to -10 μm in both x and y directions with a step of 2.5 μm

6.2.3. Contacts deposition

Two methods of contacts deposition were tested. First, metallic contacts deposition was achieved by a classical contact photolithography, with the help of the materials group from the LTM lab. In the other hand, based on the work of Li *etal*. [3] and their work on the Photolithography transfer pattern (PTP), a laborious procedure of contact deposition on GNRs was developed here with the aim of avoiding direct photoresist on GNRs. Both experimental procedures are described below.

Contact photolithography

To electrically characterize GNRs, metal contacts were deposited by conventional photolithography. AZ 5214E resist was spin-coated directly on GNRs (Fig. 6.1) at 5000 rpm spin speed during 50 s. Then the sample was annealed during 120 s at 100 °C. Using a photolithography chrome mask ″Masque-LTMBS‟ to create contact patterns, sample and the mask were aligned and exposed during 6 s with a MJB4 mask aligner equipment from SUSS MicroTec. The sample pursued an annealing at 120 °C during 120 s. In order to inverse resist polarity, the sample was exposed once again to UV light during 31 s, and finally developed with a 1:1 AZ Developer solution during 60 s. Using evaporation deposition, a 100-nm Pd film was deposited and finally the resist was lifted-off during 1 hour in acetone an a final rinse in iso-propanol. Contacts had 1, 4, 7 and 10 μ m separation (L). The entire procedure is schematized in Fig. 6.2a.

Photolithography transfer pattern

Samples of Si < 100 > p++ sacrificial substrate where cleaved in 1 cm^2 from 4-in wafers. Then the negative photoresist was spin-coated at 4000 rpm during 1 min on the cleaved substrates. Soft bake at 150 °C was necessary for solvent evaporation for 90 s. Photoresist was exposed for 3 minutes at 10.4 cm from objective (videoprojector lithography), developed for 4 s in AZ 1:4 developer solution to removed the exposed zones and rinsed during 5 min in DI water. Deposition of 100 nm of metal was achieved with a PLASSYS equipment in clean room conditions. Metal on resist was lifted-off during 1 h in acetone and a final rinsing with iso-propanol. A second stage consisted in spin-coating PMMA A9 from Microchemicals, at 1500 rpm for 1 minute. The PMMA-gold layer was then detached from the substrate with a substrate etching in NaOH 1M solution at 50 °C until complete detachment. Several rinses in DI water are required to properly remove NaOH crystals. By the method of "fishing", the PMMA-gold film was transferred and placed on the GNRs sample surface and the stack was dried in the air during 30 min. Several cycles of 30 s in acetone, 10 s in iso-propanol and N_2 flow drying were repeated until PMMA removal. Finally a solf-bake at 100 °C for 1 h in vacuum to build contact bonding with GNRs is required. The complete optimized process is schematized in Fig. 6.2b.

6.2.4. Electrical measurements setup

After contacts deposition, contacted sample is composed of a P++ (100) Si substrate, a 300-nm silica film, patterned graphene and 2 on-top metallic contacts. This stack constitutes the back-gated FET used to prove the concept of bandgap opening in graphene. Electrical measurements were performed using a probe station facility from the SINAPS lab in CEA-INAC. It is composed by an optical microscope (OLYMPUS SZ40), probe positioners and a lamp, as visualized in Fig. 6.3a- 1,2,3 respectively. The sample was placed on a metal chuck and contacted with the use of 2 or 3 microtips (Fig. 6.3b- 1& 2), Measurements where performed with a Keithley 4200-SCS equipment (Fig. 6.3c). The sample was characterized with the I_{DS} vs. V_{DS} curve at a fixed V_G, and then with the transcharacteristics curve I_{DS} vs. V_G at a constant V_{DS} value.

The 2-points measurement is a simple resistance measurement, it was performed by applying drain-source voltage (V_{ds}) from +0.5V to -0.5V, compliance was changed observing the maximum drain-source current obtained. Output was drain-source current,

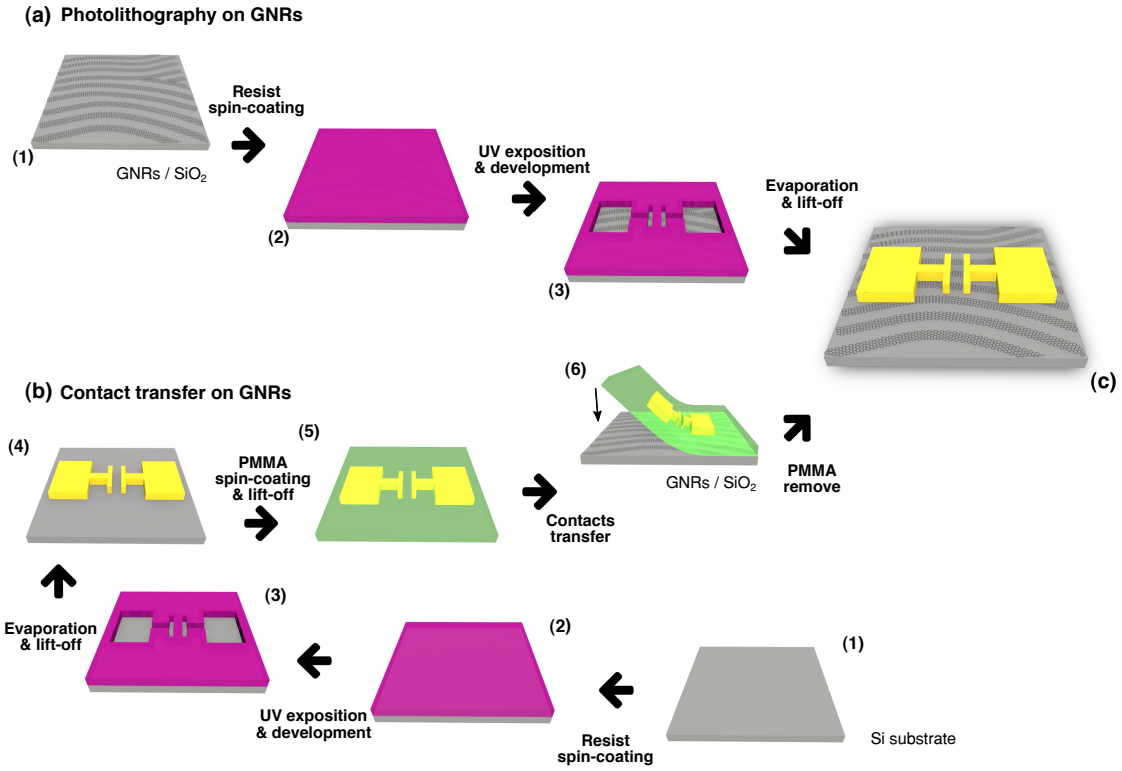

Figure 6.2.: Contact deposition procedures: (a) using a classical contact photolithography or (b) the transfer of the metallic contacts. In the procedure using photolithography, (1) photoresist is spread-out on the GNRs surface and soft-annealed followed by a (2) UV exposition and development. (3) Metallic contacts are deposited by evaporation and (4) lifted-off in acetone. In the contacts transfer method, (1) photolithography is realized first on a Si sacrificial substrate where (2) the photoresist is spin-coated and followed by a soft-annealing. (3) The photoresist is exposed to the UV light and developed. (4) Metallic contacts are deposited by evaporation and the photoresist is lifted-off with acetone. (5) A thick PMMA film is spread-out on the metallic contacts and the stack PMMA/contacts is lifted-off from the Si substrate. (6) The PMMA film floats on the solution surface, which is "fished "and transferred on the GNR, and finally the PMMA is remove with acetone. (c) Metallic contacts on the GNRs array.

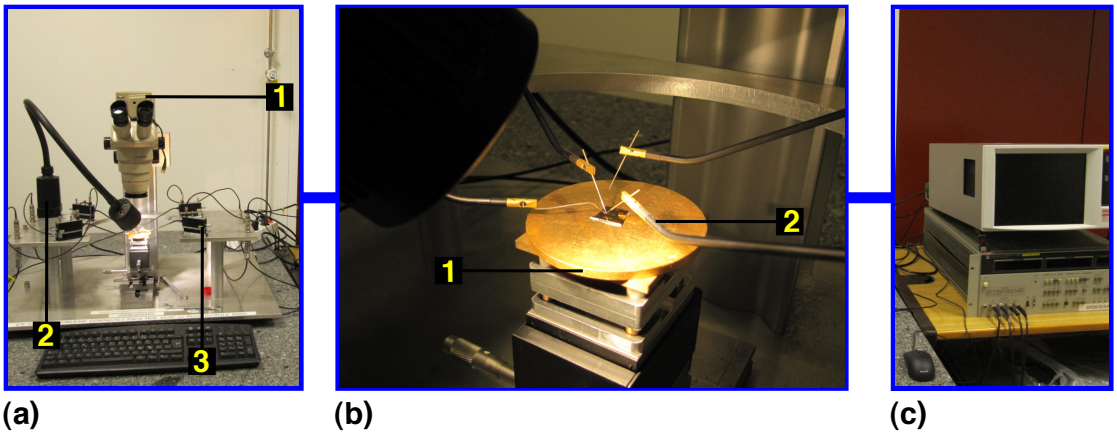

Figure 6.3.: Probe station facility for electrical characterization. (a) Sample set up: 1. Microscope, 2. Lamp and 3. Probe positioners (b) Measurement set up: 1. Wafer chuck and 2. Probes (c) Parameter analyzer for I-V measurements.

and no back-gate voltage was applied.

During 3-points measurement a third tip is put on the sample holder, which is a metallic structure and by which is possible to apply a backgate voltage (V_{gs}). The measurement is performed by applying a source-drain voltage of 0.5V with a bias sweep on the third tip going from -30V to 30V, a step of $V_{gs} = 0.5$ V is used. A double sweep is often used to reduce noise.

It is possible to sweep V_{gs} in order to obtain a better measurement I_{on} and I_{off} . A relatively low speed of sweep is crucial to have good datas, but a first study to look for switching behavior can be done at high speed. Positive or negative current only depends on system convention, these values can be changed in sign to match graphs shape from literature.

6.3. Results

6.3.1. Raman mapping

The establishment of a fabrication procedure allows to investigate the intrinsic properties of GNRs. It is important to emphasize the fact that all steps developed here aimed for clean-room fabrication, then the process is suitable for large scale production, guar-

anteeing high chemical and structural quality during the entire procedure. As further electrical characterizations are considered on the GNRs fabricated here, contact deposition was realized by contact photolithography where the typical drain-source distances vary from 1 to 10 μm. Then a need to ascertain characterization of GNRs under larger areas arisen.

Raman mapping of patterned graphene performed on 100 μm ^{2} areas are shown in Fig 6.4. Raman spectroscopy has gained popularity in the quantification of defects in nanometer-sized graphene objects. Indeed the disorder D peak originating from scattering at the ribbon edges, is introduced during graphene etching [4, 5]. The GNRs edges could be interpreted as an amount of Csp^3 border (one-dimensional defect) with respect to the total Csp^2 crystalline area. From this argument, the average distance between defects L_D can be extracted [6]. The Cançado relation in terms of the excitation laser wavelength λ_L, used during Raman measurements:

$$L^2{}_D(nm^2) = (1.8x10^{-9})\lambda^4{}_L \frac{I_D}{I_G}^{-1} \tag{6.1}$$

allows to quantify L_D from the integrated intensities of the D and G peaks I_D/I_G [7]. As the measured surface has a homogeneous matrix of GNRs, with a periodic width, the distance between defects is taken as the average GNR width (w). For a good approximation, it is supposed that the point defects are only present at the GNR edges, and a mix of edge chiralities AGNR and ZGNR. Fig. 6.4b shows the 2D distribution of the calculated GNRs width in a 100 μm^2 area.From this, the GNR mean width was calculated to 12 $\pm$ 1 nm, which perfectly matches with AFM measurements in Fig 5.10. On the other hand, it shows that the H_2 plasma cleaning procedure does not damage significantly the GNRs by lateral etching meanwhile it efficiently cleans graphene from amorphous carbon and other carboxyl groups.

Moreover the I(2D/G) intensities ratios on the same surface were calculated, displayed in 6.4a, where mean measured ratios are 0.6. As the 2D-peak depends on the illuminated area, is expected a decrease of the I_{2D}/I_G coming from the reduction of the amount of graphene [8]. Then, it proves the increase of the I(D/G) ratio comes mainly from graphene patterning on the measured area. These results could be generalized to larger areas and then to use these values on electrical characterization or further studies.

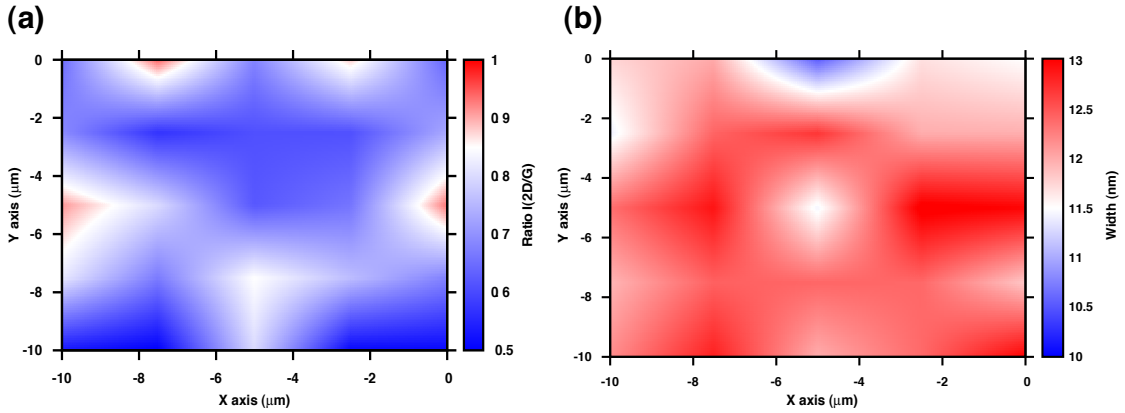

Figure 6.4.: Mapping of GNRs with Raman spectra on a 100 μm ^{2} area. (a) I(2D/G) ratio intensities and (b) the GNRs average widths calculated from the I(D/G) ratio intensities and the Cançado relation [7]. The experiments were performed with a green laser $\lambda = 532$nm

6.3.2. Electrical characterization

From section 3.1, a transition of the electrical regime from its semi-metalic nature, to a semiconductor behavior through bandgap opening via the graphene structuration is expected [9]. And this transition could be useful in the recognition of the graphene patterning from the BCP mask. Then electrical characterization was used as a complementary characterization method to the different plasma etching tests, detailed before in section 5.3.1. These measurements could be conclusive to affirm the presence of GNRs. Otherwise, they are used to evaluate electrical properties at the end of the process such as career mobility through the GNR and the bandgap opening value induced by the patterning.

As represented in Fig. 6.5a, a back-gated FET was fabricated from the GNR arrays using conventional photolithography and the photolithographic transfer pattern detailed in section 6.2.3. The three-terminal device consisted of a GNR channel with metallic source and drain contacts, a highly p-doped Si back gate (0.005 Ω·cm) and a thermally grown 300 nm-thick SiO_2 gate dielectric. Contacts were deposited in the center of the sample, then multiple GNRs channels connect arbitrarily the source and the drain (Fig. 6.5f). Due to this configuration, around 20 % of the metallic contacts were successfully working, the other were open circuit, short circuit or broken contacts.

Devices fabricated by photolithography had a channel length of 1, 4, 7 and 10 μm

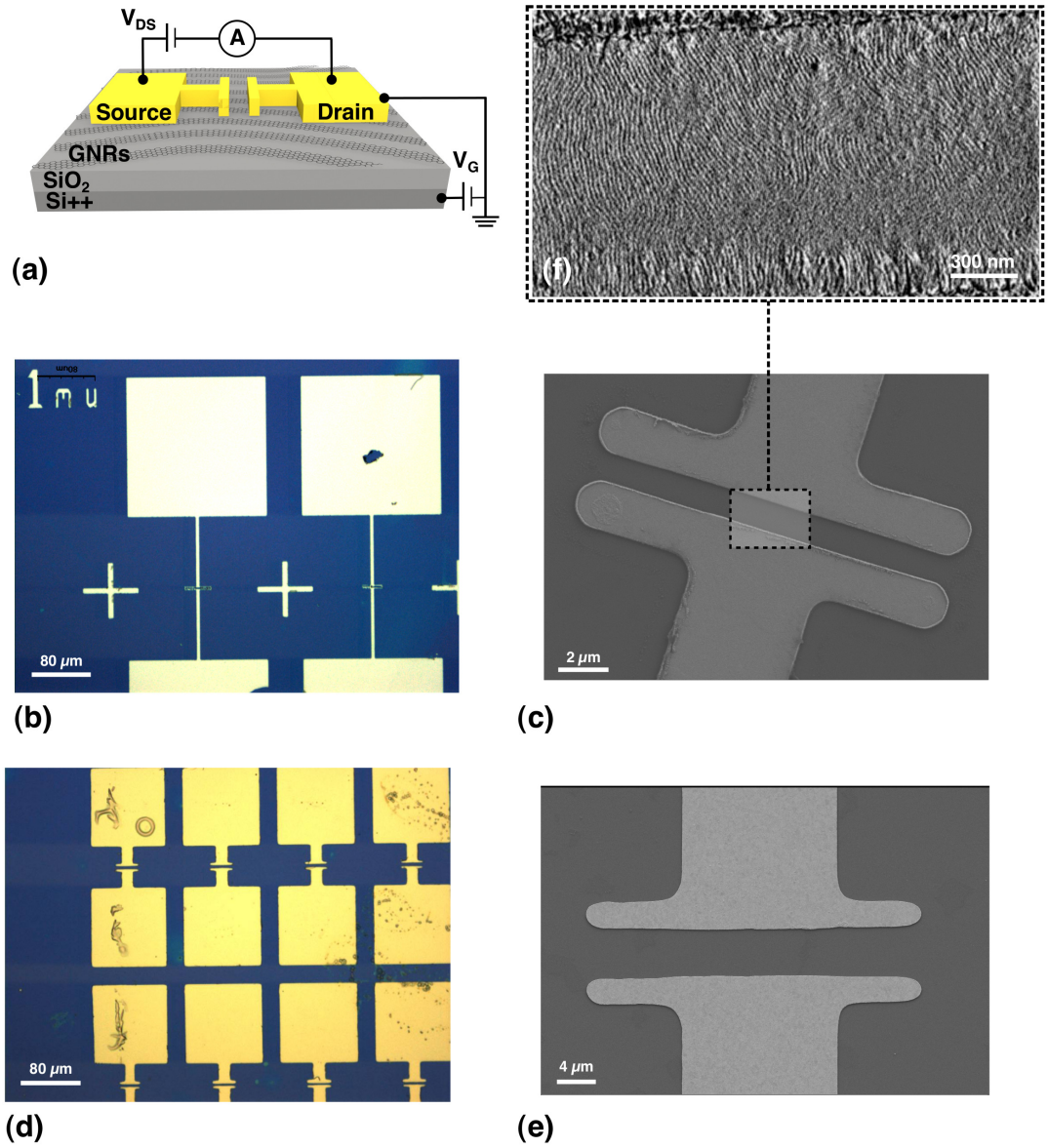

Figure 6.5.: (a) Schematic representation of the back-gated FET used for electric characterization of the graphene structures fabricated by BCP lithography. (b) optic and (c) scanning electronic microscopy top-view images of the source and drain Pd contacts deposited by photolithography. The distance length was 1 μm. Three additional channel lengths of 4, 7 and 10 μm were designed with the same mask (not shown). For the TPT method, Au contacts were finally transfered on the GNRs surface. Figures (d) and (e) show the top-view images by optic and SEM respectively. (f) Zoomed top-view SEM image of the GNRs, linking the source and drain Au contacts showed in (c). The image contrast and bright was imagery treated for GNRs evidence.

and a channel width of 15 μm. Palladium was chosen as metal for contacts as it seems to offers the lower metal-graphene junction resistance [10]. Fig. 6.5b-c show optic and SEM images of the Pd contacts made by photolithography. Besides, the PTP method provided a way of metallic contact deposition without the need of any direct photoresist spreading. Despite the aim to have Pd contacts too, they lifted-off at the end of the process during PMMA removal (figs. 6.2 2-6) resulting from a lack of adhesion. Other metals having low junction resistance were tested such as Ni and Cr [11, 12], which lifted-off too. Finally it was found that Au contacts adhere well after PMMA removal, but had a higher junction resistance than Pd. Channel length were 2, 3 and 4 μm and channel width 30 μm. The results of the electrical measurements are detailed below.

Photolithography contacts

Fig. 6.6a shows the schematic of the sample made by photolithography. 100-nm thick Pd source and drain contacts, constitutes the back-gated FET. Characteristic I-V graphs showed in Fig. 6.6 corresponds to 4 μm and 15μm channel width.

As a reminder, in chapter 5, different plasma etching receipts were tested in order to accurately transfer the PS-*b*-PDMS mask into graphene. In this process, the electrical properties of the supposed patterned graphene were measured. Fig. 6.6 shows the current-voltage (I-V) characteristics of the back-gated FET at $V_G = 0$ V, after the graphene was etched by the "double-step" plasma etching receipt. This graph shows a ohmic regime behavior with high current values (hundredths of milliamperes), which is not expected for GNRs. As graphene is not etched, the likely formation of C-F bonds by the CF_4 plasma, introduces electron acceptors and causes a decrease in electron mobility, and this could further explained the observed change in the transport properties of the graphene layers, with respect to the as-received graphene layer (Fig. 6.6c). Indeed the tunning of the electrical properties by the periodical exposition of pristine graphene to the CF_4 plasma was previously reported [13]. In the opposite case, the chemical etching does not show a significant electrical current passing through GNRs, which confirms once again the etching or structural damaging by the chemical etching (inset of Fig. 6.6b).

Fig. 6.6c shows representative current-voltage (I-V) characteristics of the FET based on unpatterned graphene sheets (blue curve) and the graphene etched by physical etching (red curve), measured at $V_G = 0$ V. When the graphene sheets were used as the conducting channel of the FETs, we observed typical metallic behavior, as predicted

by the theory. Next, measuring electrical response of the FET with GNRs arrays, the current measured in a similar range of V_{SD} exhibited a substantial decrease of 5 orders of magnitude with a highly nonlinear IV relationship (inset of Fig. 6.6c), indicating the emergence of semiconductor behavior (or band gap widening) by the lateral confinement effect resulting from a correct graphene patterning.

The $I_{DS} - V_{DS}$ characteristics became nonlinear in the GNR FETs regardless of the applied gate voltages, without significant hysteresis at RT conditions, in contrary to previous reports [14], needing vaccum or low temperature conditions to avoid hysteresis effects. As the gate voltages were applied, substantial modulation of current was shown due to the movement of the Fermi level. These observations indicate the semiconductor nature of the GNR, which is attributed to the formation of a bandgap in graphene due to the quasi-one-dimensional confinement of the carriers [15, 16, 17, 18].

The semiconductor behavior of the GNRs was also demonstrated by the behavior of the transfer curve (i.e., the source-drain current I_{SD} as a function of the gate voltage V_G) obtained at RT conditions, as shown in Fig. 6.6d. One of the parameters allowing to qualify the FET performance is the ratio between the current at the FET open state I_{on} and the current at the closed state I_{on}. The I_{on}/I_{off} ratio must be as large as possible in order to obtain a clear characteristic between the two states. The simplest and most widespread way used to determine the I_{on} and I_{off} values is simply to take the maximum current value on the Fig. 6.6d for I_{on} and its minimum value for I_{off}. From Fig. 6.6d, the I_{on}/I_{off} ratio was calculated to ~ 4. These results confirm the trend already found in chapter 5, as the physical etching for appropriate transfer ot the PDMS cylinders into graphene.

Photolithography transfer patterns

The quality of the GNRs after fabrication was a major concern, as the very reactive edges play a fundamental role in the optoelectronic characteristics of the GNRs [19, 20]. Even if the electrical properties measurements were tested as a proof-of-concept, to confirm the patterning of graphene by BCP lithography, it is desirable to evaluate the possible impact on the electrical performances, when the contacts are deposited by photolithography. The main issue using photolithography is the direct redeposit of photoresist after GNRs cleaning. The PTP method (Fig. 6.2b) provides a solution to directly deposit metallic contacts on GNRs without photoresist spin-coating.

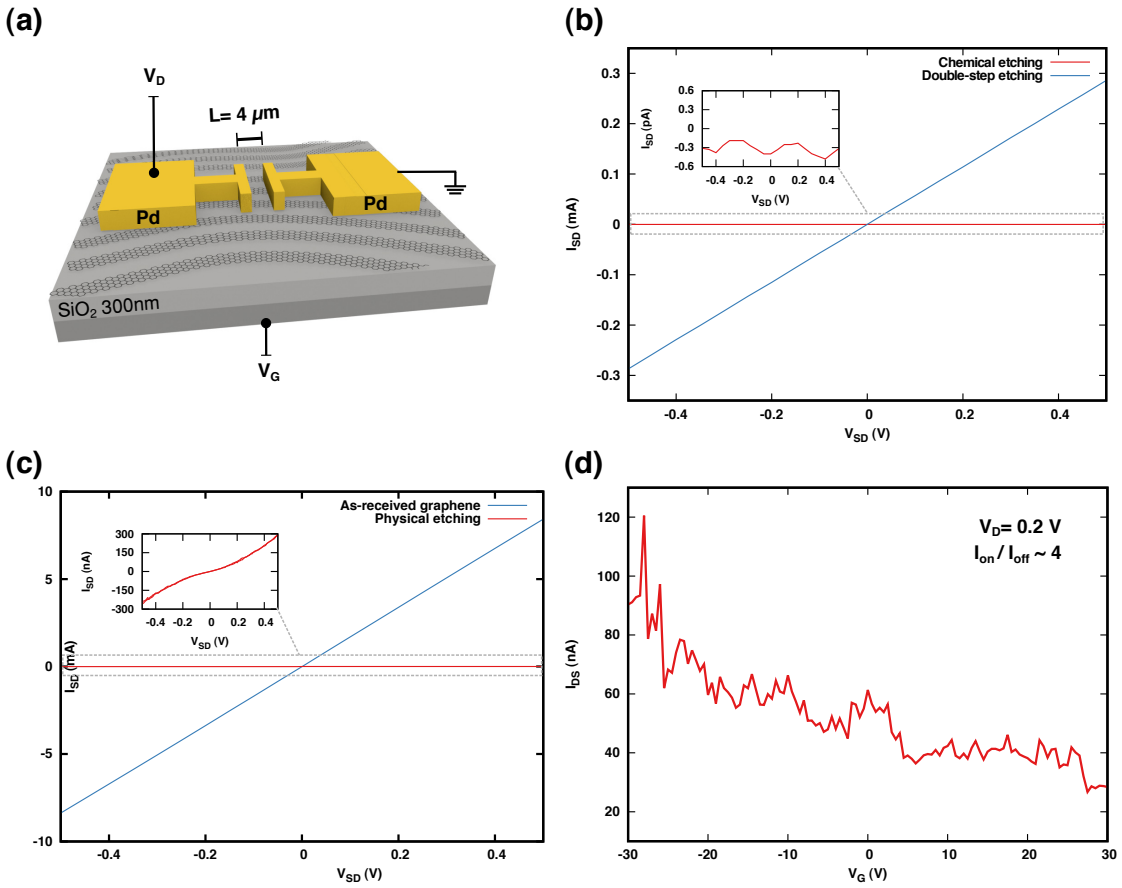

Figure 6.6.: Electrical characteristics with Pd contacts by photolithography. (a) Schematic representation of the back-gated FET: 100-nm thick contacts separated of 4μm. Representative current-voltage (I-V) characteristics at $V_G = 0$ V of the patterned graphene by (b) chemical (inset) and double-step etching, (c) physical etching (inset) and as-received graphene for comparison. (d) Transfer curve at $V_{DS} = 0.2$ V, of the patterned graphene by the physical etching. Calculated I_{on}/I_{off} was ~ 4.

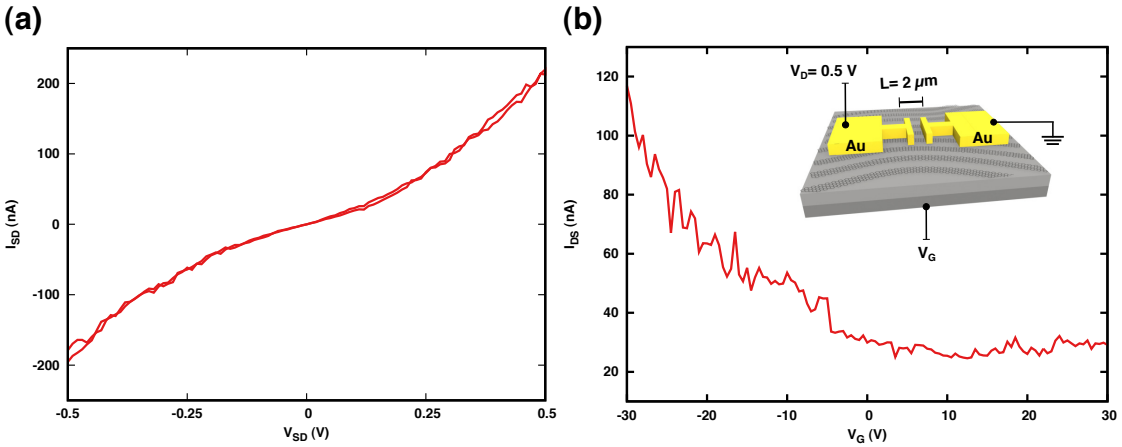

Figure 6.7.: Electrical characteristics with Au contacts by the photolithography transfer pattern method. (a) Representative current-voltage (I-V) characteristics at $V_G = 0$ V of the GNRs. (b) Transfer curve at $V_{DS} = 0.5$ V, of the GNRs. Calculated I_{on}/I_{off} was ~ 3.4.

Using the samples fabricated by the procedure showed in Fig. 6.1, electrical tests of the GNRs were performed using the PTP method of contacts deposition. Fig. 6.7a shows a representative current-voltage (I-V) characteristics of the GNR-FET, measured at $V_G = 0$ V. As observed in Fig. 6.6c, a nonlinear IV relationship indicates a semiconductor behavior, as it is expected. I_{SD} measured at $V_{SD} = 0.5V$ was in the same order of magnitude than that measured in Fig. 6.6c ($\sim$ 500 nA). The corresponding transfer curve is showed in Fig. 6.7b, where the I_{on}/I_{off} was measured to ~ 3.7. The device design allowing this electrical characteristics is a 100-nm thick Au contacts with length and width channel dimensions of 2μm and 30μm respectively.

Characteristics

The capacitance of the GNRs on silicon dioxide must be known in order to calculate many other important parameters such as mobility. Many studies in the literature use the classical oxide capacitance equation given by [21],

$$C_{ox} = \frac{\varepsilon_{ox}\varepsilon_0}{t_{ox}} : \frac{F}{m^2} \tag{6.2}$$

where $\varepsilon_{ox} = 3.9$ for the silicon dioxide, $\varepsilon_0 = 8.89x10^{-12}$ F/m is the vacuum permittiv-

ity and t_{ox} the oxide thickness. Nevertheless, taking into consideration the narrow GNRs width dimensions, the edge effect on the GNRs on the capacitance must be considered. Shylau *et al.* developed a more accurate model to calculate the capacitance of GNRs per unit length [22],

$$C_{ox} = \pi\varepsilon_{ox}\varepsilon_0 w[2d(\arctan\frac{w}{4d}) + \frac{w}{4}\ln\{1 + (\frac{4d}{w})^2\}]^{-1} : \frac{F}{m^2} \tag{6.3}$$

Using eq. 6.2, with $d = 300$nm and $w = 11$nm, it results $C_{ox} = 3.78$ pF/m. This value agrees very well with the simulation model based on finite element analysis reported previously [23]. More rigorous capacitance values demand the consideration of a quantum capacitance [24], nevertheless it goes beyond the objectives of this study.

For the estimation of the career mobility μ in the GNRs [25], a first order approximation is consider, by the relation

$$\mu = \frac{dI_{DS}}{V_G}\frac{L_{eff}}{NC_{ox}V_{DS}} \tag{6.4}$$

with $\frac{dI_{DS}}{V_G} = g_m$, the transconductance, obtained by the slope value after linearization of the characteristic curve (Figs. 6.6d & 6.7b). L_{eff} is the effective channel length, N is the number of GNRs connecting drain and source where and V_{DS} is the source-drain voltage. This simplified equation comes from a basic career mobility model without any resistance consideration and it was assumed that the GNRs join both electrodes from drain to source to compute N, *i.e.*, $N = w/L_0$.

While the GNRs were not aligned unidirectionally from the source to the drain electrodes, the real channel length, i.e. the length of the GNRs connecting source and drain electrodes, is not same as the distance between source and drain electrodes. So, a correction factor k needs to be considered in eq. 6.4 to calculate the career mobility in the GNRs. To simply solve this problem, it is assumed that the lengths of the GNRs are equal and the variations in lengths are compensated by the correction factor with respect to the gap between the source and drain electrodes. From MEB observations it was found that GNRs deviates from 1.2 to 1.5 times the standard channel length. As the shortest GNR path heads for the FET characteristic values, it was estimated $L_{eff} = k.L$ with k the total correction factor equals to $k \sim 1.22$.

If any bandgap between the valence and conduction bands is opened up in graphene, by definition, this discontinuity exactly compensates the metal-graphene Schottky barrier [26]. The off current I_{off} exponential scales as $\exp(-q\phi_{barrier}/k_BT)$, then the bandgap opening value E_g, induced by the patterning of the graphene can be calculated from the analogous Arrhenius equation [27],

$$\frac{I_{on}}{I_{off}} = e^{(\frac{E_g}{k_BT})} \tag{6.5}$$

where I_{on} and I_{off} are respectively the maximum measured and the minimum current measured in the transcharacteristics curve, q is the electron charge, $\phi_{barrier}$ is the Schottky barrier height, E_g is the energy gap in eV, k_B is Boltzmann constant and T is temperature at which the experiment was performed. This method easily links electrical properties with the intrinsic material property E_g. Then, from Figs. 6.6d and 6.7b the energy bandgap opened up in graphene by structuration was calculated.

Table 6.1 resumes the average values from the electrical characterization measurements. Additional average values using a 3μm channel lenght with the PTP method are included. Bandgap values were calculated using eq. 6.5. Regarding the mobility values, they were computed, for comparison, using both the oxide capacitance from eqs. 6.2 and 6.3 in parenthesis.

Table 6.1.: Experimental average values of the electrical characterizations of GNRs.

Contact deposition	**L x W (μm^2)**	**Measurements**		
		I_{on}/I_{off}	**E$_g$ (meV)**	**Mobility (cm^2 Vs^{-1})**
Transfer	2 x 30	3 ± 0.7	28.2 ± 6	141.9 (43.7)
Transfer	3 x 30	2 ± 0.3	17.8 ± 4	83.1 (25.6)
Photolithography	4 x 15	3.7 ± 0.3	33.6 ± 2	157.7 (48.5)

The bandgap values E_g exhibited in table 6.1 fluctuate from ~ 17.8 to ~ 33.6 meV, as the I_{on}/I_{off} ratio approximately fluctuates from 2 to 4. A decrease in the mean on-to-off ratio value for the channel length $L = 3\mu$m was noticed with respected to $L = 2\mu$m. Best values in E_g were found with $L = 4\mu$m, where the metallic contacts were deposited by photolithography. Pd contacts have a lower metal-graphene junction resistance than Au, which may explain differences in the I_{on}/I_{off} trend [10]. These I_{on}/I_{off} values are

even comparable with the literature, in the case where long carrier paths were measured at RT, around 10μm with a on-to-off of 5-10 [23]. Due to differences in the experimental conditions between the two contact deposition methods, it is not possible to evaluate a direct influence on the electrical properties coming from the direct spin-coating of the photolithography resist that could contaminate GNRs after the cleaning with H_2 plasmas.

In chapter 3, the empirical law used to link the bandgap opening and the GNR width was shown. This formula uses both the E_g values showed in table 6.1, GNRs width w estimated by AFM and Raman spectroscopy (11 $\pm$ 1 nm), and it is resumed in the simple relation:

$$\alpha = E_g \cdot w \tag{6.6}$$

where w is GNR average width in ÅAngström and E_g is the energy gap in electronvolts. Further numerical models place α in the range from 0.3 to 3 [18, 28, 29]. From table 6.1, experimental α values are in the range from 0.8 to 2.5.

As the empirical α value falls in this range, it is a qualitative electrical proof of the presence of GNRs, and that conduction is lead by these nanostructures. This method may seem trivial, but is very useful to demonstrate the quality of the GNRs fabricated, as higher α values concedes larger E_g values. A preliminary extrapolation suggests $w \sim 7$ nm to reach functional FET at $E_g \sim 0.4eV$, keeping constant the same α value. Nevertheless, as the α value is extremely sensitive to the nature of edges, crystallographic orientation of the GNR and the bonded functional groups [29], experimental value of α risks to be irreproducible.

The same trend is observed for the mobility values, as it falls down from 141.9 to 83.1 $cm^2/(V\cdot s)$ with an increased channel length from 2μm to 3μm, which was unexpected according to eq. 6.4. Better mobility values were found for the channel lenght $L = 4\mu$m corresponding to 157.7 $cm^2/(V\cdot s)$. They are comparable to the CNTs (150 $cm^2/(V\cdot s)$ [30]) or the polycrystalline Si (100 $cm^2/(V\cdot s)$) but far of the crystalline Si (1400 $cm^2/(V\cdot s)$) or even pristine CVD graphene on SiO_2 (3760 $cm^2/(V\cdot s)$ [31]). Mobility values in parenthesis, usually lower, correspond to the corrected values when the edges effects are considered in C_{ox} (eq. 6.3), that shows again the crucial role of the edges for determining in the optoelectronic properties of the GNRs. This phenomenon raises

questions about the scattering mechanism of the electrons in the GNRs at RT for long mean free paths ($\lambda_{MFP} > 1\mu$m) [32].

Table 6.2.: Contribution to the patterning of graphene by PS-PDMS BCP lithography.

Width (nm)	**Carrer mobility ($cm^2/(V\cdot s)$)**	**Bandgap (meV)**	I_{on}/I_{off}	**Dimension (lxw μm^2)**	**Reference**
8	7.3		95	0.1x0.05	[33]
8	287		13	10x5	[23]
9	120		5	2.4x1.4	[14]
11	48.5	36	4	4x15	

Electrical characterization was initially used as a qualitative tool in the demonstration of the patterning of graphene by the PS-PDMS BCP lithography. Moreover, it was showed that the fabricated device had characteristics comparable to most of literature GNR-based devices, which gives a good reason to confirm the quantitave description made. Table 6.2 compares best characteristics from this work, with the GNRs fabrication studies using the PS-PDMS BCP. Besides, the impact of the disorientated GNRs on electric performances could be definitely improved, as irregular paths and lateral roughness are corrected. Indeed, they may be responsible for the random charge localization at the edges, explaining the low switching capability observed. This is added to the bulk effects, including substrate imperfections and graphene multilayers existence which undoubtedly adversely affects apart edge defects like unwanted molecules bound to the carbon at borders and edge reconfigurations [34, 35].

6.4. Summary

After the definition of a fabrication procedure for GNRs arrays on SiO_2 by high-χ BCP lithography in the 10nm-width regime, patterned graphene was characterized on large surfaces using a Raman mapping tool. By the Cançado relation, the analyzed area (100 μm^2) was covered by a GNR matrix with channels widths of 11 $\pm$ 1 nm. It matches perfectly with the mean width already found by AFM profiles (fig. 5.10). Contact deposition was achieved by contact photolithography and a innovative photolithography pattern transfer method to avoid direct photoresist deposition on the GNRs, for electrical characterization of the fabricated structures. The highly nonlinear I-V relationship, indicated the emergence of a semiconductor behavior (or band gap widening) by the lateral confinement effect through the GNRs. The best I_{on}/I_{off} was $\sim$ 4 for a 4 μm

drain-source separation, which is comparable to some measurements in literature at RT and pressure. Cleaned GNRs fabricated here are expected then to show better conductance characteristics, with a direct self-assembled PS-*b*-PDMS and within lower drain-source separations to avoid career scattering and improve the lateral confinement.

Bibliography

[1] S. Dutta and S. K. Pati, Journal of Materials Chemistry **20**, 8207 (2010).

[2] S. S. Datta, D. R. Strachan, S. M. Khamis, and A. T. C. Johnson, Nano Letters **8**, 1912 (2008), arXiv:0806.3965 .

[3] Y. Li, L. Huang, M. Zhong, Z. Wei, and J. Li, Advanced Materials Technologies **1**, 1600001 (2016).

[4] S. Ryu, J. Maultzsch, M. Y. Han, P. Kim, and L. E. Brus, ACS Nano **5**, 4123 (2011).

[5] Z. Geng, B. Hähnlein, R. Granzner, M. Auge, A. A. Lebedev, V. Y. Davydov, M. Kittler, J. Pezoldt, and F. Schwierz, Annalen der Physik , 1700033 (2017).

[6] M. M. Lucchese, F. Stavale, E. H. M. Ferreira, C. Vilani, M. V. O. Moutinho, R. B. Capaz, C. a. Achete, and A. Jorio, Carbon **48**, 1592 (2010).

[7] L. G. Cançado, A. Jorio, E. H. M. Ferreira, F. Stavale, C. A. Achete, R. B. Capaz, M. V. O. Moutinho, A. Lombardo, T. S. Kulmala, and A. C. Ferrari, Nano letters **11**, 3190 (2011).

[8] D. Bischoff, J. Güttinger, S. Dröscher, T. Ihn, K. Ensslin, and C. Stampfer, Journal of Applied Physics **109**, 073710 (2011).

[9] Y. Zheng, H. Wang, S. Hou, and D. Xia, Advanced Materials Technologies **2**, 1600237 (2017).

[10] F. Xia, V. Perebeinos, Y.-m. Lin, Y. Wu, and P. Avouris, Nature Nanotechnology **6**, 179 (2011).

[11] W. S. Leong, H. Gong, and J. T. L. Thong, (2013), 10.1021/nn405834b, arXiv:1311.1944 .

[12] S. M. Song, J. K. Park, O. J. Sul, and B. J. Cho, Nano Letters **12**, 3887 (2012).

[13] S. Guo, M. Ghazinejad, X. Qin, H. Sun, W. Wang, F. Zaera, M. Ozkan, and C. S. Ozkan, Small (Weinheim an der Bergstrasse, Germany) **8**, 1073 (2012).

[14] J. G. Son, M. Son, K.-J. Moon, B. H. Lee, J.-M. Myoung, M. S. Strano, M.-H. Ham, and C. A. Ross, Advanced Materials **25**, 4723 (2013).

[15] A. Celis, M. N. Nair, A. Taleb-Ibrahimi, E. H. Conrad, C. Berger, W. A. de Heer, and A. Tejeda, Journal of Physics D: Applied Physics **49**, 143001 (2016).

[16] C. Stampfer, J. Güttinger, S. Hellmüller, F. Molitor, K. Ensslin, and T. Ihn, Physical Review Letters **102**, 056403 (2009).

[17] Z. Chen, Y.-M. Lin, M. J. Rooks, and P. Avouris, Physica E: Low-dimensional Systems and Nanostructures **40**, 228 (2007).

[18] Y.-W. Son, M. L. Cohen, and S. G. Louie, Physical Review Letters **97**, 216803 (2006).

[19] M. Poljak and T. Suligoj, IEEE Transactions on Electron Devices **63**, 537 (2016).

[20] Q. Yan, B. Huang, J. Yu, F. Zheng, J. Zang, J. Wu, B.-L. Gu, F. Liu, and W. Duan, Nano letters **7**, 1469 (2007).

[21] A. Kazemi, X. He, S. Alaie, J. Ghasemi, N. M. Dawson, F. Cavallo, T. G. Habteyes, S. R. J. Brueck, and S. Krishna, Scientific reports **5**, 11463 (2015).

[22] A. A. Shylau, J. W. Kłos, and I. V. Zozoulenko, Physical Review B **80**, 205402 (2009).

[23] X. Liang and S. Wi, ACS nano **6**, 9700 (2012).

[24] C. Nanmeni Bondja, Z. Geng, R. Granzner, J. Pezoldt, and F. Schwierz, Electronics **5**, 3 (2016).

[25] G. Rosaz, *Intégration 3D de nanofils Si-SiGe pour la réalisation de transistors verticaux 3D à canal nanofil*, Ph.D. thesis, Université de Grenoble.

[26] R. S. Muller and T. I. Kaminsv, *Device Electronics for Integrated Circuits* (John Wiley & Sons).

[27] F. Xia, D. B. Farmer, Y.-m. Lin, and P. Avouris, Nano Letters **10**, 715 (2010).

[28] L. Yang, C. H. Park, Y. W. Son, M. L. Cohen, and S. G. Louie, Physical Review Letters **99**, 6 (2007), arXiv:0706.1589 .

[29] V. Barone, O. Hod, and G. E. Scuseria, Nano letters **6**, 2748 (2006).

[30] E. S. Snow, P. M. Campbell, M. G. Ancona, and J. P. Novak, Applied Physics Letters **86**, 033105 (2005).

[31] T. J. Lyon, J. Sichau, A. Dorn, A. Centeno, A. Pesquera, A. Zurutuza, and R. H. Blick, Physical Review Letters **119**, 066802 (2017).

[32] X. Wang, Y. Ouyang, X. Li, H. Wang, J. Guo, and H. Dai, Physical Review Letters **100**, 206803 (2008), arXiv:0803.3464 .

[33] S.-J. Jeong, S. Jo, J. Lee, K. Yang, H. Lee, C.-S. Lee, H. Park, and S. Park, Nano Letters , acs.nanolett.6b01542 (2016).

[34] M. Koch, F. Ample, C. Joachim, and L. Grill, Nature Nanotechnology **7**, 713 (2012).

[35] D. Bischoff, P. Simonet, A. Varlet, H. C. Overweg, M. Eich, T. Ihn, and K. Ensslin, physica status solidi (RRL) - Rapid Research Letters **10**, 68 (2016).

7. Conclusion and outlook

Conventional photolithography has been for a while the key technique for patterning in microelectronics. However, due to integrated circuits process requirements for features sizes below 50 nm, the achievable photolithography resolution encounters some physical limitations. Alternative nanopatterning techniques are at the heart of the technological research in order to keep the downsizing of the well-known Moore's law.

BCPs have the particular property to self-assemble into ordered periodical structures. These macromolecules, in association with standard photolithography, represent a promising approach as an alternative advanced patterning technique in microelectronics. This way, the downsizing of ICs can be kept up. BCPs with high chemical incompatibility between their blocks exhibit a high value of the Flory-Huggins interaction parameter χ. The BCP theory predicts periodical features sizes with high-χ BCPs of only few nanometers.

This thesis explored the potential of the high-χ PS-*b*-PDMS self-assembly as a possible candidate to develop a next-generation BCP lithography, versus the current low-χ BCPs, usually PS-*b*-PMMA, which is not capable to attain half-pitch dimensions below 20 nm. Lithography performances of PS-*b*-PDMS thin film masks are demonstrated on Si and graphene substrates. This latter material, having special needs of patterning, was particularly deepened. In order to facilitate the implementation of the PS-*b*-PDMS BCP lithography in industry, a special attention was put in the development of reliable industry-compatible processes.

In chapter 2, the influence of PS-selective plasticizers on the self-assembly process of cylindrical and spherical PS-*b*-PDMS was studied. Block copolymers forms PS-*b*-PDMS micelles in solution with a hydrodynamic diameter D_h commensurable with their natural period length L_0. Physical properties of plasticizers such as negligible vapor pressure and high PS selectivity promote a high lateral motion of chains, and consequently, a significant enhancement of the PS-*b*-PDMS self-assembly kinetics. Well-ordered hexago-

nal spheres could been obtained in a one-step coating process, without any post-coating annealing.

Afterwards, using cylindrical polymers, the evaporation of plasticizer via thermal annealing allows a fast morphological transition from the metastable spherical state to its stable cylindrical morphology. After 30 s of annealing, well-aligned cylinders were obtained. Among the tested plasticizers, DOA resulted in the best compromise between evaporation rate and PS-selectivity. In this way, a practical method to make block copolymer lithography a high throughput process was demonstrated and we illustrate its applicability to fabricate high-resolution structures on large surfaces.

After showing the lithography principle on Si with different PS-*b*-PDMS thin films (70kg/mol and 45.5kg/mol) in chapter 2, with features sizes in the order of 30 and 25 nm respectively, attention was focused on the patterning of new emerging materials. Indeed, chapter 3 gave the main concepts to understand issues of graphene patterning, *i.e.*, narrow structures of graphene need to be created for bandgap opening in graphene by lateral confinement (< 10nm) of the Dirac electrons which generates a transition to semiconductor from its intrinsic semi-metal behavior. Then, GNR could be envisaged as FET channels in IC.

In this context, the patterning with high-χ PS-*b*-PDMS responds to the demand for ultra-high-resolution patterning of graphene. Few studies have been led on GNRs fabrication using high-χ BCP and more studies are needed to raise several unanswered questions. From a nanofabrication point of view, GNRs should ideally be fabricated on large areas with CMOS-compatible processes at a sub-10 nm resolution with a controlled chemical quality and edge structure.

So as to obtain a sub-10 nm hard mask for graphene patterning, the self-assembly of 10 nm resolution PS-*b*-PDMS was studied in chapter 4. This hard task was investigated within three approaches:

- the use of a underlayer as an intermediate transfer layer
- direct spin-coating and self-assembly on graphene
- the directed self-assembly with a soft graphoepitaxy approach (guiding of the BCP by removable polymer lines)

In the underlayer approach, the idea was to protect the graphene layer during patterning with a material that can be easily cleaned from the graphene surface. Different materials from polymers to high-κ dielectrics were tested. Calculations of the correlation length were implemented in order to quantify the PS-*b*-PDMS self-assembly on the stack BCP/underlayer/graphene. In all cases, a low self-assembly quality was attained (correlation length $\xi \sim 3050$ nm). As the correlation length represents the exponential decay of the correlation function, it is frequently interpreted as the average length of the polymer grains, which is considered insufficient here for any device development.

Better results in the self-assembly were obtained with a direct spin-coating and assembly on graphene. A thermal pre-annealing step of the graphene layer at 170 °C under vacuum was implemented before self-assembly. It is shown by contact angle and Raman spectroscopy measurements that this pre-annealing step modifies the chemical affinity of the CVD graphene without introducing an important amount of disorder in the graphene structure.

In spite of self-assembly improvement, a PDMS wetting layer is still present at the BCP/graphene interface, which is detrimental for etching experiments. It is shown by the Good and Girifalco surface energy model that, by heating CVD graphene at higher temperatures, it is likely to favor the PS wetting by an enhanced surface energy modification of graphene. Experimental results obtained by SEM and STEM observations proved this statement. Finally, at the same time, a desired morphology of the PS-*b*-PDMS thin film was obtained (PS wetting on graphene) and improvement self-assembly quality ($\xi \sim 300$ nm).

For the directed self-assembly of PS-*b*-PDMS, a soft-graphoepitaxy process on graphene was developed using a lift-off resist in order to create removable guiding lines. Nevertheless, high line roughness on guiding lines affected the directed self-assembly of the PDMS cylinders. Moreover, a likely high affinity of the PDMS with the guiding resist orientated the self-assembled PDMS cylinders perpendicularly, resulting in inadequate results through this approach. In the following, the PS-*b*-PDMS lithography mask developed by the direct spin-coating approach was used in the study of graphene patterning by plasma etching.

In chapter 5, the patterning of graphene through BCP lithography was studied. The understanding of plasma etching allowed the patterning of graphene with a BCP mask taking account the selectivity of the mask and the etching rate. Physical type etching

avoids a lateral etching of graphene during transfer *versus* the chemical type etching which seems to etch the underneath graphene is demonstrated in further electrical characterization.

Analysis of the graphene structuration was supported by usual carbon characterization techniques. Raman is as a practical tool with a graphene footprint in the characteristics G and 2D peaks. The appearance of the D peak was a key element as it is interpreted as edges defects of the graphene ribbons. AFM allowed to determine dimensions of GNRs, where the center of the Gaussian distribution of height and width where located at ~ 5 Å and ~ 11 nm.

The question about the chemical quality and cleanliness of the GNRs was raised during this thesis. For this GNRs were cleaned after mask stripping with hydrogen plasmas. Indeed, polymer materials are used both for the transfer of CVD graphene to SiO_2 substrates (PMMA) and for graphene pattering (PS-*b*-PDMS) and these represent an important source of amorphous carbon contamination. Moreover, the etching of graphene with oxygen-based plasma generates recombination at the edges which *p*-dopes the graphene structures. XPS measurements showed the efficient removal of the carboxyl, C-O and amorphous carbon species. XPS quantification determined also the reduction of the sp^2 carbon which approximately matches with the expected graphene removal amount after patterning with the PS-*b*-PDMS lithography mask. Hydrogen plasmas presented here showed an efficient and smooth way to clean and tailor GNRs. The complementarity of the carbon analysis techniques used allowed to prove the patterning of graphene, meanwhile electrical characterizations where performed in order to confirm this statement.

Fabricated GNRs arrays on SiO_2 were then further characterized on large surfaces using a Raman mapping tool. The Cançado relation allowed to calculate the defects length L_D, which is interpreted as the GNRs width. It was found that the analyzed area ($100\ \mu m^2$) was covered by a GNR matrix with channels widths of 11 ± 1 nm. It matches perfectly with the mean width found by AFM profiles.

Finally, metallic contact deposition was achieved by contact photolithography and an innovative photolithography pattern transfer method (to avoid direct photoresist deposition on the GNRs) for an electrical characterization of the fabricated structures. In both methods of contact deposition, a highly nonlinear I-V relationship was measured, indicating the emergence of a semiconductor behavior (or band gap opening) by the

lateral confinement effect in the GNRs. The best on-off ratio measured was ~ 3.7 for a 2 μm drain-source separation, which is comparable to some measurements in the literature at room temperature and pressure. Cleaned GNRs fabricated here would certainly show improved conductance characteristics within a shorter drain-source separation device, avoiding career scattering and improve lateral confinement.

Future works

Future works on the study of the PS-*b*-PDMS self-assembly includes a more detailed understanding of the plasticizer mechanism on the self-assembly, this notoriously for a possible generalization of the use of plasticizers in other high-χ BCPs systems which are technologically interesting to fabricate sub-10nm structures. Additionally, a better understanding of this mechanism could overcome/improve the problem of defects, which is an important issue is directed self-assembly. The works on plasticizers were highly innovative in a context where the thermal self-assembly kinetics of high-χ BCPs are incompatible with the high throughput demanded by the semiconductor industry. At the same time, these results are promising as well for other fields needing resolute structures on large surfaces such as solar panels, photocathodes or bit patterned media.

On the graphene side, fabricated structures are actually subject to an atomic resolution characterization via low-voltage TEM observations. The key role of the edges in the GNRs properties requires a precise control of the edges (orientation, roughness and doping). This has to be characterized and controlled. For this, efforts must be focused on the plasma technology which is the most adapted technology to laterally smooth and or functionalize graphene and its related materials at the atomic scale. Indeed, the doping of GNRs in one of the essential future works on GNRs, as the functionalization of the edges may bring new electrical and physical properties.

Field effect transistors characteristics based on GNRs are surely to be optimized by using directional GNRs channels and adapted metallic electrodes to generate improved responses (higher I_{on}/I_{off}). The here developed soft-graphoepitaxy could be used to optimize the directed self-assembly (perpendicularly to the trenches then), and deposit contacts. The other possible path is a first deposition of the metallic electrodes, before the BCP spin-coating on graphene.

Beyond microelectronics, GNRs are expected to find a broad ranges of applications in

the field of electrochemical sensors such as high sensitivity chemical or gas sensors due to the strong chemical reactivity of the edges. Another promising field in which GNRs may find applications is in bioanalysis, by the specific recognition of biomolecules such as proteins, enzymes and DNA. These applications do not need directed GNRs array, so the already fabricated structures could be used for these kind of devices.

The lithography procedure developed in this thesis may also be generalized to fabricate different graphene nanostructures such as graphene nanomeshes or quantum dots, to extend the potential applications. PS-*b*-PDMS could be used as a generic lithography mask to generate desire nanostructures: by changing the self-assembly procedure, one could make use of different metastable morphologies (spheres, cylinders, perforated lamellae). Finally, other 2D materials such as monolayer transition metal dichalcogenides, or a combination of them, needs also high resolution patterning methods to exploit or readapt their characteristics such as in thermoelectricity, photonics, optoelectronics and energy applications.

A. Correlation length calculations

Analytical tools are gaining attention in the area of directed self-assembly in order to measure the quality of a BCP pattern [1]. Since then, a toolbox of techniques have been created, capable of analyzing critical features such as the defect density, correlation lengths, Line edge roughness (LER) and Line width roughness (LWR) [2, 3].

The quality of the structure formed from an initial BCP thin film can be quantified beyond a qualitative description. The quantification of order uses the correlation lengths to measure the "grain sizes" defined by the self-assembled structures. Here, the method to calculate the correlation lengths is detailed for a spherical-forming and a cylindrical-forming BCP.

Orientational maps

The first step in the correlation length calculation, is to obtain an orientation map from the raw SEM image, where the grain sizes are delimited, meanwhile the method varies for a sphere network and for lines (horizontal cylinders). Both are obtained as follows.

Orientational map from spheres

For calculating the orientational field from spherical morphologies, the general procedure described by Harrison *at al.* was followed [4, 5]. A Matlab routine was created to implement this procedure.

In the Matlab program 'orientation_field_calculation', a 8-bit grayscale images was used (fig. A.1a), which was inversed to get black discs.

A function named 'comptage_billes' was used, with different arguments which calls

a Matlab function named 'imfindcircles'. This function is able to detect discs in the image and to calculate the centers of these black discs (fig. A.1b). Then, a Delaunay triangulation between these centers is applied (fig. A.1c).

The orientation of each hexagon (mean angle of its 3 main diagonals, value between 0 and $\pi/3$) was calculated. Then, the orientation field was interpolated to plot the orientational map (fig. A.1d).

Orientation_field_calculation.m

```
%% Working directory definition
wd = 'C:\...\';

%% Image Name, it must be a grayscale 8 bit image
IMname = 'image';

%% Image reading
IM = imread([wd,IMname,'.TIF']);

%% Orientation Field Saving
ims = ['Orientation_field_',IMname];

%% Color inversion to get black beads
IM2 = 255-IM;
imwrite(IM2,[wd,IMname,'_INV.TIF']);

%% CIRCLES CENTER DETECTION
%% Function calling "comptage_billes", use 'imfindcircles';
nom_im = [IMname,'_INV.TIF'];
gamma = 1;
method = 'PhaseCode'; %% COMPUTATION METHOD
dmin = 2; %% MINIMUM DIAMETER OF THE DETECTED CIRCLES
dmax = 4; %% MAXIMUM DIAMETER OF THE DETECTED CIRCLES
sens = 0.99; %% SENSITIVITY OF THE
```

```
edth = 0.05; %% EDGE GRADIENT THRESHOLD

%% Center calculation with 'comptage_billes'
centers = comptage_billes(wd,nom_im,dmin,dmax,sens,gamma,
   method,edth);

%% DELAUNAY TRIANGULATION
DT = delaunayTriangulation(centers);
figure();
imshow(IM);
hold on
triplot(DT);

%% List of triangles
DTC = DT.ConnectivityList;

%% HEXAGONS ORIENTATION CALCULATION
%% Results are in 'POINT' variable defining center,
   coordinates and main angle of hexagones
POINT = nan(length(DT.Points),4);
POINT(:,1) = 1:length(DT.Points);
POINT(:,2:3) = DT.Points;

%% Regularity of hexagons
OCTR = zeros(1,length(DT.Points));

%% ORIENTATION CALCULATION
for itr = 1:length(DT.Points) %% Hexagon loop
    IDtri = vertcat(find(DTC(:,1)==itr),find(DTC(:,2)==itr),
       find(DTC(:,3)==itr));
    if (length(IDtri) == 6) %% Hexagon test
        Coor0 = DT.Points(itr,:);
        IDpoint = DTC(IDtri(1),:);
        for j = 2:6
           IDpoint = horzcat(IDpoint,DTC(IDtri(j),:));
        end
```

```
IDpoint = unique(IDpoint);
IDpoint = IDpoint(find(IDpoint ~= itr)); %% ID
if length(IDpoint)==6

    %%% angle calculation
    theta = zeros(2,6);
    theta(1,:) = IDpoint(1,:);
    for itheta = 1:6
        X = DT.Points(IDpoint(itheta),:)-Coor0;
        Y = X(1)+i*X(2);
        theta(2,itheta) = angle(Y);
    end

    %% Angles sorting
    theta = transpose(theta);
    theta = sortrows(theta,2); %% Angles from -Pi TO
        Pi

    %% Excluding irregular hexagons
    mint = 2*pi+theta(1,2)-theta(6,2);
    for ih = 1:5
       mint = min(mint, theta(ih+1,2)-theta(ih,2));
    end
    if mint > 0.5 %% angle calculation only if
       regular hexagon
        OCTR(itr) = 1;

        %% vertex coordinates of hexagon
        X = POINT(IDpoint(1),2);
        Y = POINT(IDpoint(1),3);
        for ii = 2:6
            X = horzcat(X,POINT(IDpoint(ii),2));
            Y = horzcat(Y,POINT(IDpoint(ii),3));
        end

          %% angles of the 3 main diagonals of the
```

```
                    hexagon
                VECT = [POINT(theta(4,1),2)-POINT(theta
                    (1,1),2),POINT(theta(4,1),3)-POINT(
                    theta(1,1),3)];
                V1 = VECT(1)+i*VECT(2);
                VECT = [POINT(theta(5,1),2)-POINT(theta
                    (2,1),2),POINT(theta(5,1),3)-POINT(
                    theta(2,1),3)];
                V2 = VECT(1)+i*VECT(2);
                VECT = [POINT(theta(6,1),2)-POINT(theta
                    (3,1),2),POINT(theta(6,1),3)-POINT(
                    theta(3,1),3)];
                V3 = VECT(1)+i*VECT(2);
                b1 = angle(V1);
                b2 = angle(V2);
                b3 = angle(V3);
                b = [b1,b2,b3];

                %% angle between 0 and 2Pi
                if b3 < 0
                    b3 = 2*pi+b3 ;
                end

                %% mean angle
                POINT(itr,4) = mod(mean([b1,b2-pi/3,b3-2*
                    pi/3]),pi/3);
                POINT(itr,4) = pi/3-POINT(itr,4);
            end
        end
    end
end

%% ORIENTATION FIELD PLOT
%% x, y, z coordinates
X=POINT(:,2);
Y=POINT(:,3);
```

```
Z=POINT(:,4);

%% uniform grid
idxgood=~(isnan(X) | isnan(Y) | isnan(Z));
[xx,yy] = meshgrid(1:size(IM,2),1:size(IM,1));

%% nearest neighbor interpolation
CI = griddata( X(idxgood),Y(idxgood),Z(idxgood), xx, yy , '
   nearest') ;

%% plot
iptsetpref('ImshowBorder','loose');
figure()
imshow(CI,[],'Colormap',hsv(256));
hcb=colorbar;
caxis([0 pi/3]);
set(hcb,'YTick',[0 pi/12 2*pi/12, 3*pi/12, 4*pi/12])
set(hcb,'YTickLabels',{'0','Pi/12','Pi/6','Pi/4','Pi/3'})
title(hcb,'Angle')
set(gca, 'YDir', 'reverse')
xlim([0 size(IM,2)])
ylim([0 size(IM,1)])
print([wd,ims],'-dpng');

%% plot without border
iptsetpref('ImshowBorder','tight');
figure, imshow(CI,[],'Colormap',hsv(256));
print([wd,ims,'_noborder'],'-dpng');
```

Orientational map from horizontal cylinders

The ImageJ plug-in OrientationJ was used for directional analysis in cylinder-forming BCP networks. This plug-in is based on the evaluation of the structure tensor in a local

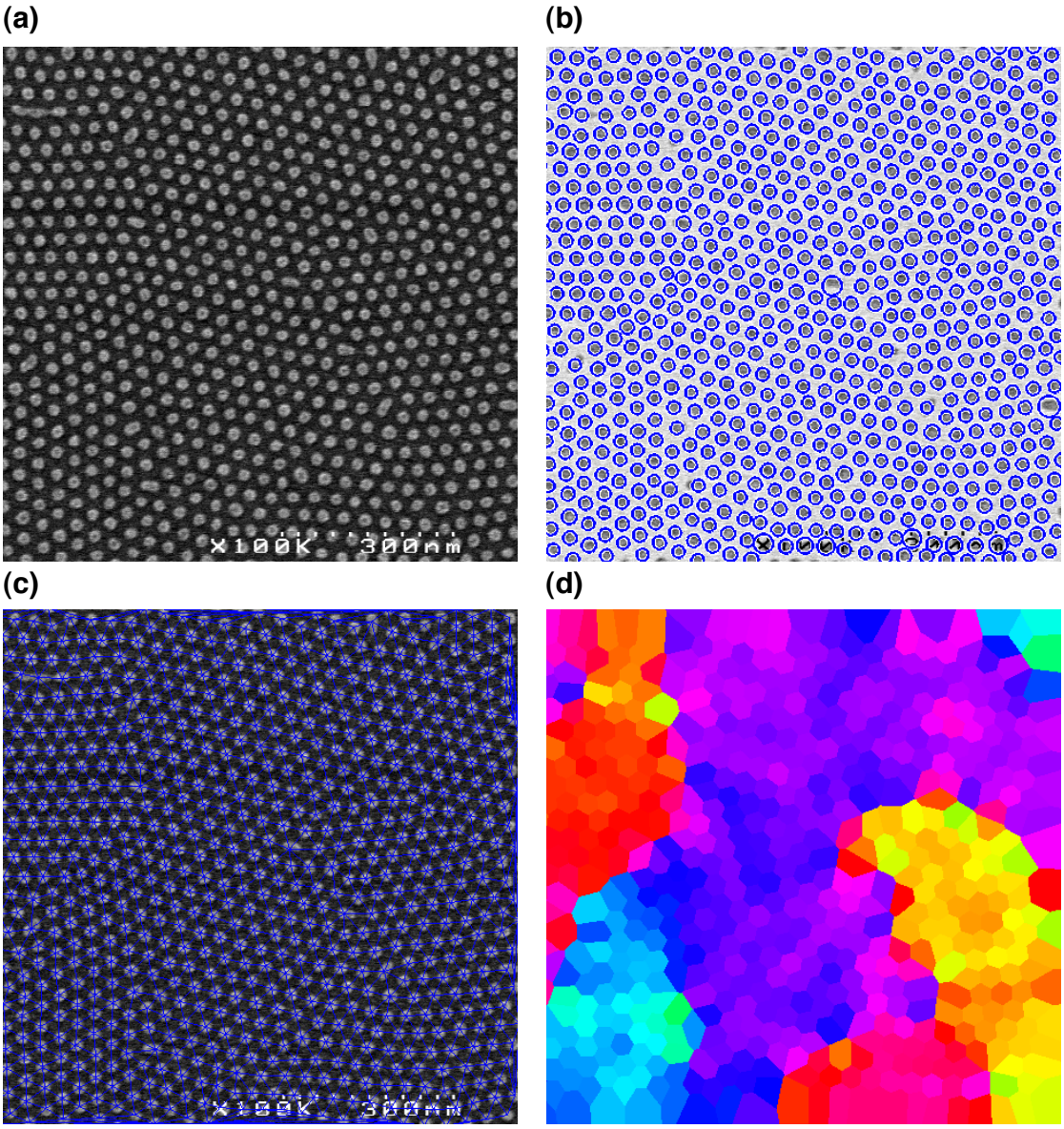

Figure A.1.: Analysis of a spherical block copolymer thin film: (a) Raw image of the spherical-forming block copolymer. (b) Inversed image to calculate the center of every sphere. (c) Delaunay triangulation of the spherical network. (d) Color map of the lattice orientation.

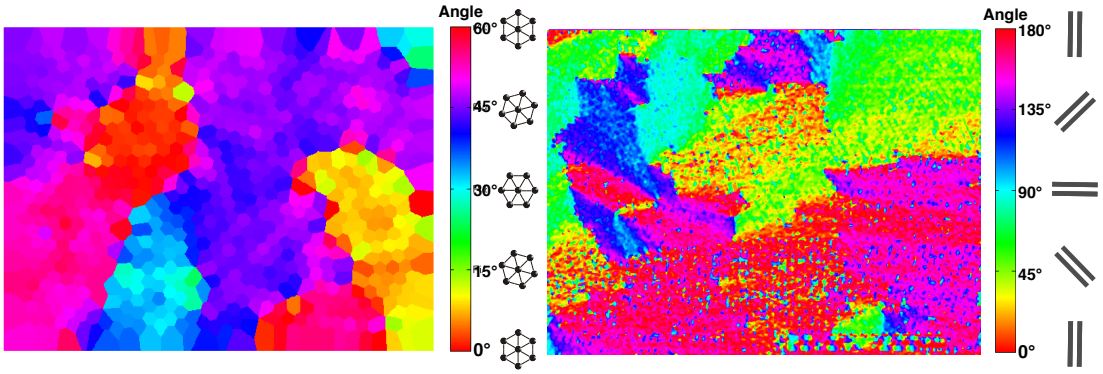

Figure A.2.: Orientational maps from different morphologies: (top) from a spherical-forming block copolymer, the colors of the spectrum indicate a range from 0 to 60 °. (bottom) from a cylindrical-forming block copolymer where the orientation colors indicate a range from 0 to 180 °.

neighborhood to characterize the orientation properties of a region of interest in a SEM image. A full theoretical background description is given by Püspöki *et al.* [6].

The "visual representation of the orientation" OrientationJ functionality was used to obtained the orientational field. The image analysis was launched by selecting a color survey with orientation hue, coherency saturation and Original-Image brightness, which automatically displays the orientational map plot.

Orientation correlation function

To evaluate the degree of ordering in the system, the orientational correlation function $g(r,t)$ is calculated. From the set of orientation angles, the correlation function is defined as

$$g_6(r,t) =< \exp\{6i[\theta(\overrightarrow{r}+\overrightarrow{r}',t)-\theta(\overrightarrow{r}',t)]\} > \tag{A.1}$$

Eq. A.1 applies in a sphere network, where $\theta(\overrightarrow{r})$ is the local hexagon orientation, determined by the real space in the Delaunay triangulation. For simplicity, eq. A.1 could be redefined as [7],

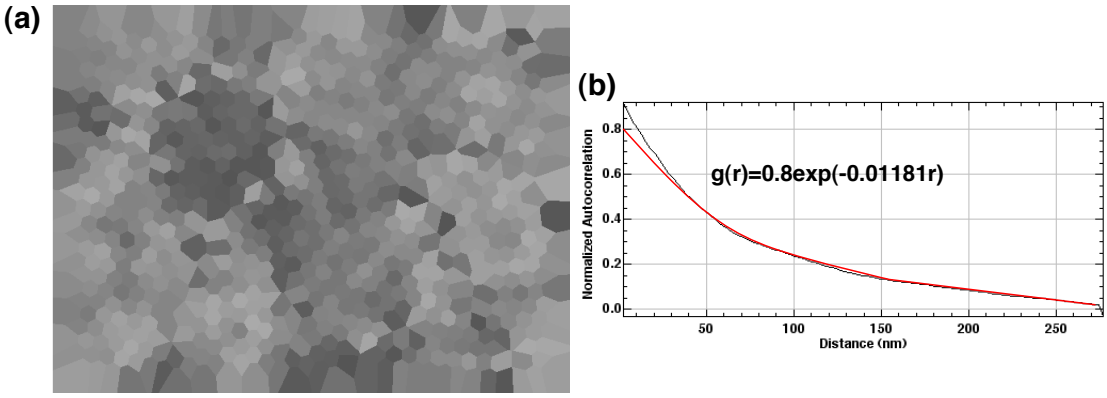

Figure A.3.: Correlation length calculation. (a) 8-bit grayscale image of the orientation map. (b) Plot of the corresponding correlation function, fitted as $\exp(r/\xi)$ to calculate the correlation length ξ.

$$g_6(r) =< \cos[6\theta(r) - \theta(r')] >=< cos(6\delta\theta) > \tag{A.2}$$

or in the case of cylinders [8],

$$g_2(r) =< cos(2\delta\theta) > \tag{A.3}$$

In both cases, the roughly exponential decay of the orientational correlation function allows to fit the correlation function $G(r)$ as,

$$g(r) \sim \exp[-\frac{r}{\xi}] \tag{A.4}$$

The parameter ξ is defined as the orientational correlation length. The average grain size is computed when $g(r)$ decays at $1/e$, i.e. ξ is the distance over which the mean nanoscale morphologies are coherent, aligned along a particular direction [9].

An ImageJ macro was used to calculate the average autocorrelation of a binary orientational map image [10], then the plot was fitted as an exponential curve to obtain the ξ value.

Bibliography

[1] M. Ceresoli, F. G. Volpe, G. Seguini, D. Antonioli, V. Gianotti, K. Sparnacci, M. Laus, and M. Perego, J. Mater. Chem. C **3**, 8618 (2015).

[2] G. Aprile, F. Ferrarese Lupi, M. Fretto, E. Enrico, N. De Leo, L. Boarino, F. G. Volpe, G. Seguini, K. Sparnacci, V. Gianotti, M. Laus, J. Garnaes, and M. Perego, ACS Applied Materials & Interfaces , acsami.7b00509 (2017).

[3] T. Segal-Peretz, J. Winterstein, M. Doxastakis, A. Ramírez-Hernández, M. Biswas, J. Ren, H. S. Suh, S. B. Darling, J. A. Liddle, J. W. Elam, J. J. de Pablo, N. J. Zaluzec, and P. F. Nealey, ACS nano **9**, 5333 (2015).

[4] C. Harrison, D. E. Angelescu, M. Trawick, Z. Cheng, D. A. Huse, P. M. Chaikin, D. A. Vega, J. M. Sebastian, R. A. Register, and D. H. Adamson, Europhysics Letters (EPL) **67**, 800 (2004).

[5] D. A. Vega, C. K. Harrison, D. E. Angelescu, M. L. Trawick, D. A. Huse, P. M. Chaikin, and R. A. Register, Physical Review E **71**, 061803 (2005).

[6] Z. Püspöki, M. Storath, D. Sage, and M. Unser (Springer, Cham, 2016) pp. 69–93.

[7] A. P. Marencic, M. W. Wu, R. A. Register, and P. M. Chaikin, Macromolecules **40**, 7299 (2007).

[8] J. N. Murphy, K. D. Harris, and J. M. Buriak, PLOS ONE **10**, e0133088 (2015).

[9] P. W. Majewski and K. G. Yager, Journal of physics. Condensed matter : an Institute of Physics journal **28**, 403002 (2016).

[10] J. G. Berryman and S. C. Blair, Journal of Applied Physics **60**, 1930 (1986).

B. CVD graphene & analysis

Graphene growth

There are two different approaches to prepare graphene. On the one hand, graphene can be detached from an already existing graphite crystal, the so-called exfoliation methods. On the other hand, the graphene layer can be grown directly on a substrate surface [2]. The first reported preparation of graphene was by exfoliation using a simple adhesive tape.

For large surfaces applications, the graphene growth by chemical vapor deposition (CVD) is privileged, as it allows an uniform growth even on 4-inch wafers. For this, an initial growth substrate is exposed to a gas mixture of H_2, CH_4 and Ar at about 1000 ° C [3]. In the CVD process, *grosso modo*, the CH_4 decomposes on the surface, so that the hydrogen evaporates (fig. B.1). The carbon diffuses into the substrate, usually Cu, which has a mismatch of the lattice constant at about 1.3 % with graphene lattice. After cooling down in an Ar atmosphere, a graphene layer grows on the surface [4].

If the desired working substrate is other than Cu, a transfer step is required in order to separate graphene from the catalyst metal substrate and move it to an arbitrary substrate. Polymer supported transfer methods are being developed along with and specifically for CVD graphene synthesis [5, 6]. PMMA is a widely used polymer carrier for CVD graphene transfer [7]. PMMA is easily spin coated on graphene and moved to any target substrate by etching away Cu in $Fe(NO_3)_3$ or $FeCl_3$.

During this thesis, CVD grown graphene on 4-inch SiO_2 wafers was used. They were directly purchased from Graphenea. The as-received graphene was properly characterized by the main carbon characterization techniques, detailed below.

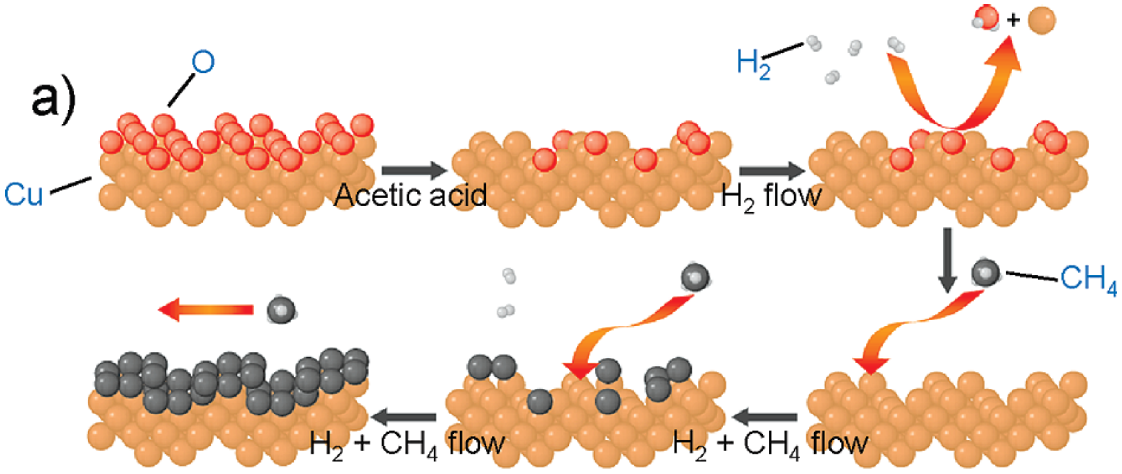

Figure B.1.: Method of graphene synthesis on evaporated copper: substrates are first immersed in acetic acid at 35 ° C for 10 min and then quickly loaded into the reaction chamber. Samples are then exposed to 200 sccm H_2 at $\sim$ 2 Torr while heating. Growths are carried out for 20 min at 1000 ° C under 200 sccm H_2 and 875 sccm CH_4 at $\sim$ 11 Torr. Adapted from [1].

Analysis of carbon

Optical and scanning electron microscopy

Particularly for CVD graphene on a thick SiO_2 substrates > 100nm, it is possible to identify graphene films by simple optical microscope observation. Optical constrast with the SiO_2 substrate allows to distinguish multilayers from graphene monolayers. Fig. B.2a shows an optical image of the as-received CVD graphene from Graphenea. This graphene present the formation of multilayers at the grain boundaries. Consequently, this has an implication on the fingerprint Raman spectra. This is confirmed by SEM observations, showed in fig. B.2b.

X-Ray Photoelectron Spectroscopy

XPS relies on the detection of characteristic photoelectrons emitted from the sample surface upon exposure to X-rays to identify elements and their bonding characteristics and local environment. When X-rays are absorbed by a sample, their energy will contribute to (Fig. B.3a), including to

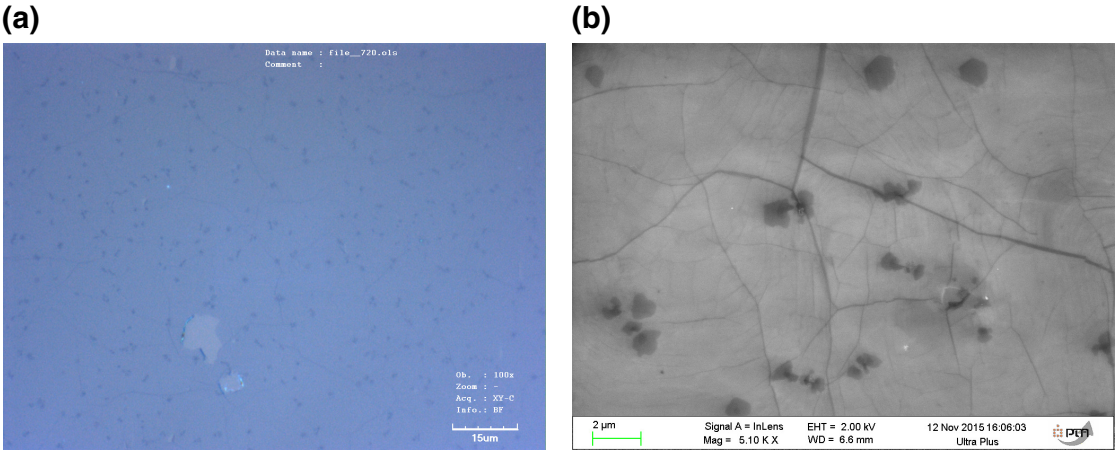

Figure B.2.: Observation of the as-received CVD graphene on 300nm thermal growth SiO_2 from Graphenea. (a) Optical top-view image and (b) SEM top-view image.

1. break the bond between electrons and the atom, also known as the binding energy,

2. provide sufficient kinetic energy to the photoelectrons located nearest to the surface to escape from the surface of the sample, and

3. provide excess kinetic energy to the ejected photoelectrons in vacuum

The main characteristic parameter is the binding energy, which allows to identify elements and their binding environment [8]. The characteristic peak of carbon C 1s appears in the range of 283 eV to 290 eV, and it can be decomposed into several components depending on the structure of carbon and other existing elements (Fig. B.3c). C-C bonds are revealed by three peaks [9]: a peak from sp^2 hybridized atoms appearing at 284.3 ± 0.30 eV and another representing the sp^3 hybridized atoms appears at 285.0 ± 0.40 eV, beside an sp^1 peak that appears at 283 eV.

Peaks from carbon oxygen bonding can appear at higher binding energies than previous peaks, each referring to a different state of bonding. These peaks were identified as C-O appearing around 286.5 eV, C=O appearing around 287.0 eV and carboxylic (O=C-O) group appearing around 289 eV [10], respectively . The C-H peak, observed in hydrogenated graphene samples [11], was reported to appear close to the positions as sp^3 connected carbon atoms C-C ($\sim$ 286 eV). The C-O peak in XPS can refer to either epoxy or hydroxyl groups decorating the basal plane, while C=O indicates ketons and

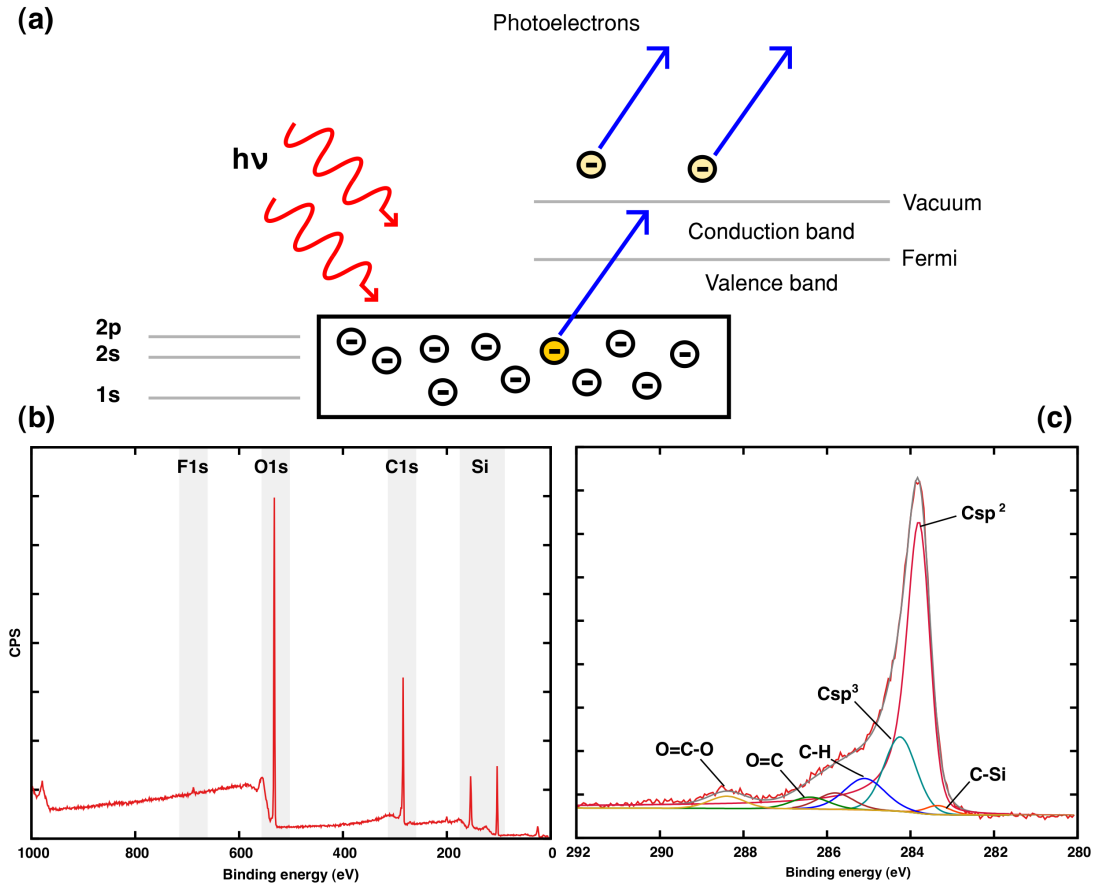

Figure B.3.: X-ray Photoelectron spectroscopy of graphene from Graphenea: (a) Schematic representation of the photoelectric effect, adapted from the CC image [13], (b) element survey and (c) the C1s peak.

quinines at the edges of the sheet or carbonyl groups in the basal plane [12].

Raman Spectroscopy

Raman spectroscopy is the most versatile and common method used to fingerprint carbon [14]. Raman is based on the interaction between photons and molecules, whereby they are irradiated with a monochromatic laser beam that excites molecules, causing them to vibrate and irradiate a photon with a different energy, based on photon-phonon interactions. Upon excitation of the atoms to a higher level, they either return back to their original state in what is known as Rayleigh scattering (elastic), or to a different

energy level with either higher (Stokes) or lower (Anti-stokes) energy than the initial state. The latter two processes are inelastic and are known as Raman scattering (Fig. B.4a).

The two main peaks that defines a graphene spectrum are the so-called G-peak and the D-peak (Fig. B.4b). The G peak, which exhibits a single peak only appearing at 1570 cm^{-1}, results from in-plane stretching of the sp^2 bonded carbon (inset of Fig. B.4b). The position of this peak is sensitive to the structure of graphene and changes according to the level of disorder and can vary between 1565 cm^{-1} and 1600 cm^{-1} [15] .

The D peak centered at 1355 cm^{-1} is caused by the breathing mode of aromatic carbon atoms (inset of Fig. B.4b), which vanishes for graphene and becomes active only when defects or discontinuities in the symmetry of the network exist. The D' peak at $\sim$ 1620 cm^{-1} appears in graphene, and its intensity is correlated to the degree of disorder in the sample similarly to the D peak [15] .

The peak at 2700 cm^{-1} is known as the 2D peak, a second-order overtone of a different in-plane vibration and it becomes more intense with increasing graphene quality, up to I(2D/G) $\sim$ 2 [16]. The 2D peak is especially relevant in studies involving graphene, especially in determining the number of graphene layers. Due to the presence of graphene multilayers uniformly distributed on the whole monolayer graphene, it causes a decrease in the mean I(2D/G) to $\sim$ 1.3 (fig. B.4b).

Atomic Force Microscope

Atomic force microscopy (AFM),in particular, is used extensively since it provides three-dimensional images that enable the measurement of the lateral dimensions of graphene films as well as the thickness, and by extension the number of layers present. However, in the literature, AFM has proven to be inaccurate with a wide range of measured values for single layer graphene thickness (between 0.4 and 1.7 nm). This discrepancy has been attributed to tip-surface interactions, image feedback settings and surface chemistry interaction with the AFM tips [18].

As-received graphene from Graphenea was imaged by an AFM. Fig. B.5 show the top view image by AFM, where it is possible to better distinguish the grain boundaries of graphene crystals, the characteristic wrinkles in CVD graphene and also the multilayers regions, already observed before by optical microscopy.

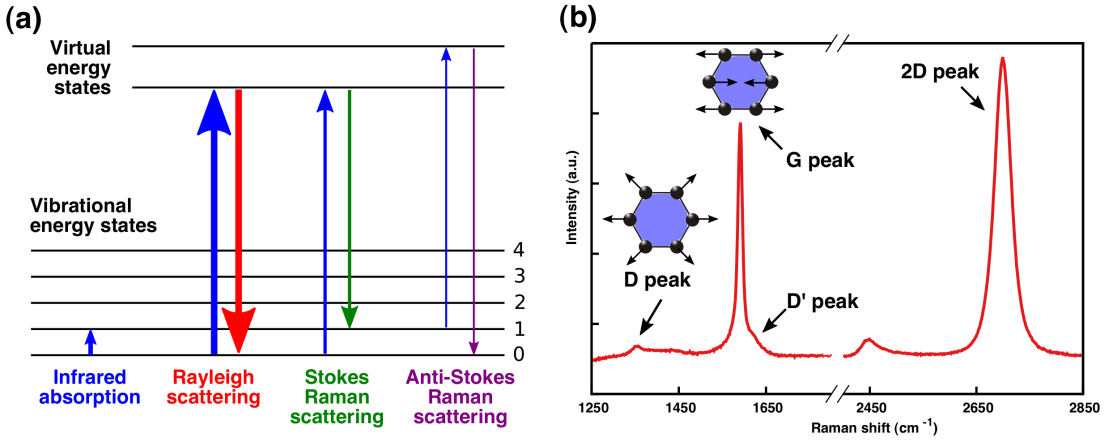

Figure B.4.: Raman spectra of CVD graphene: (a) Energy-level diagram showing the states involved in Raman spectra, image under CC [17]. (b) fingerprint Raman spectra of the CVD graphene from Graphenea. Inset figures schematically represent the vibration mode of carbon atoms, consisting of the stretching mode causing the G peak (right) and the breathing mode causing the D peak (left). Mean intensity peak ratio is evaluated at $I(2D/G) \sim 1.3$.

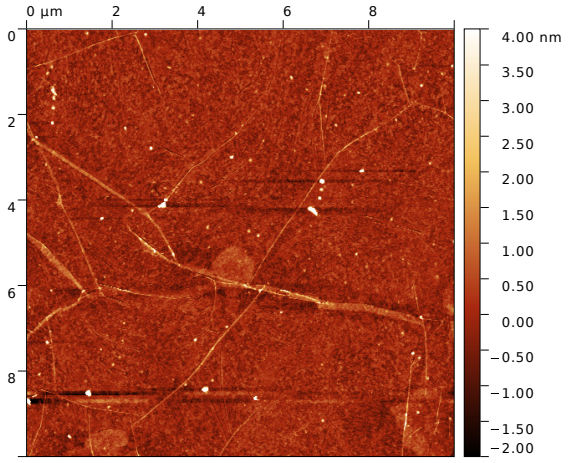

Figure B.5.: AFM image of the as-received graphene from Graphenea. The image was treated with Gwyddion software for flatten level and scars reduction.

Bibliography

[1] M. P. Levendorf, C. S. Ruiz-Vargas, S. Garg, and J. Park, Nano letters **9**, 4479 (2009).

[2] J. Kang, D. Shin, S. Bae, and B. H. Hong, Nanoscale **4**, 5527 (2012).

[3] K. M. Reddy, A. D. Gledhill, C.-H. Chen, J. M. Drexler, and N. P. Padture, Applied Physics Letters **98**, 113117 (2011).

[4] J.-Y. Choi, Nature Nanotechnology **8**, 311 (2013).

[5] K. S. Kim, Y. Zhao, H. Jang, S. Y. Lee, J. M. Kim, K. S. Kim, J.-H. Ahn, P. Kim, J.-Y. Choi, and B. H. Hong, Nature **457**, 706 (2009).

[6] P. J. Ko, H. Takahashi, S. Koide, H. Sakai, T. V. Thu, H. Okada, and A. Sandhu, Journal of Physics: Conference Series **433**, 012002 (2013).

[7] X. Liang, B. a. Sperling, I. Calizo, G. Cheng, C. A. Hacker, Q. Zhang, Y. Obeng, K. Yan, H. Peng, Q. Li, X. Zhu, H. Yuan, A. R. H. Walker, Z. Liu, L.-M. Peng, and C. a. Richter, ACS nano **5**, 9144 (2011).

[8] Y. Y. Leng, *Materials characterization : introduction to microscopic and spectroscopic methods* (J. Wiley & Sons, 2008) p. 337.

[9] J. Díaz, G. Paolicelli, S. Ferrer, and F. Comin, Physical Review B **54**, 8064 (1996).

[10] Z. Luo, T. Yu, Z. Ni, S. Lim, J. Shang, H. Hu, L. Liu, Z. Shen, and J. Lin, (2010), arXiv:1009.0091 .

[11] D. C. Elias, R. R. Nair, T. M. G. Mohiuddin, S. V. Morozov, P. Blake, M. P. Halsall, A. C. Ferrari, D. W. Boukhvalov, M. I. Katsnelson, A. K. Geim, and K. S. Novoselov, Science **323** (2009).

[12] C. Mattevi, G. Eda, S. Agnoli, S. Miller, K. A. Mkhoyan, O. Celik, D. Mastrogiovanni, G. Granozzi, E. Garfunkel, and M. Chhowalla, Advanced Functional Materials **19**, 2577 (2009).

[13] Wolfmankurd, "The photoelectric effect," (2007).

[14] A. C. Ferrari, Solid State Communications **143**, 47 (2007).

[15] A. C. Ferrari and D. M. Basko, Nature nanotechnology **8**, 235 (2013).

[16] I. Childres, L. A. Jauregui, W. Park, H. Cao, and Y. P. Chen, New developments in photon and materials research **1** (2013).

[17] Moxfyre, "Molecular energy levels and raman effect," (2009).

[18] C. J. Shearer, A. D. Slattery, A. J. Stapleton, J. G. Shapter, and C. T. Gibson, Nanotechnology **27**, 125704 (2016).

C. Résumé

La photolithographie conventionnelle a toujours été la technique clé pour la structuration en microélectronique. Cependant, en raison des exigences continues de réduction des tailles des circuits intégrés, aujourd'hui inférieures à 50 nm, la résolution de la photolithographie rencontre certaines limitations physiques. Afin de maintenir la bien connue loi de Moore, le développement de techniques alternatives est au cœur de la recherche technologique.

Les copolymères à blocs (BCPs) ont la propriété particulière de s'auto-assembler en structures périodiques ordonnées. Ces macromolécules, en association avec la photolithographie standard, représentent une approche prometteuse en tant que technique de lithographie alternative avancée en microélectronique. De cette façon, la course à la réduction des dimensions des circuits intégrés (ICs) peut être maintenue. Les BCPs présentant une forte incompatibilité chimique entre leurs blocs présentent une valeur élevée du paramètre d'interaction de Flory-Huggins χ. La théorie des BCPs prédit alors des périodes caractéristiques qui peuvent être aussi petites que quelques nanomètres.

Cette thèse explore le potentiel de l'auto-assemblage du polymère à haut χ PS-*b*-PDMS en tant que candidat possible pour développer une lithographie par BCP de nouvelle génération, par rapport au plus courant PS-*b*-PMMA, dont la résolution est limitée à environ 20 nm. Les performances lithographiques de masques de PS-b-PDMS sont démontrées sur des substrats de Si et de graphène. Ce dernier matériau, ayant des besoins particuliers de structuration, a été particulièrement approfondi. Afin de faciliter la mise en œuvre de la lithographie par BCP dans l'industrie, une attention particulière a été portée au développement de procédés fiables et compatibles avec l'environnement microélectronique.

Dans le chapitre 2, l'influence de plastifiants, sélectifs pour le bloc PS, sur le processus d'auto-assemblage de PS-*b*-PDMS cylindriques et sphériques, a été étudiée. Les copolymères à blocs forment des micelles de PS-*b*-PDMS en solution avec un diamètre

hydrodynamique D_h commensurable avec leur période naturelle L_0. Les propriétés physiques des plastifiants telles qu'une pression de vapeur réduite et une sélectivité élevée pour le PS, favorisent un mouvement latéral des chaînes et, par conséquent, une amélioration significative de la cinétique d'auto-assemblage du PS-*b*-PDMS est observée. Des arrangements hexagonaux bien ordonnées ont pu être obtenus juste après le dépôt du polymère sans aucun recuit.

Ensuite, en utilisant des polymères cylindriques, l'évaporation du plastifiant par recuit thermique permet une transition morphologique rapide de l'état sphérique métastable vers la morphologie cylindrique stable. Après 30 s de recuit, des cylindres bien alignés ont été obtenus. Parmi les plastifiants testés, le DOA a donné le meilleur compromis entre le taux d'évaporation et la sélectivité pour le PS. De cette manière, un procédé pratique et très rapide pour faire de la lithographie par copolymère à blocs a été démontré et nous illustrons son applicabilité pour fabriquer des structures à haute résolution sur de grandes surfaces.

Après avoir montré le principe de la lithographie sur Si avec différentes couches minces de PS-PDMS (70 kg/mol et 45.5 kg/mol) dans le chapitre 2, avec des tailles de l'ordre de 30 et 25 nm respectivement, l'attention a été centrée sur des matériaux émergents. Le chapitre 3 donne les principaux concepts pour comprendre les problématiques du graphène. Par exemple, des nano-structures de graphène doivent être créées afin d'ouvrir une bande interdite électronique dans le matériaux (intrinsèquement semi-métallique) par confinement latéral (< 10 nm) des électrons de Dirac. Effectivement, des nanorubans de graphène (GNRs) pourraient être envisagés comme canaux dans les transistors à effet de champ dans les circuits intégrés.

Dans ce contexte, la lithographie par PS-PDMS pourrait répondre à la demande de motifs de graphène à ultra-haute résolution. Peu d'études ont été menées sur la fabrication de GNRs en utilisant un BCP et d'autres études sont nécessaires pour répondre à plusieurs questions sans réponse. Du point de vue de la nano-fabrication, les GNRs devraient idéalement être fabriqués sur de grandes surfaces avec des procédés compatibles CMOS, à une résolution inférieure à 10 nm, avec une qualité chimique et une structure de bords contrôlée.

Afin d'obtenir un masque dur de moins de 10 nm pour la structuration du graphène, l'auto-assemblage de PS-*b*-PDMS avec une résolution de 10 nm a été étudié au chapitre 4. Cette tâche difficile a été étudiée selon trois approches :

- l'utilisation d'une sous-couche comme couche de transfert intermédiaire
- le couchage et l'auto-assemblage directement sur graphèn
- l'auto-assemblage dirigé avec une approche de ≪soft graphoepitaxy≫ (guidage du BCP par des lignes polymères amovible)

Dans l'approche de sous-couche, l'idée était de protéger la couche de graphène pendant les étapes de lithographie avec un matériau qui peut être facilement nettoyé sélectivement de la surface de graphène. Différents matériaux allant des polymères aux diélectriques à haute valeur de κ ont été testés. Des calculs de la longueur de corrélation ont été mis en œuvre afin de quantifier l'auto-assemblage du PS-*b*-PDMS sur l'empilement sous-couche / graphène. Dans tous les cas, une qualité d'auto-assemblage faible a été atteinte (longueur de corrélation $\xi \sim 30-50$ nm). Comme la longueur de corrélation représente la décroissance exponentielle de la fonction de corrélation, elle est fréquemment interprétée comme la longueur moyenne des grains de polymère organisés, ce qui est considéré comme insuffisant ici pour tout développement de dispositif.

De meilleurs résultats d'auto-assemblage ont été obtenus avec un couchage et un auto-assemblage directement sur le graphène. Une étape de pré-recuit thermique de la couche de graphène à 170 °C sous vide a été mise en œuvre avant l'auto-assemblage. Il est montré par des mesures de l'angle de contact et de la spectroscopie Raman que cette étape préalable modifie l'affinité chimique du graphène CVD sans introduire une quantité importante de désordre dans la structure du graphène.

Malgré l'amélioration de l'auto-assemblage, une couche de mouillage de PDMS est toujours présente à l'interface BCP / graphène, ce qui est préjudiciable aux expériences de gravure. Le modèle d'énergie de surface de Good et Girifalco montre que, en chauffant préalablement le graphène CVD à des températures encore plus élevées, il est susceptible de favoriser le mouillage du PS par une plus ample modification de son énergie de surface. Les résultats expérimentaux obtenus par les observations SEM et STEM ont prouvé cette affirmation. Finalement, la morphologie souhaitée du film mince PS-b-PDMS est obtenue (PS mouillage sur graphène) en même temps qu'une amélioration de la qualité d'auto-assemblage ($\xi \sim 300$ 300 nm).

Pour l'auto-assemblage dirigé du PS-PDMS sur graphène, un procédé de graphoépitaxie a été développé en utilisant des lignes de guidage en résine. Néanmoins, la rugosité élevée des lignes de guidage a affecté l'auto-assemblage des cylindres de PDMS. De plus, une

forte affinité probable du PDMS avec ces lignes de guidage oriente les cylindres de PDMS perpendiculairement, ce qui n'était pas recherché ici. Dans ce qui suit, c'est le masque de lithographie PS-b-PDMS obtenu directement sur graphène sans lignes de guidage qui est utilisé dans l'étude de la structuration du graphène par gravure plasma.

Dans le chapitre 5, la compréhension de la gravure plasma a permis de structurer le graphène avec un masque de BCP en tenant compte de la sélectivité du masque et de la vitesse de gravure. Une gravure plasma avec une composante physique plus importante évite une gravure latérale du graphène pendant le transfert par rapport à une gravure plus chimique qui semble graver le graphène latéralement sous le masque. Ceci est confirmé par les caractérisation électrique ultérieures.

L'analyse de la structuration du graphène a été suivie par les techniques habituelles de caractérisation du carbone. La spectroscopie Raman est un outil performant pour cela, avec une signature du graphène dans les pics G et 2D. L'apparition du pic D est un élément clé car il est interprété comme les défauts de bords des rubans de graphène et permet donc de remonter à leur dimension latérale. L'AFM a permis également de déterminer les dimensions de GNRs : les centres de la distribution gaussienne de hauteur et de largeur ont été mesurés à ~ 5 Å et ~ 11 nm respectivement.

La question de la qualité chimique et de la propreté des GNRs a été soulevée au cours de cette thèse. Pour cela, les GNRs ont été nettoyés après l'enlèvement du masque avec des plasmas d'hydrogène. En effet, des matériaux polymères sont utilisés à la fois pour le transfert de graphène CVD sur des substrats SiO_2 (PMMA) et pour la formation de graphène (PS-*b*-PDMS) et ceux-ci représentent une source importante de contamination par du carbone amorphe. De plus, la gravure du graphène avec un plasma à base d'oxygène génère une recombinaison au niveau des bords qui dope (p) les structures de graphène. Des mesures XPS ont montré l'élimination efficace des espèces carboxyle, C-O et carbone amorphe. Une quantification XPS a également montré la réduction du carbone sp^2 qui correspond approximativement à la surface de graphène retirée du fait de sa structuration. Les plasmas d'hydrogène présentés ici ont montré une manière efficace et non-destructrice de nettoyer et d'adapter les GNRs. La complémentarité des techniques d'analyse du carbone utilisées a permis de prouver la structuration du graphène, tandis que les caractérisations électriques effectuées ont confirmées cette analyse.

Les matrices de GNRs fabriquées sur SiO_2 sont finalement caractérisées sur de grandes surfaces à l'aide d'un outil de cartographie Raman. La relation de Cançado a permis de

calculer la longueur des défauts L_D, qui est interprétée comme la largeur des GNRs. Il a été trouvé que la zone analysée (100 μm^2) était couverte par une matrice de GNRs avec des largeurs de canaux de 11 $\pm$ 1 nm, ce qui correspond parfaitement aux profils AFM.

Enfin, des dépôts de contacts métalliques ont été réalisés par photolithographie contact et par un procédé innovant de transfert de motifs (pour éviter le dépôt direct de résine sur les GNRs nettoyés) pour une caractérisation électrique des structures fabriquées. Par les deux méthodes de dépôt de contacts, une relation I-V hautement non linéaire a été mesurée, indiquant l'émergence d'un comportement semi-conducteur (ouverture de bande interdite) par un effet de confinement latéral dans les GNRs. Le meilleur ratio I_{on}/I_{off} mesuré en utilisant le substrat dopé comme grille était de $\sim$ 3.7 pour une séparation drain-source de 2 μm, ce qui est comparable à certaines mesures dans la littérature à température et pression ambiantes. Les GNRs nettoyés fabriqués ici présenteraient certainement des caractéristiques de conductance améliorées dans un dispositif avec une séparation drain-source plus courte, évitant la dispersion des porteurs et améliorant le confinement latéral.

D. Contributions

Peer review articles

1. **J. Arias-Zapata**, S. Böhme, J. Garnier, C. Girardot, A. Legrain and M. Zelsmann, *Ultra-fast assembly of PS-PDMS block copolymers on 300 mm wafers by blending with plasticizers.* **Advanced Functional Materials** vol. 26, p. 5690 (2016)

2. J. Garnier, **J. Arias-Zapata**, O. Marconot, S. Arnaud, S. Böhme, C. Girardot, D. Buttard, and M. Zelsmann, *Sub-10 nm silicon nanopillars fabrication using fast and brushless thermal assembly of PS-b-PDMS diblock copolymer.* **ACS Applied Materials & Interfaces** vol. 8, p. 9954 (2016)

3. **J. Arias-Zapata**, J. Cordeiro, S. Böhme, C. Girardot, J. Garnier, P. Bezard, K. Ntetsikas, G. Liontos, A. Avgeropoulos, D. Peyrade, and M. Zelsmann, *High throughput sub-10 nm metallic particles organization on templates made by block copolymer self-assembly and nanoimprint.* **Microelectronic Engineering** vol. 141, p. 155 (2015)

International conferences

Underlined = Speaker, $*$ = Proceedings

Invited presentations

1. S. Böhme, C. Girardot, J. Garnier, **J. Arias-Zapata**, S. Arnaud, O. Marconot, D. Buttard, G. Cunge, O. Joubert, and M. Zelsmann, *A route for industry-compatible*

DSA of high-chi PS-PDMS block copolymers. China Semiconductor Technology International Conference - **CSTIC 2016**, March 2016, Shanghai (China)

2. S. Böhme, P. Bezard, C. Girardot, J. Garnier, **J. Arias-Zapata**, S. Arnaud, G. Cunge, M. Zelsmann, and O. Joubert, *DSA pattern transfer with PS-PMMA and silicon-containing block copolymers.* **SPIE Advanced Lithography conference:** Advanced Etch Technology for Nanopatterning, Feb. 2016, San Jose (USA)

Oral presentations

1. A. Legrain, **J. Arias-Zapata**, S. Böhme, C. Girardot, C. Navarro, G. Fleury, and M. Zelsmann, *Novel Si-containing high- block-copolymer for nanolithography application: PS-b-PDMSB.* Micro- and Nano-Engineering conference - **MNE 2016**, Sep. 2016, Vienna (Austria)

2. **J. Arias-Zapata**, D. Ferrah, J. Garnier, S. Böhme, C. Girardot, G. Cunge, and M. Zelsmann, *Graphene structuration by self-assembly of block copolymers.* 13th International Conference on Nanosciences & Nanotechnologies - **NN16**, July 2016, Thessaloniki (Greece) / ∗ **Materials Today: Proceedings** vol. 4, p. 6827 (2017)

3. J. Garnier, S. Böhme, C. Girardot, S. Arnaud, **J. Arias-Zapata**, O. Marconot, D. Buttard, and M. Zelsmann, *Directed self-assembly process for high-χ PS-b-PDMS diblock copolymer compatible with microelectronics environment.* European Materials Research Society conference - **E-MRS 2015 Spring Meeting**, May 2015, Lille (France)

4. C. Girardot, J. Garnier, O. Marconot, S. Böhme, **J. Arias-Zapata**, E. Laforge, X. Chevalier, C. Nicolet, C. Navarro, D. Buttard, M. Mumtaz, G. Fleury, G. Hadziioannou, and M. Zelsmann, *In-situ GISAXS investigation during thermal and solvent annealing of high- block copolymers.* European Materials Research Society conference - **E-MRS 2015 Spring Meeting**, May 2015, Lille (France)

5. S. Böhme, J. Garnier, C. Girardot, **J. Arias-Zapata**, S. Arnaud, E. Dupuy, E. Pargon, O. Marconot, D. Buttard, and M. Zelsmann, *Plasma etching optimization and alignment control of directed self-assembled high-χ cylindrical PS-b-PDMS.* European Materials Research Society conference - **E-MRS 2015 Spring Meeting**,

May 2015, Lille (France)

6. **J. Arias-Zapata**, J. Cordeiro, S. Böhme, C. Girardot, J. Garnier, D. Peyrade, M. Zelsmann, *High throughput sub-10 nm metallic particles organization on templates made by copolymer self-assembly and nanoimprint.* Micro and Nano Engineering conference - **MNE 2014**, Sep. 2014, Lausanne (Switzerland)

7. S. Böhme, C. Girardot, J. Garnier, **J. Arias-Zapata**, E. Latu-Romain, G. Cunge, O. Joubert, M. Zelsmann, *Integration of high- PS-b-PDMS in industry-type photolithography stacks for high resolution lithography processes.* Micro and Nano Engineering conference - **MNE 2014**, Sep. 2014, Lausanne (Switzerland)

Posters

1. **J. Arias-Zapata**, H-A. Mehedi, D. Ferrah, M. Serege, A. Legrain, G. Cunge, M. Zelsmann, *Fabrication of high quality graphene nanoribbons on large surfaces by block copolymer lithography.* **Graphene Conference 2017** April 2017, Barcelona (Spain)

2. D. Ferrah, O. Renault, D. Marinov, **J. Arias-Zapata**, N. Chevalier, D. Mariolle, D. Rouchon, H. Okuno, V. Bouchiat, G. Cunge, *Toward new plasma procedure for efficient cleaning of high quality CVD graphene transferred onto SiO_2 /Si substrate.* **Graphene conference 2016** April 2016, Genoa (Italy)

3. S. Böhme, C. Girardot, J. Garnier, **J. Arias-Zapata**, S. Arnaud, R. Tiron, O. Marconot, D. Buttard, and M. Zelsmann, *A route for industry-compatible directed self-assembly of high-chi PS-PDMS block copolymers.* **SPIE Advanced Lithography conference**: Alternative Lithographic Technologies, Feb. 2016, San Jose (USA) / ∗ **Proc. SPIE** vol. 9777, p. 97791W (2016)

4. J. Garnier, S. Böhme, C. Girardot, M. Salaün, **J. Arias-Zapata**, and M. Zelsmann, *Polystyrene brush optimization for directed self-assembly of high-X PS-b-PDMS diblock copolymer.* European Materials Research Society conference- **E-MRS 2015 Spring Meeting** May 2015, Lille (France)

Workshops & seminars

1. S. Böhme, **J. Arias Zapata**, P. Bézard, C. Girardot, J. Garnier, A. Legrain, J. Cordeiro, D. Peyrade, M. Zelsmann, *Nanolithography with high-χ block copolymers.* Journées Nationales sur les Technologies Emergentes en Micronanofabrication 2015 - **JNTE 2015**, Nov. 2015, Lyon (France)